Electron Recombination Studies on Titanium Oxide Ions in the Cryogenic Storage Ring at the Max Planck Institute for Nuclear Physics, Heidelberg

A thesis submitted

in partial fulfillment for the award of the degree of

Master of Science

in

Solid State Physics

by

Naman Jain

Department of Physics

Indian Institute of Space Science and Technology

Thiruvananthapuram, India

June 2020

Electron Recombination Studies on Titanium Oxide Ions in the Cryogenic Storage Ring at the Max Planck Institute for Nuclear Physics, Heidelberg

This Master's Thesis has been carried out by Naman Jain
at the Max-Planck-Institute for Nuclear Physics in Heidelberg
under the supervision of
Prof. Dr. Andreas Wolf (MPIK)
Dr. Oldřich Novotný (MPIK)
and Dr. Umesh Kadhane (IIST)

Declaration

I declare that this thesis titled ***Electron Recombination Studies on Titanium Oxide Ions in the Cryogenic Storage Ring at the Max Planck Institute for Nuclear Physics, Heidelberg*** submitted in partial fulfillment for the award of the degree of **Master of Science** in **Solid State Physics** is a record of original work carried out by me under the supervision of **Prof. Dr. Andreas Wolf**, and has not formed the basis for the award of any degree, diploma, associateship, fellowship, or other titles in this or any other Institution or University of higher learning. In keeping with the ethical practice in reporting scientific information, due acknowledgements have been made wherever the findings of others have been cited.

Place: Thiruvananthapuram
Date: June 2020

Naman Jain
(SC15B151)

Abstract

Numerous observations have reported the sustained presence of complex molecules in the interstellar medium (ISM) since the first half of the twentieth century. Especially the production of large molecules in such harsh environments is still an outstanding fundamental problem in the scientific community. It is known that the complex chemical processes observed in the gas-phase of ISM are majorly based on ion reactions. Dissociative recombination (DR) of molecular ions is a dominant process in such environments that neutralizes the plasma and leads to the fragmentation of molecules. In this context, metal oxides have been proposed to play a significant role in the complex reaction mechanisms within the astrochemical networks. In this work we undertake a detailed study on one such distinctive system, the titanium monoxide cation (TiO^+) which can be formed by the chemi-ionization (CI) process between atomic titanium and oxygen. The process has been proposed to be responsible for the production of free electrons and severe atomic depletion of Ti in gas phase ISM. The inverse process, DR, is expected to be endothermic, contrary to most other cases. Precise laboratory studies on the DR of TiO^+ are needed for a concrete proof of the reaction energetics, thus elucidating the molecular reaction dynamics. Apart from offering a first detailed insight into the unexplored regime of endothermic DR reactions, this would lend momentous possibilities for better practical applications of TiO^+, an extremely significant compound as a precursor for TiO and TiO_2 which are crucial for material sciences applications and commercial industries alike. Understanding of such an endothermic DR also opens up avenues for novel scientific proposals in varied fields such as in communication systems technology to mitigate atmospheric scintillation.

To the best of our knowledge, no direct investigation of the specific DR for such class of reactions has been carried out until the time of production of this work, experimentally or theoretically. Such experiments have been conducted at the Max-Planck-Institute for Nuclear Physics, Heidelberg as a part of this study at the electrostatic Cryogenic Storage Ring (CSR) in similar conditions as in the cold ISM. Here, we elucidate the experimental apparatus, implemented techniques, measurement campaign, obtained data and the interim results of a TiO^+ DR experiment performed with the electron beam setup at CSR.

Contents

Chapter 1

Introduction

Our quest for understanding nature, in many ways, was revolutionized with the inception of quantum mechanics in the early twentieth century. Over the course of time, numerous ideas have been built upon the elegant foundations laid by the theoretical and experimental ventures alike. The recent advancements in the broadest fields of physical sciences aim at building the structure up further by probing deeper into the quantum phenomena. For these reasons, we have looked as far away into the universe as possible, and even close inside an atom. Both these extremities have provoked advancements in science and technology in coherence, to understand the highly complex interplay of the physical processes, extreme conditions and the transpiring chemical reactions in the interstellar medium (ISM), as well as foraying into the subatomic regimes, through precision measurements, and ingenious methods to perform spectroscopy forgoing the distinct classical boundaries laid for the disciplines. Quantum dynamical processes, in this respect, are a fundamental building block of the chemical network which also traces the origins of life and even the universe as we observe it, presenting a vast regime of physics still holding enormous potential to explore over plethora of different natural scales. In order to probe into one such regime, this work resorts to the molecular dimension wherein the pieces of puzzle are broadly set yet relatively well defined.

One of the primary motivations of this investigation is the need for understanding the highly complex phenomena and processes present in the interstellar medium (ISM). Over the years, it has been understood that most of the gas-phase interstellar chemistry is driven by ion reactions [1]. At low temperatures (10-100 K) the dominant reactions are the *dissociative recombination* (DR) of molecular ions with free electrons, and *ion-neutral reactions*, both of which play a key role in controlling the charge density and composition of the cold ISM [2, 3]. This work aims at a detailed study of DR reactions– essentially a neutralization process, wherein a free electron with some kinetic energy recombines with

positively charged molecular ion. The ion can make use of its internal structure and transfer the electron to a bound state while breaking one or several chemical bonds, making the process generally exothermic, and also substantiating the name of the process given the fact that the capture of electron is stabilized by dissociation (see sec. 1.1). Although a primary chemical process, DR is at the heart of gas-phase reactions in the ISM leading to the production of neutral atoms and molecules [4] and has been expected to be instrumental in explicating the presence of some of the significantly complex molecules that have been observed in space, exact pathways and time scales involved in the formation of which, are still poorly understood. With the Cryogenic Storage Ring (CSR) at the Max Planck Institute of Nuclear Physics in Heidelberg, Germany, commissioned in 2015 [5], it is possible to study such critical reactions in conditions similar as in the cold ISM. With a closed orbit of about 35-meters the completely electrostatic cryogenic storage ring is designed to store ion beams at energies up to 300 keV per unit charge, independent of ion mass. The ions can be stored for up to thousands of seconds in a low-temperature radiation field given by the black-body radiation of the beamline wall at less than 10 Kelvin [6]. At these conditions ions can radiatively de-excite towards their ro-vibrational ground-states in background gas pressures that have been observed reaching as low as 10^{-14} mbar [5].

The production and sustained presence of organic molecules in the ISM is one of the fundamental problems which has remained unsolved for quite long in the scientific community and is still a topic of utmost interest. Often referred to as the astrochemical puzzle, the observation of organic molecules from diatomics such as CH^+ in 1937 [7, 8], to polycyclic aromatic hydrocarbons (PAHs), as large as C_{60} fullerenes [9, 10] conclusively proved in 2010, has raised the essential question about their formation pathways. Numerous astrophysical models have been proposed to calculate the abundances of fundamental elements, which are then used as starting ingredients for the simulation of other complex processes leading to the formation of larger molecules through various chemical reaction chain models. In this context, metal oxides have been proposed to play a significant role in the reaction mechanisms as intermediate products [11], a strong possibility often attributed to their nature of forming stable ionic compounds, but have not been successfully observed. There have been upper limits defined for the abundances of these metal oxides but it is unclear if it implies the severe depletion of these metals in the ISM or if simply the metal oxides are not formed efficiently [12]. On the other hand, numerous visual and ultraviolet observations of the diffuse ISM have shown a severe depletion of metals such as Ca, Fe and Ti [13, 14]. It is important to understand this as the elemental depletions not only have a significant effect on the composition of the interstellar dust grains, affecting the surface

chemistry in the ISM but also affect the ionization levels in the dense interstellar clouds which in turn can directly affect the star formation process.

We consider one such distinctive system, the titanium monoxide cation TiO^+, which is extremely intriguing for multifarious reasons. Firstly, atomic Ti in gas-phase has been observed to be significantly depleted in the ISM, suggesting its presence on dust grains or in the molecular form [15]. Additionally, while the neutral counterpart, TiO is known to have a considerable impact on the structure of the stellar atmosphere [16], has been observed as a major spectral feature of M-type stars, and is known to be a vital specie for numerous other astronomical systems based on indirect deductions [17, 18]. However, explicit searches for the TiO molecule signatures in sub-mm radio wavelengths have resulted in unsuccessful attempts concluding, as in the work by Churchwell et al., "...the 'missing' or 'depleted' atomic interstellar gas phase Ti is not in the form of gaseous TiO" [15].

At this point, it is important to note that the associative ionisation or chemi-ionisation (AI or CI) reaction for titanium and oxygen atoms, wherein the two atomic species combine to form a diatomic molecular ion, releasing a free electron in the process, has been hypothesized to be an exothermic reaction process, an unusual phenomenon. This, in turn, implies that the inverse process of AI, i.e. dissociative electron recombination (DR) with the TiO^+ should be an endothermic reaction, represented as [19]:

$$\mathrm{TiO}^+ + e^- \longrightarrow \mathrm{Ti} + \mathrm{O} \quad (E_{\mathrm{reac}} = -0.05 \pm 0.07\,\mathrm{eV}) \tag{1.1}$$

which may crucially influence the expected form of Ti present in the ISM and the diffuse interstellar clouds. Furthermore, the aforementioned reaction then holds the potential for the stability of TiO^+ to be responsible for high production of free electrons in the ISM, which can further play a pivotal role in the production of other molecules, as has been proposed in earlier investigations [20]. Interestingly, TiO^+ has a high molecular dipole moment of ~ 6.3 D, which also paves way for a rich collection of rotational and vibrational levels favorable for observation which have been used in other fields [20] as well.

Another momentous practical aspect that makes the TiO^+ system especially interesting is the conceivable use in communication systems technology by enhancing the electromagnetic wave transmission in the atmosphere, a scientific proposal that has been gaining momentum recently [21]. Based on the understanding that fluctuations in electron density in the ionosphere can cause disruption in radio-wave transmission used for satellite communications, a common phenomenon termed as scintillation, a possible mitigation strategy would involve local creation of regions with artificially enhanced electron density in the

ionosphere using the CI reaction of metal atoms that can readily react with oxygen atoms, abundant in the ionosphere, favorably producing a positive ion and a free electron [22]. While for most metals, the CI process is endothermic and thus inefficient due to a more robust and energetically favoured inverse process (i.e. DR), for many lanthanide metals and a few transition and actinide metals, the CI reaction is sufficiently exothermic [23]. For these limited number of elements, the metal monoxide has an ionization energy (IE) smaller than its bond dissociation energy, resulting in an exothermic release of an electron at thermal energies, wherein TiO^+ is one such case [24]. Hereby, a detailed and exceedingly accurate understanding of such a reaction is imperative to be applied efficiently for the purpose. Given the premise, however, it is important to remark that, to the best of our knowledge, no direct investigation of the specific CI or DR reactions for these elements has been carried out until the time of production of this work, experimentally or theoretically. As a part of this study, we undertake a detailed investigation of the hypothesized endothermic DR reaction for TiO^+ molecule at the CSR facility, in MPIK, Heidelberg, which is an appropriate tool for such a comprehensive study, enabling energy resolutions down to meV levels, and setting a crucial milestone in the field.

1.1 Dissociative recombination (DR) process

The process of dissociative recombination can loosely be put together as a combination of two separate steps: first being neutralization wherein the electron recombines with an ionic molecule, and second, molecular fragmentation. A complex yet fundamental chemical reaction, the DR process occurs abundantly on the Earth and is accountable for numerous critical phenomena in our immediate surroundings [25, 26]. Its pivotal role as a neutralising agent in the Earth's upper atmosphere has been well established and its occurrence in many natural and laboratory-produced plasma has been a strong motivation for studying the process, which is still poorly understood [4]. It is also known to be at the heart of some of the most complicated gas-phase reactions transpiring in the ISM, as has been discussed previously, and has been proposed to be the essential phenomenon providing exit pathways for charged-particle astrochemical reaction chains [2, 27, 28]. The DR process influences important applications in industry, astrophysics, atmospheric science, plasma physics and fusion research, among others, and has been an outstanding topic of research [29–32], which we intend to delve deeper in to with the current work.

In order to understand this process, it is instructive to use the molecular potential energy curves obtained by solving the Schrödinger equation for the electronic wavefunctions

of a diatomic molecule, as a tool to picture the dynamics of the process transpiring when energy is deposited into a molecular system through collisions or by photon absorption. At the onset it is to be remarked that for cases where the potential energy curves are not energetically well-separated, i.e. the energy eigenvalues of the electronic states become degenerate, couplings between the electronic and the nuclear motion start to play a role, and the *Born-Oppenheimer* (BO) approximation, which is generally used for simplifying the Schrodinger equation, falls apart. As in the situation under consideration, although collision energy of the incoming electron may be very low, when it recombines, the total energy is at the ionization potential of the neutral. Therefore, there exists an infinite number of Rydberg states converging to each state of the ion, corresponding to different potential energy curves which may lie extremely close in energy, thus leading to the breakdown of BO approximation and allowing for non-adiabatic coupling between states. At these nuclear configurations, the degeneracy of the respective electronic states is lifted and avoided crossings might occur equivalent to a nuclear motion not defined by the potential energy curve of a single electronic state only.

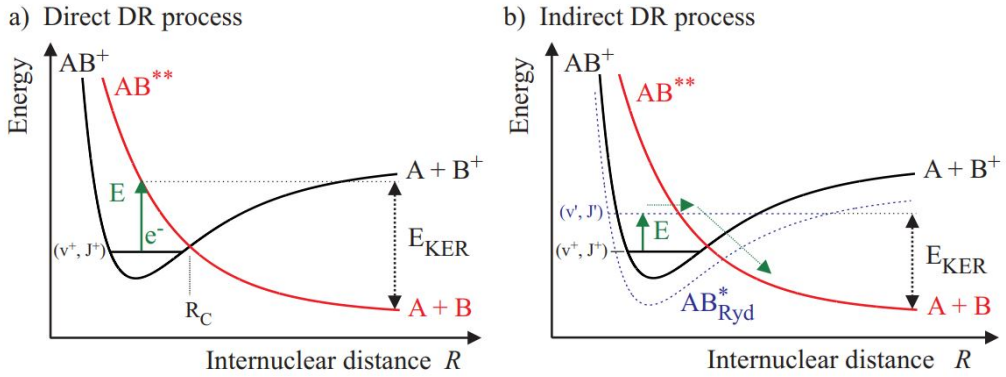

Figure 1.1: Potential curves schematic representing DR. The electron with energy E_{e} is captured in (a) directly into the repulsive state AB** (red line) thus direct DR, whereas in (b), the indirect DR first the ro-vibrational level (v', J') of an excited Rydberg state (dashed blue line) is formed before dissociation of the molecular system continues upon AB** (red line). The final atomic fragments A and B are emitted with a kinetic energy E_{KER}. Image adapted from PhD thesis of S. Novotny [33].

The DR process is known to follow one of the two proposed reaction mechanisms, viz. direct DR and indirect DR, as presented in the potential energy schematic figure 1.1. Both processes usually start by a free electron (at electron-ion collision energy E_{e}) recombining with a molecular cation (initial vibrational and rotational states denoted by v^+ and J^+) into

a temporary neutral state which later fragments out along with some kinetic energy E_{KER}:

$$\mathrm{AB}^{+}\left(v^{+}, J^{+}\right) + e^{-}\left(E_{\mathrm{e}}\right) \longrightarrow \mathrm{A}\left(n, l\right) + \mathrm{B}\left(n', l'\right) + E_{\mathrm{KER}} \tag{1.2}$$

where the final atomic products A and B are distinguished by their principal and orbital angular momentum quantum numbers n (n') and l (l'). In the *direct* DR process, which is purely electronic, the final state of the system is a resonant state, i.e. a valence state of the neutral that is embedded into the scattering continuum of the system. As opposed to a Rydberg state converging to the ground state of the ion, this state represents a double excitation with respect to the combined system, which is repulsive. As the neutral molecule travels along the potential energy curve, it fragments out and if the products are stable with respect to autoionization in context of the internal states, it leads to final neutrals. Formally, assuming that the electronic coupling (given by the matrix element between electronic states of the reactants and the dissociative state, coupled by the electronic Hamiltonian) varies only slowly in the overlap region, the direct DR cross section σ_{direct} for a single dissociative curve is governed by the Franck-Condon factor $\left|\langle\Psi_{AB^{**}}(R)|\Psi_{AB^{+}}(R)\rangle\right|^2$ and is inversely proportional to the electron energy E_{e}. Often though, this state can then cross the Rydberg states convergent to the ground state of the ion curve before the system has reached the asymptotic region. These crossings do not affect the total cross section of the DR but can dramatically change the final state product distribution [4].

The comparatively straightforward case of direct DR is complicated by the Rydberg states that converge to the ground state of the molecular ion. In the *indirect* mechanism the capture of the electron proceeds through non-adiabatic couplings by the breakdown of the BO approximation and forms a rotationally and vibrationally excited molecular Rydberg state. These states, lying near parallel to the ionic states, are bound and cannot directly dissociate. However, since the expanse of the wavefunction is broader here, it is possible for these states to couple to the dissociative resonant state. In essence, electron capture here is first followed by a second radiationless transition (predissociation) where the excited Rydberg state couples to the repulsive state AB^{**} upon which the system then continues towards dissociation. This can further lead to products, which may or may not be internally excited as discussed in the previous case. It is also important to note that the two processes are indistinguishable paths to the same products and thereby interfere. This causes sharp peaks in the total cross section as a function of energy, and similar oscillations in the final state distribution as a function of energy.

1.2 TiO^+ as a system

Titanium monoxide molecular system is exceptional not only due to the hypothesized endothermic DR and the astrophysical relevance as has been highlighted previously, but is also interesting due to its far-reaching practical applications in the industry. For instance, its neutral counterpart TiO is known to be a valuable precursor for the synthesis of TiO_2, which is an extremely significant compound for material sciences and commercial industries alike, with applications in water-splitting as anodes for commercial use, pigments, coating materials, catalysts, photo-voltaic cells, gas sensors, smart membranes, biomaterials, and development of sustainable technology [34–36]. Naturally, a better understanding of the quantum dynamics in context of the particular molecule would undeniably aid in enhanced applications of the same and thus, various studies before have delved into the investigation of titanium oxide molecular ion TiO^+, studying the cross-sections, rate constants and energetics of reactions comprising of the ion specie. These investigations usually involved study of the AI process for Ti and O, or more frequently the explicit exploration of the neutral or ionic form of titanium monoxide molecule using photoelectron spectroscopy, photodissociation spectroscopy and mass-analysed threshold ionisation techniques, to study the molecular structure and bond energies in detail [19, 37–44]. In order to study the DR for TiO^+ ion, as indicated in equation 1.1, it is important to note the energetic relations surmising the relevant energy balance for the DR that can be expected in accordance with the measurements and calculations performed in other works [19, 45–48]. This has been summarised in figure 1.2.

To investigate the aimed DR reaction at the CSR, the fundamental experimental observable at our disposal enables the determination of kinetic energy released in the process. As outlined previously, the DR process in our case, is strongly dependent on the initial state (electronic, vibrational and rotational) of the molecule and the incoming electron energy spread given by the experimental settings (see section 4.3). This dependence is manifested in the kinetic energy release (see eqn. 4.6), and final states (electronic) of the formed neutral atomic products – a complete knowledge of which ascertains an exhaustive picture of the reaction. While a detailed discussion of the interplay of these variables forms the subject matter of chapter 4, here we outline the crucial parameters that step in as a characteristic of the atomic and molecular systems involved.

The TiO^+ ion has a stable electronic configuration of $X^2\Delta$, or a doublet ground state. Only a few theoretical works have delved into the calculation of potential energy curves for the molecule due to the high complexity involved, for instance the work by Miliordos and

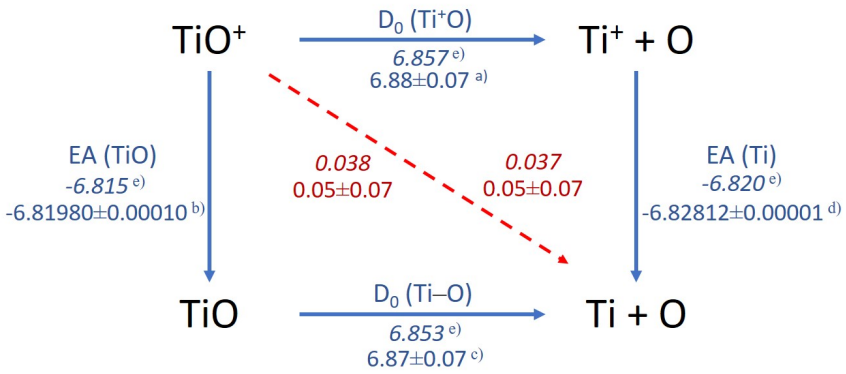

Figure 1.2: Energy cycle for the TiO system based on the principle of energy conservation, depicting the expected reaction energy values for TiO^+ DR (in red), via two pathways as indicated (in blue) involving electron affinity (EA) and bond dissociation (D_0) energy values. For indicated reaction energy of each step, values obtained from theoretical calculations are in italics while experimental values are in normal font. All values are in the units of eV. a) D.E. Clemmer et al., J. Chem. Phys. 1991, 95; b) H. Huang et al., J. Chem. Phys. 2013, 138; c) C. Naulin et al., Chemical Physics Letters, 1997, 266; d) L. Matsuoka et al., J. Opt. Soc. Am. B 2007, 24; e) Y. Pan et al., J. Phys. Chem. A, 2017, 121.

Mavridis [43]. The experimentally obtained energy difference for the lowest lying states electronic of TiO^+ have been listed in table 1.1, which have been used as a reference for this work. It is important to note that the doublet structure leads to a splitting of the ground state by $\sim$ 26.2 meV (ref. [48]), a result of the fine-structure of the molecule due to spin-orbit coupling. Further, there are rotational and vibrational energy quanta that the molecule can accommodate, giving rise to further energy level structure and has been elucidated in section 3.3.

Further, to characterise the neutral product fragments, in our case Ti and O atomic species, only a knowledge of electronically excited states is required, which is known to a rather high accuracy. In the tables 1.2, we list the relevant lowest excited states for Ti and O [49, 50].

It is instructive to note here that according to the mechanism of the DR reaction for our case of TiO^+, the initial state energy (electronic and rovibrational) of the molecule E_i along with the energy of the incoming electron in the center-of-mass frame of the system E_cm forms the total input energy (E_i + E_cm). The reaction then proceeds as dictated by quantum mechanical considerations, accounting for the reaction energetics ΔE, finally leading to the neutral products Ti and O, possibly in electronically excited states, the internal energy sum amounting to E_f in total, while the balance is manifested as the kinetic energy of the

Lowest lying electronic states for TiO^+			
Index	**Molecular state**	**Excitation energy** [cm^{-1}]	**Excitation energy** [eV]
0	$X^2\Delta_{3/2}$	0.0 (reference)	0.0
1	$X^2\Delta_{5/2}$	211.3	0.0262
2	$A^2\Sigma^+$	11227	1.392
3	$B^2\Pi$	15426	1.913
4	$a^4\Delta$	25750*	3.193

Table 1.1: A list of the energy separations for the lowest lying molecular states with respect to the ground state of TiO^+. It is to be noted that the ground state for the molecule is a doublet, separated by $\sim$26.2 meV due to spin-orbit coupling. The listed excitation energy values have been obtained experimentally by H. Huang et al. [48], while the energy marked with $\star$ is a theoretically calculated estimate.

products E_{KER}, according to the law of conservation of energy. This can be shown as:

$$\mathrm{TiO}^+ \left(E_\mathrm{i} + E_{\mathrm{TiO}^+}(J,v)\right) + e^- \left(E_\mathrm{cm}\right) \xrightarrow{\Delta E} \mathrm{Ti}(E_{\mathrm{f,Ti}}) + \mathrm{O}(E_{\mathrm{f,O}}) + E_{\mathrm{KER}} \tag{1.3}$$

The figure 1.3 depicts the energy balance through DR schematic in accordance with the convention used in this formalism and the table 1.3 has been produced for instantiation, listing values expected for E_{KER} ($= E_\mathrm{i} - E_\mathrm{f}$), considering $E_\mathrm{cm} = 0$, $\Delta E = 0$, and no rotational or vibrational excitations, for the predominantly relevant low-energy initial and final states for the involved atomic and molecular species. A level structure schematic is presented in figure 1.4. It is to be remarked that for calculating the actual E_{KER}, one needs to further add the quantity (E_cm + $E_{\mathrm{TiO}^+}(J,v) - \Delta E$) to the energy value listed in table 1.3, where $E_{\mathrm{TiO}^+}(J,v)$ is the energy brought in due to the initial rotational (J) and vibrational state (v) of the molecule, and the reaction energy ΔE is considered to be positive when the DR reaction is endothermic, i.e. ground energy level of TiO^+ is lower than that for the cumulative energy level for the products. This can expressed as,

$$E_{\mathrm{KER}} = (E_\mathrm{i} - E_\mathrm{f}) + E_\mathrm{cm} + E_{\mathrm{TiO}^+}(J,v) \; - \Delta E \tag{1.4}$$

Outline of this work

The introduction and motivation of this work is followed by a brief overview in Chapter 2 about the elaborate experimental apparatus used at the CSR's electron cooler section,

Lowest lying electronic states for products				
Index	**Ti**		**O**	
	Ti-state	Excitation energy [eV]	O-state	Excitation energy [eV]
0	a^3F_2	0.0 (reference)	$^3P_2$	0.0 (reference)
1	a^3F_3	0.021	$^3P_1$	0.0196
2	a^3F_4	0.048	$^3P_0$	0.0281
3	a^1D_2	0.800	$^1D_2$	1.967
4	a^5F_1	0.813	$^1S_0$	4.190
5	a^5F_2	0.818	-	-
6	a^5F_3	0.828	-	-
7	a^5F_4	0.836	-	-
8	a^5F_5	0.848	-	-
9	a^3P_x	1.05	-	-

Table 1.2: Table for the relevant low-lying electronically excited energy levels for the neutral product species, Ti and O. The conventional atomic configuration notations have been used to denote the states, with the term symbol complemented with the subscript J for the specific state, along with the experimentally obtained energy values from the works [49, 50].

at MPIK, Heidelberg, where this study has been performed. The chapter also follows the discussion of various techniques employed in the experiment to optimise the conditions, in order to reach the aimed precision levels of $\sim$ meV electron-ion collision energies, along with a short description of the detector setup and measurement schemes relevant for this work.

Moving forth, Chapter 3 describes the conditions prevalent during the measurement campaign, starting from a brief description of the Penning sputtering ion source used to produce the TiO^+ ion beam, and analysis techniques used to understand the beam composition. This is followed by an exhaustive summary and listing of the measurement parameters and physical conditions as observed and recorded at the time of measurement. The chapter ends with a discussion of the radiative cooling model used to estimate the rovibrational population distributions of the injected ion beam, crucial for further study of the reaction.

Chapter 4 moves towards the first step of the analysis wherein the procedures to extract, calibrate, filter and visualize the recorded data from the experimental beamtime have been outlined and important results from these proceedings have been elaborated. This chapter

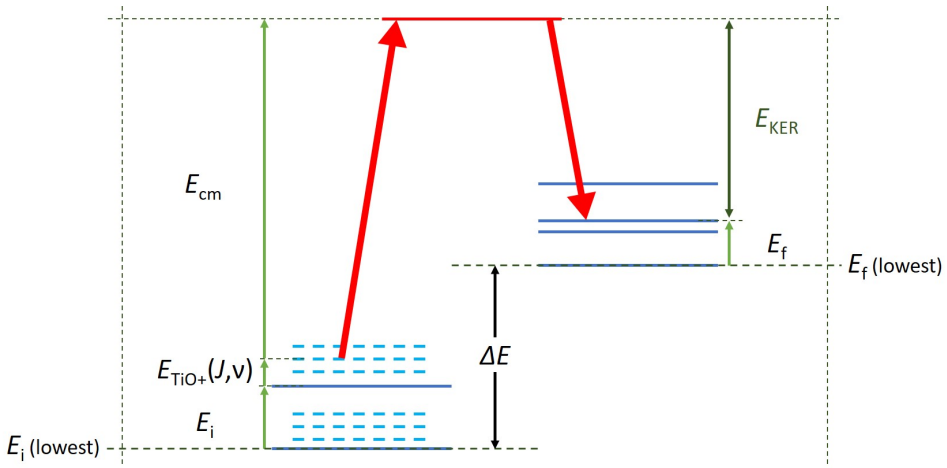

Figure 1.3: Energy balance depicted through an example DR reaction schematic, in accordance with the convention used in this work. The initial electronic state (dark blue line) of the molecule is considered to be at an energy E_{i} with respect to the lowest possible energy level. Rovibrational energy levels (depicted as dashed blue lines) add another contribution to this state $E_{\mathrm{TiO^+}}(J,\nu)$. Recombination with an E_{cm} energetic incoming electron takes the system through a representational total energy level (red line), finally to the final product state, with internal excitations amounting to E_{f} energy higher than the ground level. The balance is manifested as the KER, i.e. E_{KER}. The difference between the lowest possible ground levels is termed as endothermicity $\Delta E = E_{\mathrm{f,lowest}} - E_{\mathrm{i,lowest}}$.

also discusses the Monte-Carlo modelling used to simulate fragment distance distributions, a fundamental experimental observable in our case, which aids in the detailed understanding of the obtained data.

Further on, Chapter 5 follows from all the aforementioned discussions to finally trace the analysis details and infer the results aimed for through the experiment. Although the analysis is still ongoing at the time of writing this study, some of the major strategies and techniques used to arrive at the preliminary results and the path forward leading to final conclusions and possibly a pinning down of the DR energetics for the TiO^+ molecule have been elucidated. Following naturally from this, the interim results and inferences, including the intricacies yet to be accounted for to concretely arrive at the culmination of this experimental venture have been outlined in the final Chapter 6.

E_{KER} for the relevant low-energy states				
Initial state	**Product state**			$\boldsymbol{E_{\mathrm{KER}}}$ [meV]
TiO^+-index	O-index	Ti-index	E_{f} [meV]	$(E_{\mathrm{i}} - E_{\mathrm{f}})$
0	0	0	0.0	0.0
	1	0	19.6	-19.6
	0	1	21.0	-21.0
	2	0	28.1	-28.1
	1	1	40.6	-40.6
	0	2	48.0	-48.0
	2	1	49.1	-49.1
	1	2	67.6	-67.6
	2	2	76.1	-76.1
1	0	0	0.0	26.2
	1	0	19.6	6.6
	0	1	21.0	5.2
	2	0	28.1	-1.9
	1	1	40.6	14.4
	0	2	48.0	-21.8
	2	1	49.1	-22.9
	1	2	67.6	-41.4
	2	2	76.1	-49.9

Table 1.3: Demonstrative table for the expected kinetic energy release E_{KER} for the relevant low-lying electronic energy levels for the initial ionic molecule and neutral product species. Noteworthy are the major assumptions considered, viz. a) the molecule has no initial rotational and vibration excitation, b) the reaction energy $\Delta E = 0$, and c) electron-ion collision energy $E_{\mathrm{cm}} = 0$, which consequently yield 'negative' values for the E_{KER} which are only demonstrative.

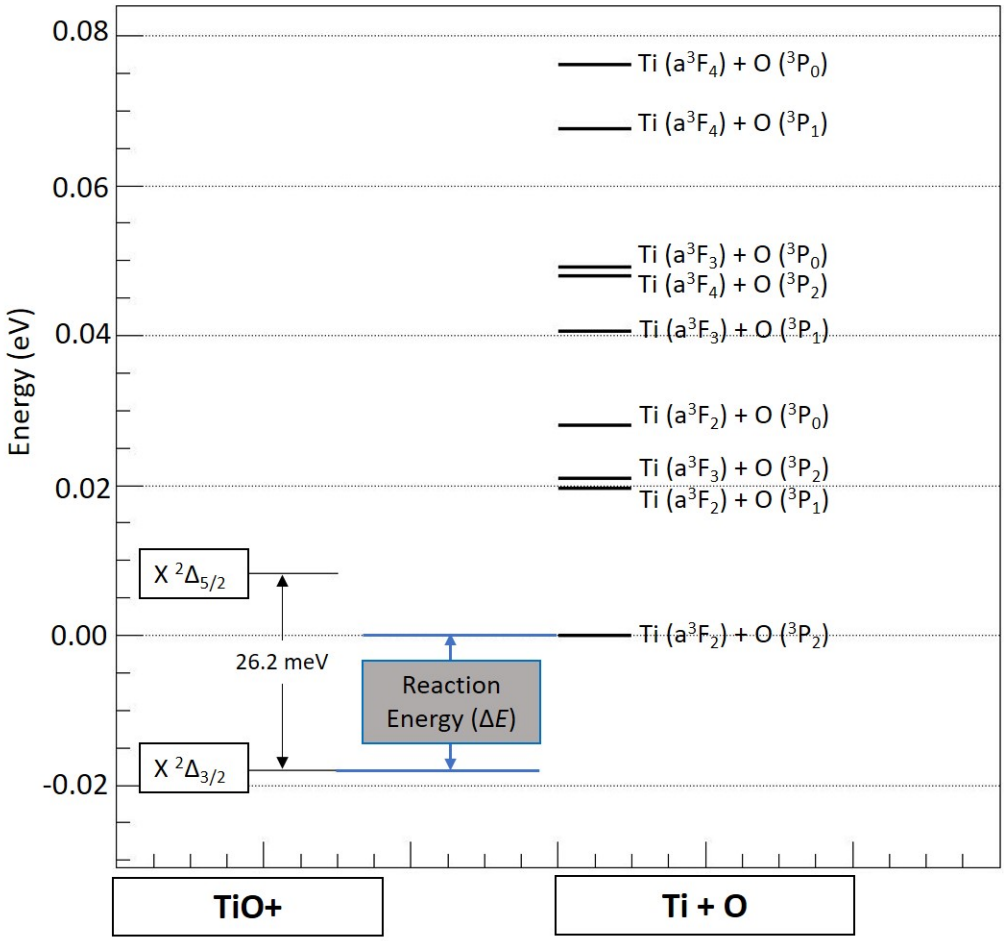

Figure 1.4: An electronic energy level schematic for TiO^+ and the DR product fragments (Ti + O), disregarding the rotational and vibrational levels for simplicity. The ground states have been used as the reference or zero for both the energy ladders and the difference between these can be used to define the energetics of the reaction, ΔE, a primary aim of this work.

Chapter 2

Experimental Apparatus and Techniques

The experiment undertaken as a part of this work involves a plethora of intricate techniques and involved developments on state-of-the art experimental apparatus present at the Max Planck Institute for Nuclear Physics (MPIK), in Heidelberg. A succinct overview of the relevant details of the setup and crucial techniques involved, including the production of cold electron beam, optimisation and characterisation of low kinetic temperatures, ion bunching, beam cooling and other diagnostic strategies, forms the subject matter of this chapter. An insight into the theoretical treatment of the particle dynamics in a storage ring has been presented to better discuss the electron-ion merged beams technique implemented at the eCool section, wherein the targeted recombination experiment has been performed. This is complemented by a brief overview of the electron cooling technique that the eCool section is exceedingly crucial for, elucidating the need and advantages of the same. Finally the principle and working of the neutral fragment detection system has been presented, along with a general overview of the elaborate measurement scheme used at the eCool section in context with its customisation entailed in this work.

2.1 The electrostatic Cryogenic Storage Ring (CSR)

The Cryogenic Storage Ring (CSR) at the MPIK in Heidelberg is a 35.12-meters electrostatic storage ring capable of storing ions with energies ranging from 20 keV upto 300 keV, per unit charge, in a uniquely designed environment [5]. The figure 2.1 shows a schematic of the facility. The CSR is capable of stably supporting cryogenic temperatures down to 2 K along the whole structure. This is possible due to the layered structure of the ring, comprising of the inner experimental beam tube with the ultra-high vaccuum levels measured upto pressures as good as 10^{-14} mbar. This is surmounted by the isolation vacuum chamber, further covered by two stages of radiation shields and the cryostat. The beam tubes

have been covered with high-purity copper to reduce the thermal gradients. The cooling to cryogenic conditions is enabled by a helium refrigerator system, with a network of cooling lines distributed strategically to circulate gaseous and liquid helium in majorly 2 K, 5 K, 40 K and 80 K stages. The temperatures of the experimental chambers are monitored using PT1000 sensors (inaccurate below 35 K) and a smaller number of RhFe sensors to measure lower temperatures.

The experimental structure of the ring is composed of four field-free symmetrical straight sections of 2.6 meters each, with equal sets of ion-optical elements in each corner, consisting of two quadrupole electrodes, two 6° minor bending electrodes and two 39° major bending electrodes. The ion beam production and acceleration is performed separately from the ring on a floating-potential source platform, and the appropriately energetic ion beam is transported through a transfer beamline to the CSR at the injection corner. Named in an anti-clockwise fashion from the injection corner, three of the four straight sections (A, B, D) have been dedicated for experiments, and one (section C) is dedicated exclusively for beam diagnostics.

The cryogenic temperatures realised in the ultra-high vacuum environment proffer fundamental advantages due to the cryo-adsorption of low-mass gases, allowing for long storage times (lifetimes on order of a few thousands of seconds) even for low-energy (keV) molecular ions. The CSR design ensures that the vacuum vessels and beamline elements are kept in the line-of-sight of the stored ions which, strictly limits the thermal black-body radiation in the experimental chambers, facilitating the infrared-active molecules to radiatively deexcite and equilibrate to the lowest energy levels over the long storage times. This is particularly important in the study of molecular ions, as in the objective of the current work, given that the low excitation energies are crucial for understanding the reaction at the desired level of a few meV energy resolution, which would otherwise not be possible in a room temperature environment. Further, storage rings provide for excellent implementation of the technique of merged beams (see sec. 2.4), which when coupled to the principle of 'recycling' of the stored particles, leads to repeated interactions with the target for each turn, also allowing for high effective ion-beam currents and state-selective reaction study. Two major types of MCP-based detector systems have been installed in the CSR to study these molecular reactions– the COld MOvable PArticle CounTer (COMPACT) that can be used to detect the charged particles that leave the stored ion trajectory, and the Neutral Imaging in Cold Environment (NICE) detector (see sec. 2.6), equipped to measure the neutral product fragments with position sensitivity. The imaging experiments carried out as a part of this work are based off the NICE detector system and have been discussed later.

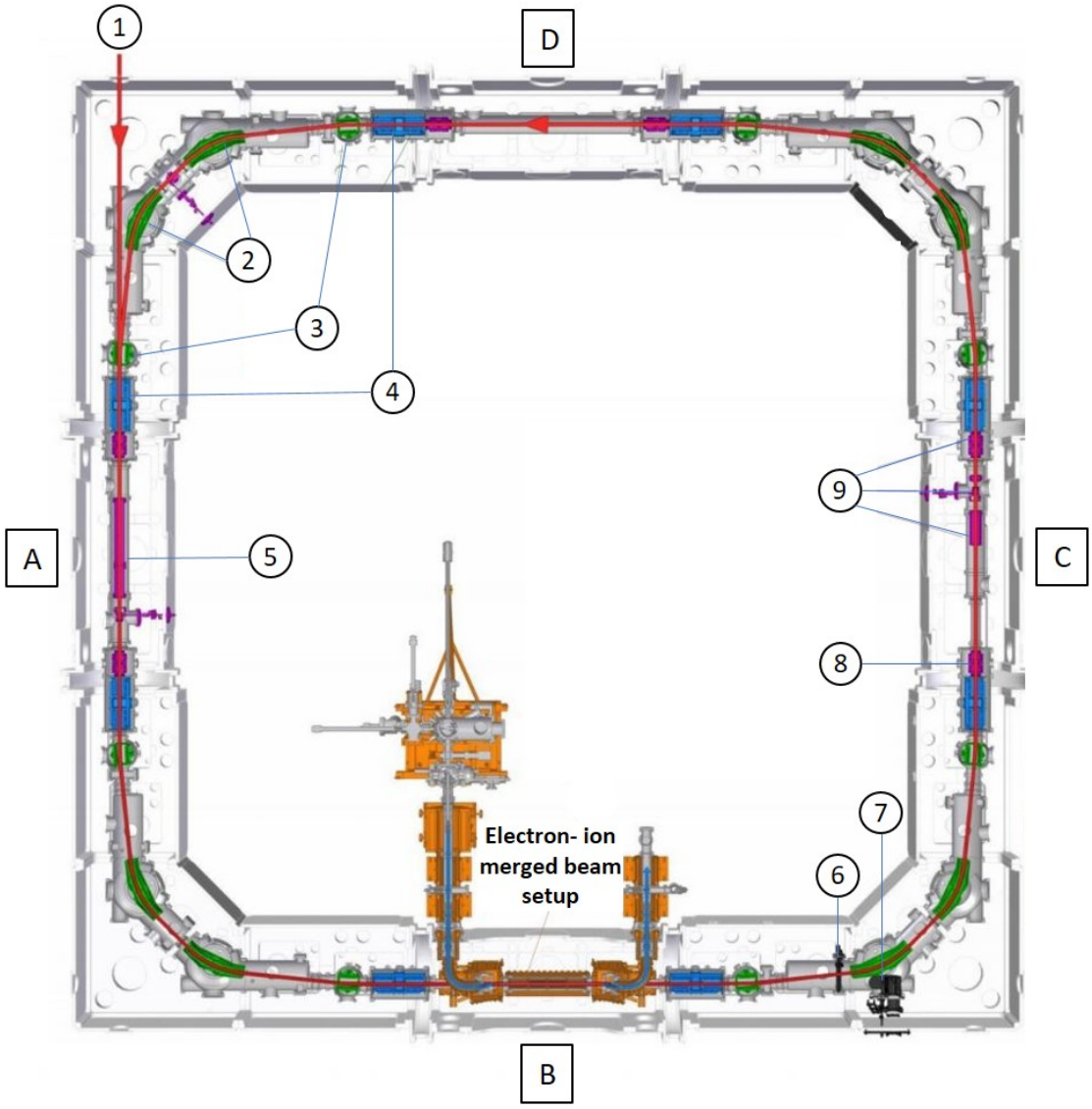

Figure 2.1: Overview of the CSR. The ion beam is injected at (1) and confined to a ∼35 meter closed orbit by electrostatic ion-optical element sets of 6° deflectors (2), 39° deflectors (3), and quadrupole focusing doublets (4), placed symmetrically at the four corners. Section A houses the ion-neutral beam experiment, along with an RF-bunching system (5) for beam bunching in the ring. Section B features the electron cooler (eCool) section, with the COMPACT charged particle detector (6) and the neutral imaging detector NICE (7). Section C is reserved for beam diagnostic elements such as the position pickups (8), the Schottky, and current pickups (9). Section D is designated for the reaction microscope setup.

2.2 Ion storage

A storage ring is based on clever manipulation of electromagnetic fields using electrodes placed at strategic positions, called as the ion optical elements, to keep the ions within a closed orbit, constantly keeping in check various quality parameters of the beam. We deal with the theoretical treatment of the particle dynamics involved in the storage of an ion beam at the CSR [5] in beirf, on the lines of earlier works [51, 52] in this section.

The concepts of storing ions in a storage ring are fundamentally based on the application of the Lorentz forced experienced by charged particles under the influence of electric or magnetic field, given as:

$$\vec{F_L} = q.(\vec{E} + \vec{v} \times \vec{B}) \tag{2.1}$$

Under proper manipulation of the electric field ($\vec{E}$) and/or magnetic field ($\vec{B}$) strength, this can be used to confine a particle beam of mass m, and charge q, with a specific velocity $\vec{v}$. An important consequence to note here is that while the effect of electrostatic elements is based on the energy of the ion, the magnetic elements interact with the ion according to its momentum, when being driven around an arc, elucidated by the respective rigidity definitions given as:

$$r_m|\vec{B}| = \frac{mv}{q} = \frac{p}{q}; \quad r_e|\vec{E}| = \frac{mv^2}{q} = \frac{E_{kin}}{q} \tag{2.2}$$

where r_m and r_e represent the bending radii in the two cases. This makes an electrostatic storage ring more robust in terms of switching between various ion species with different masses but unchanged kinetic energies. In case of maximal allowed velocity for a given field strength, electrostatic storage ring gives a $v_{max} \propto m^{-1/2}$ dependence, and the magnetic analog yields $v_{max} \propto m^{-1}$. The absence of magnetic fields fundamentally improves the situation as electric fields are comparatively easier to control, do not have hysteresis, remnant fields, or eddy currents. Furthermore it also reduces the chances of unintentional stimulated transitions for the circulating ions, making the electrostatic storage rings a favorable alternative, as used in this work.

2.2.1 Phase-space ellipse

The behaviour of the stored ion beam particles is addressed using a six-dimensional phase-space representation, given that the particle dynamics are manifested in the physical three-

dimensional space. The ion-optical elements in the ring are tuned according to the so-called *reference particle* or *design particle*, which is assumed to follow an ideal and deterministic trajectory along the closed orbit of the storage ring. Chosen a position, s, along the design orbit in the ring, the design orbit intersection with the cross-section defines the origin of the left-handed curvilinear coordinates for the stored particles, as depicted in figure 2.2. Here the transverse coordinates are x, and y, at an arc length s defined with respect to a reference point (**0**) along the ring's closed orbit.

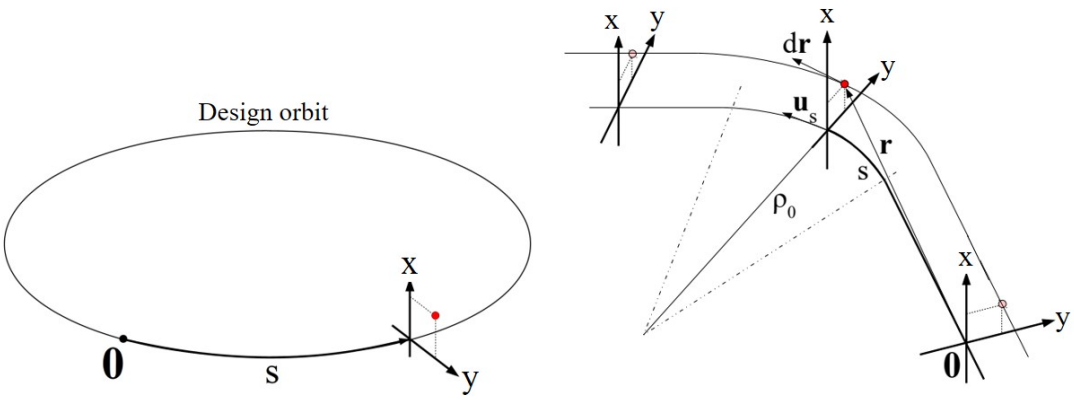

Figure 2.2: Curvilinear coordinates defined for the stored ion beam with respect to the design orbit; image adapted from [53].

For complete definition of a particle in phase space, it is plausible to use the straightforward position and linear momentum coordinates – (x, x', y, y', s, s'). However, a more instructive approach involves the system by a vector defined as:

$$\vec{x}(s) = \begin{pmatrix} x \\ x' \\ y \\ y' \\ l \\ \delta \end{pmatrix} \tag{2.3}$$

where x and y are spatial coordinates defined as the spatial deviations from the design orbit, with their corresponding linear momenta denoted by x' and y':

$$x' = \frac{\mathrm{d}x}{\mathrm{d}s} = \frac{p_x}{p_0}, \quad y' = \frac{\mathrm{d}y}{\mathrm{d}s} = \frac{p_y}{p_0} \tag{2.4}$$

where $p_{x,y}$ define the particle momentum along the transverse directions, and p_0 is the momentum of the design particle along its orbit. Further, it is instructive to define the rest two coordinates as angular deviation from the design particle in the form of the path length difference l, and relative momentum deviation as:

$$l = -v_0(t - t_0), \quad \delta = \frac{p - p_0}{p_0} \tag{2.5}$$

where p is assumed to be the particle momentum, at a time t, when it passes a certain point s, while the quantities with the subscript 0 are defined for the design particle.

Consider for a single particle's phase space coordinates in one dimension, viz. x and x'. In a conservative field environment and decoupled degrees of freedom along other directions, the particle is expected to follow the path along the boundary of the ellipse described by the initial conditions of the particle. If the many-particle picture is considered in case of a beam, the phase-space ellipse is filled with various particles occupying points inside the ellipse area. This particle dynamics obey the law of conservation of the area inside a phase-space ellipse called *beam emittance*, in accordance with the corollary of Liouville's theorem (see section 2.5), generally stated for a completely defined Hamiltonian with all active forces accounted for within. The shape of the phase-space ellipse may evolve depending on, for instance, coordinate s along the closed orbit when the transversal interactions are considered.

The beam-emittance describes the crucial characteristics about the beam such as the beam size and beam divergence. A beam of particles may be represented in a phase space diagram as a cloud of points within the closed contour, usually an ellipse, generally described by [54],

$$ax^2 + 2bxx' + cx'^2 = \epsilon \tag{2.6}$$

where a, b, c and ϵ are ellipse parameters that determine the shape and orientation of the ellipse (see fig 2.3). The application of the equation 2.6 in two dimensional phase space yields, a compact notation in form of 2×2 matrix,

$$\sigma = \begin{pmatrix} \sigma_{11} & \sigma_{12} \\ \sigma_{21} & \sigma_{22} \end{pmatrix} = \epsilon \begin{pmatrix} c & -b \\ -b & a \end{pmatrix} \tag{2.7}$$

Using the equation 2.7, beam emittance can be defined for both the transverse directions x and y analogously. It is helpful to note that the diagonal elements represent the maximum

spatial ($x_{\max} = \sqrt{\sigma_{11}}$) and angular deviations of the beam ($x'_{\max} = \sqrt{\sigma_{22}}$) (similar relations hold for y). Further, the beam emittance is defined by the determinant of σ, smaller value for the latter implies a smaller spread around the central design particle.

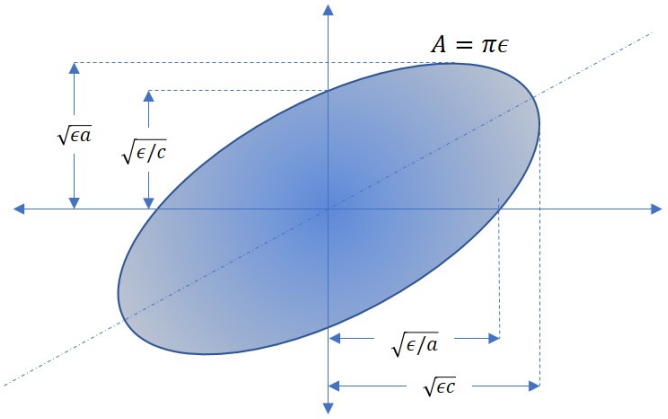

Figure 2.3: Representation of the phase space ellipse as described by the equation 2.6; adapted from [54].

2.2.2 Transverse beam dynamics

Stored ions moving inside the ring are influenced by the periodic lattice conditions created by ion-optical elements to guide particles along closed orbit. This effect can be modelled using the Lorentz force acting on the particles, with the initial parameters given by the position and momentum coordinates in the (x, y)-plane, considered as a function of the elemental length ds on the reference orbit. This modelling results in the equations of motion resembling set of equations used in astrophysical context first and thus named after the astronomer G.W. Hill [55]:

$$\begin{aligned} \frac{\mathrm{d}^2 x(s)}{\mathrm{d}s^2} + k_x(s)x(s) &= 0 \\ \frac{\mathrm{d}^2 y(s)}{\mathrm{d}s^2} + k_y(s)y(s) &= \frac{\delta}{\rho_0(s)} \end{aligned} \tag{2.8}$$

where ρ_0 is described as the instantaneous curvature radius that the particle is bent around, as depicted in figure 2.2. The periodic conditions of the ring are reflected in the periodicity of the linear coefficients as $k_{x,y}(s) = k_{x,y}(s+C_0)$, with C_0 being the total closed orbit length of the ring. Naturally, the general solution of the differential equation set 2.8, resembles the pseudo-harmonic oscillator solution. This describes the characteristic transversal motion

of the particle in the storage ring, termed as the *betatron oscillations*, given as:

$$u_d(s) = \alpha_d \sqrt{\beta_d(s)}\, \cos(\Psi_d(s) + \Psi_{0,(d)}) \tag{2.9}$$

Here, $\alpha_d \sqrt{\beta_d(s)}$ gives the amplitude of the oscillations, $\Phi_d(s)$ is the phase of oscillation, wherein d subscript represents one of the two transverse directions x or y, with an initial condition offset given by Φ_0.

With the knowledge of betatron functions in the transverse directions, it is possible to calculate the number of full betatron oscillations a particle performs in one turn along the ring circumference, as:

$$Q_{x,y} \coloneqq \frac{1}{2\pi} \oint \frac{\mathrm{d}s'}{\beta_{x,y}(s')} \tag{2.10}$$

The quantity Q is an important figure named as the *Q-value* or the betatron tune value. The tune values (Q_x, Q_y) of the storage ring define its so-called *working point* in the given conditions. It is important to note that integer or half-integer values of $Q_{x,y}$ result in resonances where any perturbations of the ideal orbit by dipole or higher order multipole errors become synchronized with the betatron oscillation. Such a perturbation can be caused, for instance, by a field imperfection of the storage ring's focussing elements or deflectors. During the operation of a storage ring, one generally uses a resonance diagram (also called working diagram or tune diagram) to identify possible working points, carefully avoiding these tune resonances.

Another important quantity is the relation between the momentum spread of the stored beam and the revolution frequency f, termed as the *phase slip factor* (η). This arises from the Hill's equations which suggest that a momentum spread $\frac{\Delta p}{p}$ of a stored beam affects its horizontal position y in the ring, which in turn, influences the closed orbit of the particle. Thus, the phase slip-factor relation is given as:

$$\frac{\Delta p}{p_0} = \frac{1}{\eta} \frac{\Delta f}{f_0} = \delta \tag{2.11}$$

which defines the relation in terms of the quantity spreads and the values for the design particle (denoted with the subscript 0).

2.2.3 Longitudinal beam dynamics

In order to understand the stored beam inside the ring, it is important to use credible diagnostics. One such idea that helps in characterisation of the stored beam uses a clever manipulation of the longitudinal particle dynamics in the ring. The technique is termed as *beam-bunching* wherein time-dependent voltage modulation is applied to a cylindrical drift tube electrode in the storage ring. The procedure aims at imprinting a time structure on the circulating ion beam and thus, transforms this coasting or dc-beam, into a bunched beam that is now composed of almost discrete ion pulses. These intense pulses of ions owing to their temporal nature can be efficiently detected non-destructively through diagnostic tools such as the Schottky and current pick-ups. In contrast to the betatron oscillations, beam bunching manipulates the particle dynamics longitudinally, interpreted using the angular coordinates, namely, path difference (l) and phase difference, with respect to the design particle (δ) defined as in the equation 2.5. The design particle considered here, called *synchronous particle*, is defined such that it always passes the drift tube center with the same phase Φ_0, and energy $E_0(t)$, and thus the RF-signal is synchronised to the synchronous particle revolution frequency as:

$$\omega_0 = \frac{\omega_{\mathrm{rf}}}{z} \tag{2.12}$$

where, ω_{rf} is the frequency of the RF-signal, and z is an integer. The RF-bunching brings in a coupling between the energy deviation, ΔE ($E - E_0$), and phase deviation, $\Delta\Phi$ ($\Phi - \Phi_0$) considered with respect to the synchronous particle. This coupling conserves the area of phase-space ellipse for the beam from the time and conditions when RF-bunching is switched on, as shown in figure 2.4. The behaviour of the beam, and within it, each particle is determined strongly by the RF characteristics (such as frequency, amplitude, etc.), along with the storage ring tune parameters. Empirically, the energy of a particle stays unchanged if it has $\Delta\Phi$ = 0. However, consider a particle with $\Delta\Phi > 0$. Particle dynamics dictate that it will gain energy due to the RF-field $\Delta E_{\mathrm{rf}}(\Phi)$ with each turn through the drift tube, thus increasing the velocity. This continues until eventually phase difference reaches a minimum at zero, while energy deviation reaches a maximum for the given initial condition. However, it is not a stable condition due to the high energy. This reverses the phase of the particle with respect to the synchronous case, and thus decreasing its energy with each turn until it reaches a minima, and the maximum possible phase difference $\Delta\Phi$. This essentially signifies an oscillatory behaviour around the synchronous particle, as can be seen in the ΔE versus Φ plot in the figure 2.4.

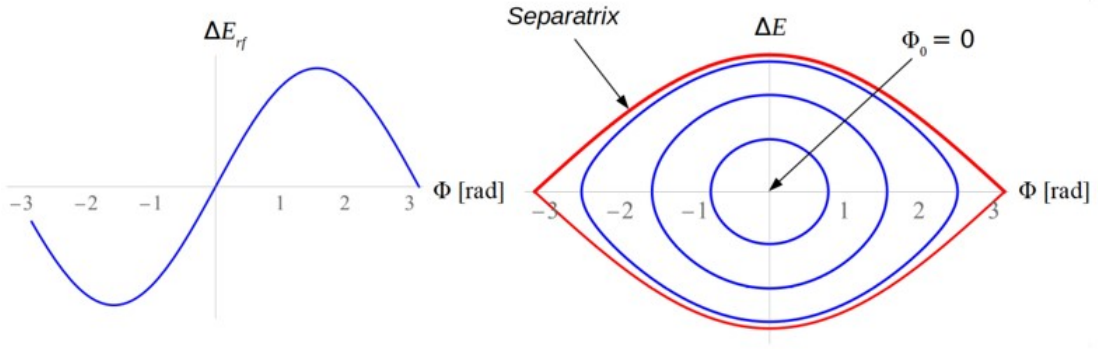

Figure 2.4: The energy gain per turn for a particle passing the bunching drift tube is a periodical function of the RF-phase, shown in the left curve. Right: stationary RF-bucket ($\Delta\Phi = 0$). The area border of the stable particle trajectories is marked by the *separatrix* (red curve), beyond which ions are lost out of the beam. Image adapted from the work of P. Wilhelm [53].

Detailed dynamics in the beam bunching are defined by the used RF voltage amplitude, ramp-up and ramp-down times on the drift tubes, length of the drift tube, etc. The fundamental frequency for bunching of a given beam in the settings at the ring can be calculated preliminarily and found more precisely by experiments. Once at the correct frequency (or its harmonics), the peaking bunching signal against the noise can be detected on current pickups and seen to sustain longer. As this procedure is extremely sensitive to the frequency used for bunching (to the level of a few tens of Hertz), it can also be used as a tool for precisely determining the revolution frequency of ion beam stored in the ring.

2.3 The electron cooler section (eCool)

One of the straight arms of the CSR, section B according to the figure 2.1, is dedicated to the low-energy electron cooler (eCool) section, an exceedingly intricate setup spanning an approximate length of 1.3 meters. With implementation of merged-beams technique (see sec. 2.4) for the electron and ion beam, it can serve as an electron cooler viable for phase-space cooling of the ions (see sec. 2.5), as well as an electron target feasible for probing into electron-induced reactions for atomic and molecular species, under the designated measurement conditions.

The eCool has been designed for efficiently probing into lab-frame electron energies as low as 1 eV with high accuracy. This translates to the capability of achieving extremely low relative energy conditions for the electron-ion system (see sec. 2.4, 2.5), with ion

masses upto 160 u stored in the ring with 300 keV energy and energy resolution of $\sim$1 meV. Making it a unique characteristic, such low energies also mandate strict electron beam confinement conditions over the span of the eCool, and thus a strong magnetic field region is set up through the cooler using copper-coiled solenoids in the room-temperature region and superconducting solenoids in the cryogenic region, in various stages. There are also multiple correction/steering elements placed along the beam path which help in gaining a better control over the beam, as well as effectively performing the electron-ion beam overlap, as has been highlighted later.

A schematic of the eCool section in figure 2.5 marks the electron beam path, along with the typical longitudinal magnetic field amplitudes through the section. At one end, a high density electron beam is first produced with considerably low energy spreads (kinetic temperatures $\sim$300 K) as compared to the conventional thermal electron sources ($\sim$1000 K), at the cold electron emitter bank (CEEB– see 2.3.1). The CEEB is embedded in a high-field solenoid typically operated at fields of 3000 Gauss in this work. These longitudinal magnetic fields enable better confinement and stability for the low energy beam, and must have a certain minimal strength in order to suppress the heating effects such as the transverse-to-longitudinal relaxation (TLR) and the blow-up due to the Coulomb repulsion. Upon leaving the high-field solenoid, the electrons enter a field of typically 200-250 Gauss created by smaller copper solenoids. This is the area of the first magnetic expansion of the electron beam by an expansion factor α_1 = 15. The beam is then guided into the cryogenic region through a toroidal solenoid where electrons experience a 90° bend and get in a parallel orientation with respect to the ion beam orbit.

The electron beam merging, as shown in the figure 2.5, with the ion beam inside the CSR is then accomplished by a 30° bend downwards in the toroid with a simultaneous second magnetic expansion (α_2 = 2). This vertical bending is realized by four HTS racetrack coils, two of them positioned above and two of them below the ion beam orbit ("merging vertical" coils). This brings the beam in the interaction region where the magnetic fields are typically 100-125 Gauss strong and the ion and electron beams are finally collinear. In a similar manner the electron beam is later demerged (and magnetically compressed), and guided to the outside of the CSR cryostat. This beam can finally be collected by an analyzing Faraday cup setup on the other side of the eCool (collector side), which can be used for electron beam diagnostics.

It is instructive to note that the magnetic systems outside of the CSR cryostat (production and collection region) are built from water-cooled copper coils. In contrast, the merging and interaction regions are inside of the CSR cryostat which only use the high

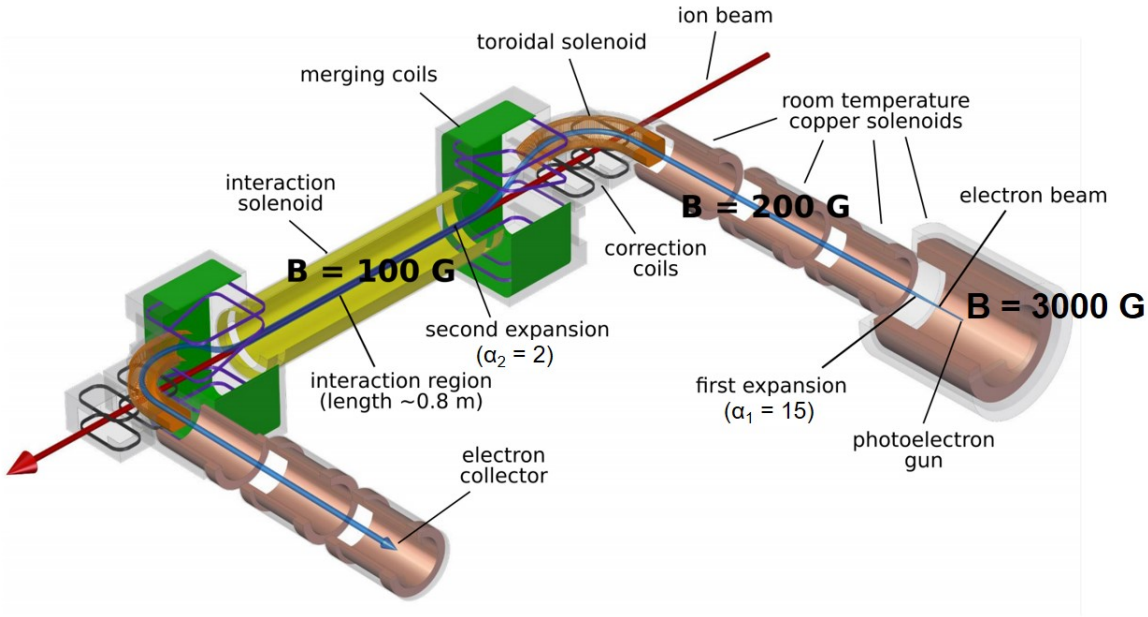

Figure 2.5: The electron cooler (eCool) design schematic adapted from the work of S. Vogel [56].

temperature superconductors (HTS) coils to avoid any heating due to current dissipation.

Apart from the major guiding field settings, there are also various positions along the eCool where it is possible to correct for the direction of the electron beam locally using magnetic fields produced by correction/steering coils as it traverses from the CEEB (gun) to the collector side. The room temperature gun side X and Y steering coils ('R.T. Gun' X/Y) are present near the low-field solenoid (see brown in figure 2.5). Further, as the beam moves in the toroidal section in the CSR, there are correction coils ('Gun Toroid' X/Y) which can be used to adjust for toroidal drift while the beam makes a 90° horizontal turn. Moving forth, vertical merging coils are present where the electron beam is finally merged with the ion beam ('Gun Merging' X/Y) wherein correction is possible. Finally in the interaction region, there are two long magnetic correction coils (Interaction X/Y) which may be used to change the electron beam angles in the region (with respect to the initial position of entry) to get a better overlap with the ion beam. At this point near the interaction region is also the starting point of the *drift-tube*, that spans through the interaction zone. The drift-tube, divided in 11 separate electrodes, is a crucial element in the section that can be used to set/adjust the designated electron beam energy for the intended electron-ion interaction in an alternate mode of operation, termed as the drift-tube mode, discussed in section 2.7. Following the end point of drift tube, a symmetric set of correction/steering coils are present in the de-merging section, albeit with the dipole fields pointing in the

opposite fashion, called the collector side correction coils (analogous to the gun side). This arrangement similarly guides the electron beam out from the cryogenic section, and towards the end of the eCool where, with a Faraday cup, the emergent electron beam can be monitored.

2.3.1 Cold electron emitter bank (CEEB)

At the ultra low meV electron-ion collision energies targeted with the CSR electron-ion merged-beam setup, the electron beam profile and temperature plays a crucial role for the achievable energy resolution. In most applications, electrons are produced by heating a thin metal wire that stimulates thermionic electron emission. The electron energy distribution in this case is directly dependent on the cathode temperature (on the orders 10^3 Kelvin, corresponding to $\sim 10^2$ meV energy spread) when high electron currents are produced. Consequently, in order to generate cold electrons at the eCool, electron beam generated from a semiconductor GaAs photocathode electron source, the CEEB, developed as a part of the work by Orlov et al [57]. The specially produced *p*-doped GaAs semiconductor is first activated by deposition of monolayers of Cesium and Oxygen. This process is continuously monitored and is repeated in cycles until the quantum efficiency of the cathode being illuminated by a low power laser starts to saturate. This process leads to a so-called *negative electron affinity* surface-state of the CEEB, wherein according to the proposed mechanism, the vacuum level at the surface is reduced below the conduction band minimum [58]. In the conduction band, electrons thermalize into a Boltzmann distribution that is defined by the temperature of the crystal and drift towards the crystal surface. Since this means that the temperature distribution of electrons depends directly on the photocathode temperature, the eCool section also has the feature of cooling the cathode to liquid nitrogen temperatures during measurements to reach extremely low electron energies. An electron can then escape into the vacuum by tunneling through the thin potential barrier created by the (Cs,O) layer. This can happen either directly, or after they lose energy in processes like scattering with the surface defect states or even by interaction with phonons. In the latter case, electrons leave the crystal with a much broader energy distribution as shown in figure 2.6. The extraction of electrons from this electrode is done by shooting a high power infrared laser at the back of the CEEB which is covered with a Sapphire glass. This cathode is fit inside a electron gun assembly designed in 'Pierce' geometry majorly responsible for proper shaping and spread of the beam. The cathode is held at a potential $-U$ with respect to the ground which defines the acceleration voltage of the electrons. Then extraction and

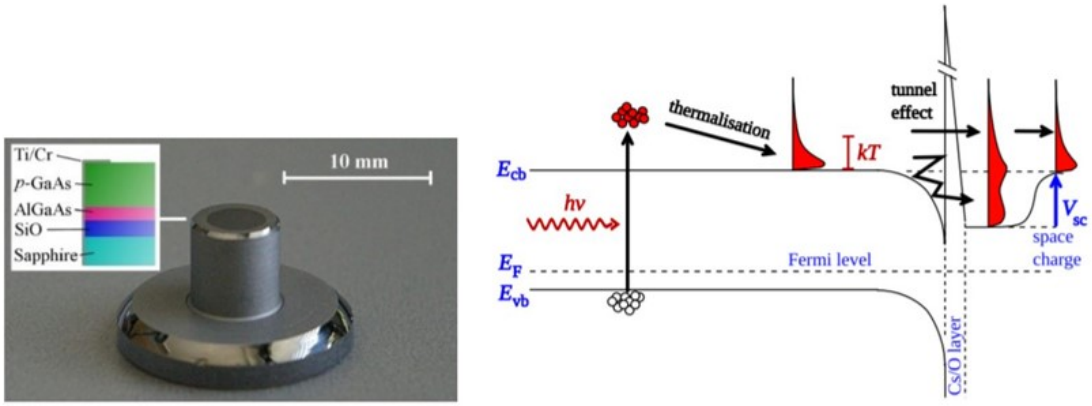

Figure 2.6: CEEB outside the electron gun assembly (left). Band diagram of the GaAs CEEB with deposited layers of Cs and O. Image adapted from PhD thesis by P. Wilhelm [53].

Pierce electrodes are adjusted keeping the cathode voltage as floating ground, and define the beam shaping parameters.

Two modes of electron extraction are possible for the electron gun. In the *current-limited mode*, high extraction voltage or low laser intensities result in the extraction of every electron that is emitted from the crystal surface. The emitted current does not depend on the extraction potential, but is defined by the laser intensity and the quantum yield of the CEEB. In the *space-charge limited mode*, the electron current I_e that can be extracted from the cathode is related to the extraction voltage U_{ext} by the Child-Langmuir law as:

$$I_e = pU_{ext}^{3/2} \tag{2.13}$$

where the Perveance *p* is a gun geometry-dependent parameter, typical value for which in the operational mode of CEEB is 0.5μ A/V$^{3/2}$. Operating in this mode the electron beam is independent of any fluctuations of the laser intensity as well as degradation of the CEEB surface layers which may affect the quantum yield. However, high laser intensities and low extraction voltages cause the accumulation of an electron cloud in front of the crystal surface. Very slow electrons are blocked by this potential and the energy distribution of the extracted electrons in this mode is given by their initial distribution in the bulk GaAs cathode, as excited in the conduction band initially. The space-charge potential becomes a limiting factor for current increase from the CEEB, especially critical at low electron energies, as in our case. However, as shown in eqn. 2.33, the electron density is central for the cooling force, as well as a decisive parameter determining count rate in a recombination

experiment. For a given gun geometry, as highlighted in the work of A. Shornikov [59], the only way to improve the current density is to extract the electrons from the source at a higher energy and then to decelerate the beam to the required energy. This scheme is the basis of the drift-tube operation mode at the eCool, discussed in 3.2.1.

The typical electron currents extracted in the operational conditions used in space-charge limited mode range within 5-50 micro-Amperes (μA), while the currents used in the measurements for the current work were $\sim$5 μA, representing an electron number density $n_{\mathrm{e}} \sim 4 \times 10^5$ electrons/cm^3 at the lab-frame energy of 2.4 eV (cooling energy). The CEEB is a unique feature of the eCool setup which has not been used in this capacity elsewhere, and gives a very reliable low-energy electron beam.

2.3.2 Electron beam temperature reduction

It is imperative to understand the velocity distribution of the electron beam in the electron-ion merged beam section, as it determines the precise collision energies taking part in the reaction with the ion beam. The velocity distribution is also needed to deconvolve the measured recombination rates to specify the reaction cross-sections [30], along with properly using the technique of electron cooling (see sec. 2.5), both of which are strongly dependent on the kinetic temperature of the electron beam. We elucidate the treatment of kinetic temperture of the electron beam, and further discuss the methods used to effectively reduce these velocity distributions in the transverse and longitudinal directions.

Directly after emission from the CEEB, the velocity distribution for the electron beam is assumed to be isotropic in the longitudinal and transverse directions. As the electrons in the eCool section are guided by a longitudinal magnetic field, owing to the Lorentz force (eqn. 2.2) the particles' motion can be segregated into a translation parallel to the field lines and a rotation around the same. Consequently, the energy spread in the longitudinal and transverse directions can be considered separately using the kinetic temperatures $T_{\parallel}$ and $T_{\perp}$ respectively. Invoking the treatment as in the Kinetic theory of gases, the electron beam temperatures can be defined by the mean of the beam velocity distribution along each axis direction. Also using the equipartition theorem, and coupling the transverse directions (X

and Y) due to the symmetry, the electron beam kinetic temperatures are given by:

$$\frac{1}{2}k_{\mathrm{B}}T_{\parallel} = \frac{1}{2}m_e\Delta_{e,\parallel}^2, \quad \text{and} \tag{2.14}$$

$$k_{\mathrm{B}}T_{\perp} = \frac{1}{2}k_{\mathrm{B}}(T_x + T_y)$$

$$k_{\mathrm{B}}T_{\perp} = \frac{1}{2}m_e\Delta_{e,\perp}^2 \tag{2.15}$$

where the transverse and longitudinal electron velocity spread $\Delta_{e,\parallel}$ and $\Delta_{e,\perp}$, are taken to be the σ_{v_z} and $\left(\sqrt{\sigma_{v_x}^2 + \sigma_{v_y}^2}\right)$ respectively.

Transverse temperature

The transverse electron temperature can be efficiently reduced using the adiabatic transverse expansion technique [60]. If the electron beam is transferred longitudinally from a region of high magnetic field strength (B_i) to a low field (B_f) region, it is expected that the magnetic field lines are not parallel anymore, but slowly diverge due to the field gradient, thus decreasing in density. However, the magnetic field gradient induces a non-zero longitudinal component of the Lorentz force on the electron. While the electron undergoes a cyclotron motion about the field lines with a frequency given by:

$$\omega_c = \frac{eB}{m_e} \tag{2.16}$$

this can be used to estimate the distance travelled by the electron in one revolution, that is:

$$\lambda_c = 2\pi\frac{v_{\parallel}}{\omega_c} = 2\pi\frac{m_e v_{\parallel}}{eB} \tag{2.17}$$

If the longitudinal field variation over this length λ_c is small in comparison with the total field ***B***, i.e.

$$\left|\frac{\mathrm{d}B}{\mathrm{d}z}\right| \frac{\lambda_c}{B} \ll 1 \tag{2.18}$$

the condition can be termed as adiabatic, wherein the ratio of the mean electron beam energy in the transverse direction, $\langle E_{\perp}\rangle$, and the total magnetic field strength B, i.e. the quantity $\langle E_{\perp}\rangle/B$ remains a constant in the electron beam. Thus, if the initial magnetic field B_i is scaled by the expansion factor α, to a field strength B_f in accordance with the

adiabaticity measure, it follows from the above discussion that,

$$\alpha = \frac{B_i}{B_f} = \frac{\langle E_{\perp,i} \rangle}{\langle E_{\perp,f} \rangle}$$
$$\implies T_{\perp,f} = \frac{T_{\perp,i}}{\alpha} \tag{2.19}$$

which depicts the observable decrease in transverse temperature of the electron beam. The adiabatic invariance also implies the conservation of the magnetic flux through a given electron beam radius in cylindrically symmetric field conditions. The decrease in the magnetic field strength, thus, also leads to transverse expansion of the beam, given by:

$$R_f = \sqrt{\alpha} R_i \tag{2.20}$$

where R_i and R_f denote the electron beam radius in the two regions under consideration. Given that the electron number is conserved, this also implies a decrease in the number density within the beam by a factor α. Given that the electron density is crucial for the experimental statistics and electron cooling process (see section 2.5), this constrains the extents of expansion factor, α.

Longitudinal temperature

Following the emission from CEEB, the electron beam is produced with an isotropic velocity distribution. While the transverse beam temperature is improved using the adiabatic magnetic expansion technique as discussed before, in order to optimize the longitudinal temperature, consider a technique wherein the electron beam is simultaneously accelerated by a potential difference U_e. To observe the effect of this, first, we note the electron longitudinal energy in the lab-frame,

$$E_{lab,\parallel} = \frac{m_e v_\parallel^2}{2} + eU_e \tag{2.21}$$

where, m_e and e represent the electron mass and charge. In another inertial frame moving with a velocity only defined by the potential difference used to accelerate the electron, i.e. $(2eU_\mathrm{e}/m_\mathrm{e})^{1/2}$, assume that the electron velocity is given by $v'_\parallel$. While the kinetic energy of the electron in this moving frame is simply given by $E' = \frac{1}{2} m_\mathrm{e} {v'_\parallel}^2$, we can transform this

to calculate the kinetic energy in the laboratory frame to yield,

$$E_{lab,\parallel} = \frac{1}{2} m_e \left(v'_\parallel + \sqrt{\frac{2eU_e}{m_e}} \right)^2 \tag{2.22}$$

Comparison of the electron velocity as defined in the two reference frames, as in eqn. 2.21 and 2.22 leads to,

$$v_\parallel^2 = {v'_\parallel}^2 + 2\, v'_\parallel \sqrt{\frac{2eU_e}{m_e}} \tag{2.23}$$

It is important to note here that the potential difference U_e is chosen to match the electron velocity with the ion beam velocity. Thus, considering now an electron beam picture, which when accelerated by the same potential U_e, results in a mean velocity given by $(2eU_\mathrm{e}/m_\mathrm{e})^{1/2}$ ($\gg v'_\parallel$), the relation for a single electron can be approximated as,

$$v'_\parallel \approx \frac{v_\parallel^2}{2\sqrt{\frac{2eU_e}{m_e}}} \tag{2.24}$$

Extending the idea to a thermal ensemble of electrons with an initial kinetic temperature $k_\mathrm{B}T_\mathrm{cath}$, which is then accelerated by a potential U, yields the relation [61],

$$k_\mathrm{B}T_\parallel = \frac{\left(k_\mathrm{B}T_\mathrm{cath}\right)^2}{2eU} \tag{2.25}$$

for the final longitudinal temperature $T_\parallel$ in the relevant inertial frame of reference co-moving with the velocity close to the mean ion beam velocity. This kinematic compression holds good in the approximation of a non-interaction beam of particles, considered as an ideal gas, which is valid at the typical particle densities in our case.

2.4 Electron-ion merged beams technique

The eCool section has been designed such that it can serve as an electron-cooler and an electron target for ion beam interactions in the CSR [29]. This is facilitated by the use of *merged-beams technique*, wherein two interacting beams of particles are made to travel along a common axis for some finite distance [62, 63]. The principal advantage of this method lies in the ability to access low center-of-mass energies with two fast collinear beams having similar velocities in the the lab frame. Thus, it can be used to study interac-

tions between particles with very low relative energies and high-energy resolution. Given that the interaction region between the beams extends upto $\sim$1 m in the case of the CSR, this imbues the possibility to study reactions involving short-lived or highly reactive beam species, and transient effects.

Consider the case of electron and ion beams with speeds $v_{\rm e}$ and $v_{\rm i}$ intersecting at an angle Ω, where their relative speed $v_{\rm r}$ is given as,

$$v_r = |\vec{v_e} - \vec{v_i}| = (v_e^2 + v_i^2 + 2v_e v_i \cos\Omega)^{1/2} \tag{2.26}$$

wherein, the relative energy in the center-of-mass frame, $E_{\rm r}$, is

$$E_r = \frac{1}{2}\mu v_r^2 \approx m_e \left[\frac{E_e}{m_e} + \frac{E_i}{M} - 2\left(\frac{E_e E_i}{m_e M}\right)^{1/2}\cos\Omega\right] \tag{2.27}$$

where, $\mu = m_e M/(m_e + M) \approx m_e$ is the reduced mass for the electron-ion system, while $E_{\rm e,i}$ and m_e, M are the ion and electron energies (in the lab-frame) and masses respectively. It is noteworthy that for the case $\Omega = 0^\circ$, i.e. perfectly merged beams, the condition

$$\frac{E_{\rm e}}{m_{\rm e}} = \frac{E_{\rm i}}{M} \tag{2.28}$$

yields $E_{\rm r} = 0$, implying that two fast beams in the laboratory frame can be merged and made to interact at essentially zero relative energy. Although zero relative velocity can make the definition of ion-electron collisions tricky, it is to be noted that in practice, Ω can never be made identically zero for all the beam particles due to the beam temperatures arising from the source, and divergence due to the focusing elements in the storage ring. Nevertheless, the velocity distributions and angular spreads of the beams are optimised in the experimental setup to reach as close as possible to the zero mean relative energy condition.

At the CSR, the mean ion beam energy, $E_{\rm i}$ is typically of the order of a few hundred keV and is kept stable through a given experiment/measurement. The mean electron beam energy is used as a variable for the experimental conditions which can be tuned by manipulating the potentials of the electrodes in the beam path to reach very low energies (see chapter 3). These energies are usually calculated and tuned with respect to the $E_{\rm r} = 0$ condition, as mentioned in eqn. 2.28, wherein, the corresponding electron energy in the lab-frame is termed as the *cooling energy*, $E_{\rm cool}$. The rationale for the term and further discussion is a part of the section 2.5. The collision energy for the electron-ion system in

the center-of-mass frame is calculated using 2.27 for perfectly merged condition, $\Omega = 0°$, which can be expressed as,

$$E_r = \frac{1}{2}\mu \left|\vec{v}_r\right|^2 = \frac{1}{2}\mu \left(v_e - v_i\right)^2 = \frac{1}{2}\mu \left(\sqrt{\frac{2E_e}{m_e}} - \sqrt{\frac{2E_{\mathrm{cool}}}{m_e}}\right)^2$$
$$E_r = E_d = \left(\sqrt{E_e} - \sqrt{E_{\mathrm{cool}}}\right)^2 \tag{2.29}$$

where, the equation 2.29 defines the quantity *detuning energy*, E_{d}, which is the mean collision energy for the electron-ion beam in the center-of-mass frame calculated for perfectly collinear beams, while the quantities on the RHS, E_{e} and E_{cool} are the set energies for the electron beam and cooling (velocity-matched condition) in the lab-frame.

2.5 Electron cooling

The quality of an ion beam can be described using the beam emittance along with the momentum spread, as has been discussed in the section 2.2. In order to perform precise measurements on electron-ion system, it is imperative to understand and optimize on the quality parameters of the ion beam. One powerful method to do this is by employing *phase-space cooling* of the stored ions using electrons as has been discussed below.

Phase-space cooling is a general technique used to improve the stored ion-beam quality in storage rings by aiming at the reduction of beam cross-section, angular deviations and the momentum spread by extracting energy from the system. The principle can directly be related to a compression of the phase-space ellipse for the stored beam. This also means to a contraction of the physical expanse of the beam towards the central orbit, which not only localizes the reaction origin, but also increases the beam lifetime inside the storage ring. It has been mentioned previously in section 2.2 that beam emittance is a constant of motion for a stored beam, in accordance with the Liouville's theorem which states, *the density of particles in the six-dimensional phase space is conserved under the influence of conservative forces*. Naturally, the influence due to the ion-optical elements are through electromagnetic interactions, which can only alter the shape of the beam. However, this limitation can be overcome using a second overlapping beam which, if replenished continuously can provide an exit pathway for the energy, from the system under consideration.

The method of electron cooling proposes the use of a cold electron beam as a sympathetic beam to carry the heat out of the stored ions. Figure 2.7 shows a schematic of the

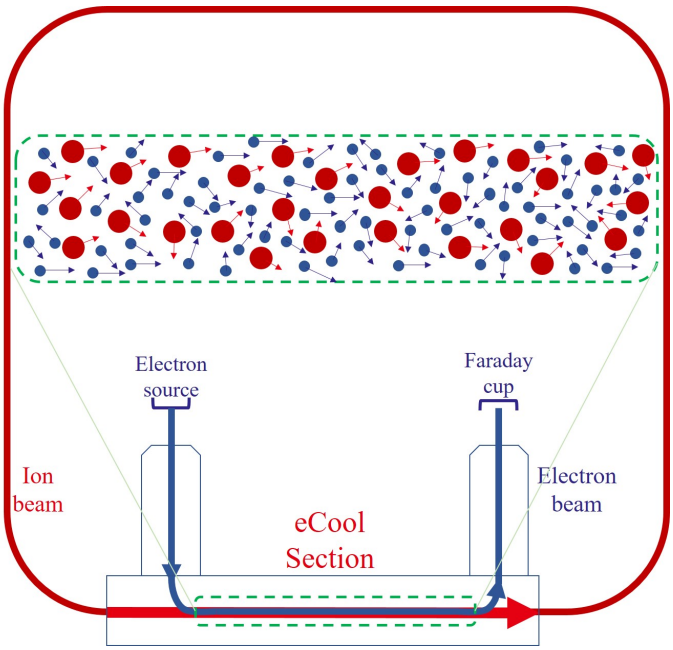

Figure 2.7: Electron cooling principle schematic– the cold electrons (blue) are generated continuously at the CEEB, directed to and merged with the ion beam (red), and then demerged after the interaction region towards the collector with a Faraday cup at the end. The Coulomb interaction between the two beams averages to yield a thermalization effect in the electron-ion plasma, achieving the phase-space cooling of stored ion beam in the CSR.

idea as implemented at the eCool in the CSR. The cold electrons produced at the CEEB are made to overlap with the stored ion beam for a given interaction length, and are subsequently deflected out from the ring again. The initial condition of the beams is considered to be a Maxwell-Boltzmann distribution according to the initial temperatures as T_i and T_e, for ions and electrons respectively. This yields the mean thermal velocities of the particles in the center-of-mass frame to be,

$$\langle v_{e,cm} \rangle = \sqrt{\frac{k_{\mathrm{B}} T_e}{m_e}}, \qquad \langle v_{i,cm} \rangle = \sqrt{\frac{k_{\mathrm{B}} T_i}{M}} \tag{2.30}$$

where k_{B} is the Boltzmann constant, m_e the electron mass, and M represents the ion mass. As the electrons and ions interact due to the Coulomb interaction, the momentum transfer to the electron can be calculated according to the binary collision model as:

$$\Delta p = \frac{1}{4\pi\epsilon_0} \int_{-\infty}^{\infty} \frac{Ze^2}{x^2 + b^2} \mathrm{d}t = \frac{2Ze^2}{4\pi\epsilon_0 v_r b} \tag{2.31}$$

Here, b is the impact parameter, and v_r is the relative ion velocity in the electron's frame of

reference. The given treatment considers only the transverse component of the Coulomb force, since the longitudinal force component averages out to be zero over an interaction region through which the ion drifts. The corresponding energy transferred to the electron is given by,

$$\Delta E(b) = \frac{-(\Delta p)^2}{2m_e} \propto \frac{Z^2}{v_r^2} \tag{2.32}$$

It is to be remarked here that since molecular ions cannot be easily produced in charge states larger than one, as this results in the severing of chemical bonds, factor Z remains immaterial, whereas the factor v_r can be used to optimize the energy transfer. Further, this energy transfer can be used to model the situation wherein the ion passes an electron cloud with a given density n_e, by appropriately integrating over the relevant range of impact parameter b, deduced by using the Debye length in the electron-ion plasma (introduces a factor L_C, addressed as Coulomb logarithm). This yields an expression of the effective force obtained from the energy exchanged between the electron-ion system,

$$\vec{F} = -\frac{2\pi n_e}{\mu}\frac{2Z^2e^4}{(4\pi\epsilon_0)^2}\frac{\vec{v_r}}{v_r^3}L_C \tag{2.33}$$

here, μ is the reduced mass of the electron-ion system, and L_C is the Coulomb logarithm. It is important to note that until now the energy spread in the electrons has been neglected. Following from the equation 2.30, electron temperature is distributed according to the following distribution function,

$$f(\vec{v_e}) \;=\; \frac{1}{\pi^{3/2}\sigma_{v_e}^3}\exp(-\frac{(\vec{v_e} - \langle\vec{v_e}\rangle)^2}{\sigma_{v_e}^2}) \tag{2.34}$$

$$\text{where,} \quad \sigma_{v_e} = \sqrt{\frac{2k_{\mathrm{B}}T_e}{m_e}} \tag{2.35}$$

Now, the relative velocity v_r is defined as $(\vec{v_e} - \vec{v_i})$, where the velocities in the latter expression are defined in the lab-frame. Consequently, the force due to the cooling model (eqn. 2.33) can be defined as a convolution with the electron velocity distribution, yielding:

$$\vec{F} = -\frac{4\pi n_e Z^2 e^4}{\mu(4\pi\epsilon_0)^2}\int L_C(\vec{v_e} - \vec{v_i})f(\vec{v_e})\frac{\vec{v_e} - \vec{v_i}}{|\vec{v_e} - \vec{v_i}|^3}\mathrm{d}^3v_e \tag{2.36}$$

Thus, it can be noted here that the force experienced by the ions is 'frictional' in nature, tending to decrease the velocities as they increase in amplitude v_r. It can also be noted that

smaller the energy spread of the initial electron beam, better would be the ion cooling as the distribution function $f(\vec{v_e})$ would statistically boost the cooling force. Clearly exhibiting the intuitive idea that a colder beam of electrons leads to a stronger cooling force.

As mentioned earlier, since the overlapping beams can be considered as an electron-ion plasma, this can be used to estimate proportionality on the experimental variables on the cooling times on the basis of plasma thermalization model [64] giving,

$$\tau_{cool} \propto \frac{MT_e^{3/2}}{n_e Z^2} \tag{2.37}$$

where M is the ion mass, and Z the ion charge, while n_e and T_e define the characteristics of the eelctron beam. The τ_{cool} represents the time constant for the thermalization process for the electron-ion plasma, with the assumptions that the T_i is much greater than T_e, and ion mass is comparatively much greater than the electron mass. It is important to note that in a storage ring, physical effects like residual gas collisions, intra-beam scattering and interactions with a potential internal target, lead to heating up of the ion beam, irrespective of any other effects, but only dependent on the experimental conditions. Thus, it is to be remarked that the cooling times τ_{cool}, must not be too large on the comparative scale to achieve a desired result. Further, for a fixed electron beam temperature, a lower initial ion beam temperature converges exponentially towards it with the time constant τ_{cool}. Also, as this technique depends strongly on the relative beam velocities, the best cooling conditions are obtained at the velocity matched conditions, i.e. $v_i = v_e$, which is further optimised by a perfectly overlapping condition of the beams.

2.6 Neutral fragment detection technique

The electron-ion recombination yields neutral products which are the primary experimental observables. The detection of these fragments takes place using the Neutral fragment Imaging detector in the Cryogenic Environment (NICE), which was developed and implemented as a part of the work by A. Becker [65]. This section describes some fundamental characteristics of the detector system relevant in context of the current work.

The NICE system is based on a microchannel plate (MCP) detector used in chevron configuration, backed by a phosphor screen (P-screen) anode setup used for imaging (see fig. 2.8). MCP- detector is based on the principle of impact-based secondary electron emission from the sensitive detector surface. This first emission is sequentially intensified by the further collisions of the produced secondary electrons (following a quasi-Poissonian

distribution) which are directed onto the path within the micro-channels in the detector using a high voltage across the front and back surfaces of the MCP. In earlier studies, it has been observed that MCP-based detectors perform well in cryogenic conditions [66], as well as along with P-screen [67]. As a characteristic of the MCP detector, at high-gain operational conditions, the total number of electrons in the avalanche converges towards an upper bound defined by the space-charge screening of the accelerating potential, resulting in a narrow pulse height distribution on anode. However, it is to be noted that due to the semi-conducting nature of the microchannel walls, the MCP resistance shows a strong increase at low temperatures which, in turn, increases the recharge times of individual channels after an electron avalanche has been triggered. This places a higher limit on the maximum particle rates which can be detected by the system in cold environments, thus NICE detector is operated in a heated mode at $\sim$35 K. In operational mode, for typical count-rates in a few kHz regime, NICE allows for an accurate measurement of the particle impact positions by determining the position of fast-decaying light spots produced on the P-screen due to the impinged electron cloud. The spot positions on the P-screen are recorded using a fast-camera system coupled to the screen using a suitable optical arrangement. The fast-camera is capable of capturing a frame size of 1280×1024 pixels of 14×14 μm size and 8-bit resolution, with a frame rate of approximately 10 kHz, while the practical limits are imposed by the camera-DAQ interface, allowing for acquisition at 1 kHz at a reduced resolution of 512×512 pixels. The electronic pulses generated on the anode are digitized appropriately, and generally used as fast-camera triggers with a specified exposure time, also recorded for later analysis. The frame grabber of the camera and the digitizer run independently, simultaneously, and the generated trigger signal is processed by a field programmable gate array (FPGA) circuit to trigger the read-out of both data acquisition systems [65].

To optimize the data acquisition, images from the fast-camera are analysed online and the significant information is compressed according to an efficient algorithm developed by the group. The algorithm is primarily used to identify fragment-hit spot coordinates and the related characteristics from a given frame snapshot wherein the impinged electron cloud creates a luminous spot on the P-screen. The routine systematically traces through the frame along X-direction row-wise, moving on to next column in steps along Y pixels. Once a high-intensity pixel above a certain set brightness amplitude threshold is found, a square-box of predetermined size (decided at the beginning of the measurement) is created around the pixel. This selected area is considered as a fragment-spot, wherein the routine records the spot amplitude and intensity (integral) as seen in the box in the pixel-space,

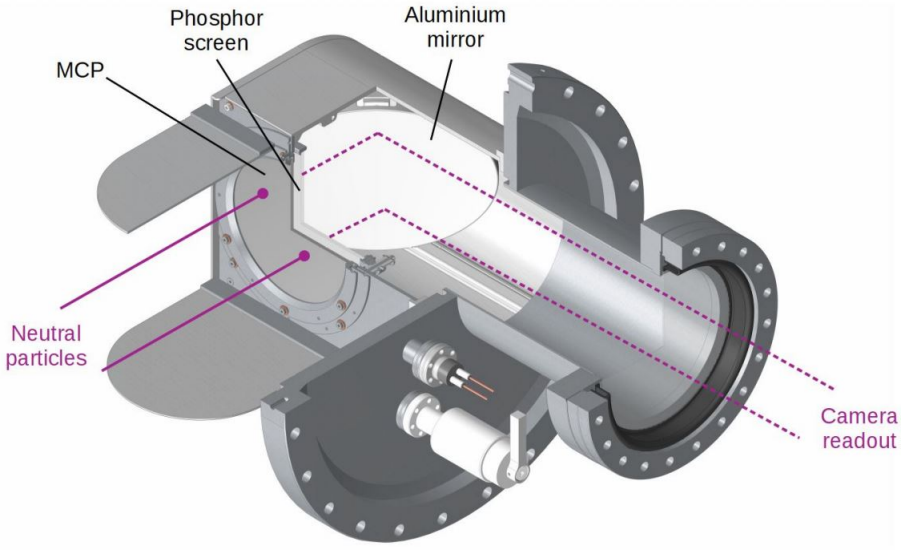

Figure 2.8: Model of the neutral fragment imaging detector for cold environment (adapted from [65]).

resets the values of those selected pixels to zero to avoid double-counting, and then moves further on in the frame to find other possible spots until the whole frame has been scanned. Each frame capture is done following a trigger, for a set exposure time duration (typically 2 μs), and is thus considered as a single event recorded as such with the significant quantities stored (see table 4.2 for a detailed list).

It is to be remarked here that the NICE detector system is capable of 3-dimensional fragment imaging, wherein the transverse coordinates can be recorded directly on the MCP as discussed above, while the longitudinal separation between the fragments can be calculated using the relative timing signals. The 3D separation between the product fragments resulting from a DR reaction is dependent on the energetics of the reaction manifesting as the kinetic energy of the products. For a diatomic molecule, this relation is given as:

$$d_{\mathrm{3D}} = \frac{D}{v_{\mathrm{i}}}\sqrt{\frac{2E_{KER}(m_1+m_2)}{m_1 m_2}} \tag{2.38}$$

where, D is the distance between the dissociation point for the molecule and the detector plane, v_{i} is the stored ion velocity in the ring, E_{KER} is the kinetic energy release (KER) in the reaction resulting into product fragments with masses m_1 and m_2. This requires the use of electron pulse timing and spot position correlation technique as recorded on the anode. However, this mandates that the difference between the time-of-flight for the

product fragments stays appreciable (> 10ns), which is not the case for this study, and thus the principle is out of the scope for current discussion. In this scenario, the transverse (2D) fragment distance on the detector remains as the fundamental experimental observable, the maximum value for which, for a given D and E_{KER}, is the same as the expected 3D distance as in eqn. 2.38. A study of the realistic manifestation of 2D fragment distances resulting from a reaction is central to this work, and has been discussed in detail in section 4.3.

2.7 Measurement Scheme

The measurement scheme employed at eCool uses the technique of energy wobbling which has been successfully used in previous DR investigations [29, 30, 68]. Here, once the ion beam has been produced at the source, it is accelerated to the required energy U_{acc} and transported to the CSR injection section. The measurement is functionally seen as a sequence of identically designated injection cycles, as has been discussed further.

An injection cycle is commenced by a trigger pulse that stimulates the injection electrode, following which an ion pulse is allowed to enter the ring. Given all electrostatic fields applied in the CSR, the ion beam dilutes to a continuous coasting beam within <5 ms, stored in the ring with a mean energy U_{acc}. At this stage, the ion beam can be allowed to cool radiatively by revolving around in the CSR as it is for a designated time period. For performing electron-induced measurements, the electron beam is switched on and the set collision energy, E_d is wobbled at a relatively rapid rate according to a pre-defined scheme for data taking steps. Using the equation 2.29 for E_d, to set E_{e} in lab-frame, the collision energy can be cycled through four different steps: $E_d = E_{\mathrm{cool}} = 0$ (*cooling* step), $E_d = E_{\mathrm{d,m}}$ (*measurement* step), $E_d = E_{\mathrm{d,r}}$ (*reference* step), and electron-beam *off* step. A sequential combination of these steps constitutes a scheme, multiple cycles over which defines the injection measurement cycle. The first step maintains the phase-space cooling of the ion beam at zero collision energy, while the second step generates designated conditions for the aimed DR measurement. The reference step is generally set for a high detuning energy, E_d, where the DR cross-section is expected to be extremely low, therefore yielding a credible measure for the background counts relevant for rate determination for the recombination. Lastly, the off-step is usually placed at the end of a scheme to measure the event counts due to ion collisions with residual-gas background in the CSR. Each step in the measurement scheme is designated a time duration, which, in our case, typically spans a few tens of milliseconds. Given that the electron energy is changed rapidly, a fast and stable four-quadrant power supply is used for the purpose, and a settling time of 5 ms

is allocated following every step in the scheme wherein the electron beam is switched off. After iterating over the scheme for a determined number of times (typically 1000 cycles) for a given injection measurement, the ion beam is dumped after which the counts can be measured on the detector for a time duration to determine the dark count rate. This finishes an injection cycle, and a new ion beam injection in the CSR can be made, following a similar measurement procedure from scratch. An example of a measurement scheme cycle has been shown in figure 2.9.

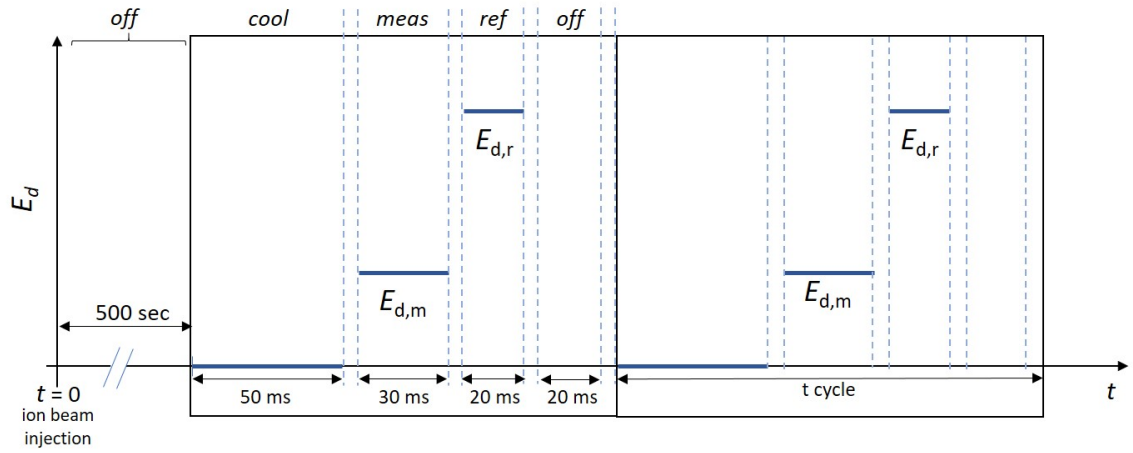

Figure 2.9: Measurement scheme cycle used for a typical experiment, wherein the ion injection happens at $t = 0$, and the ions are stored in the ring with electrons-off for 500 sec. Following this, electron-induced recombination measurement is begun. The box represents a single cycle for the defined scheme: cooling step (50 ms) – measurement step (30 ms) – reference step (20 ms) – off step (20 ms), each separated by a wait-time (electron-beam off) of 5 ms. This scheme is cycled for a set number of times during a measurement run, following which the ion beam is dumped and another injection cycle starts from scratch.

A single measurement run constitutes multiple of such injection cycles with the same settings. The whole measurement is handled using a data-acquisition system with the capability of synchronising the set parameters and trigger signals with the acquired detector data with a timing resolution of $\sim$10 ns (dependent on the trigger-width), and with pulse timing resolutions of $\sim$1 ns. The recorded data from each injection measurement run is primarily separated for segregating different run settings, and for the purpose of efficient data handling, and limiting individual file size for further analysis.

Chapter 3

The TiO^+ Experimental Beamtime

The fundamental objective of this work is based on the study of dissociative electron recombination reaction for the TiO^+ molecule as elucidated in Chapter 1. The aimed experiment was performed in December 2019 beamtime at the eCool section of the CSR facility at MPIK. A detailed discussion of the preparations, implementation and conditions leading up to and prevalent at the time of the aforementioned experiment forms the subject matter of this chapter. We start with a brief discussion of the source used for ion production, including the analysis of the ion beam composition as used in the experiment. This is followed by an exhaustive summary of the crucial conditions and set parameters for the storage ring, electron cooler section and the detector assembly, general discussions of which have been addressed in Chapter 2. Furthermore, the measurement scheme for the experiment has been outlined along with the relevant modelling and physical estimates to consolidate the reasoning. A detailed interpretation of the acquired data and the progression of analysis have been explored in the Chapters 4 and 5.

3.1 Ion production

The production of a pure ion beam for the molecular ion under consideration, TiO^+, was done using an in-house sputtering Penning ion source built based on the design by Z. Nouri et al. [69], developed as a part of the work by F. Nüsslein at MPIK. The Penning ionisation source works on the principle of gas discharge [70], structurally consisting of a hollow anode cylinder, surmounted by a concentric cylindrical cathode shell, with a titanium sputter target placed along the anode axis. Crucial to the design is a high axial magnetic field, which confines the discharge electrons to a cycloidal motion along the axis, increasing the chances for collisions with the target, and forms the fundamental working principle for the source. In the operational mode, a potential of $\sim$1 kV is applied between the cathode and

anode, and a noble gas (such as Argon, ^{40}Ar) is introduced in the system, which gives rise to a weakly ionised quasi-neutral plasma, aiding ionisation from a solid target. To form the targeted metal oxide, the noble gas is mixed with Oxygen (^{16}O) in a definite proportion, optimised for the source's stable functionality and high ion yield. The produced ions are extracted by applying a potential between the extraction electrode and the cathode, following which an Einzel lens optimises the ion beam, finally leading out to the transfer beamline.

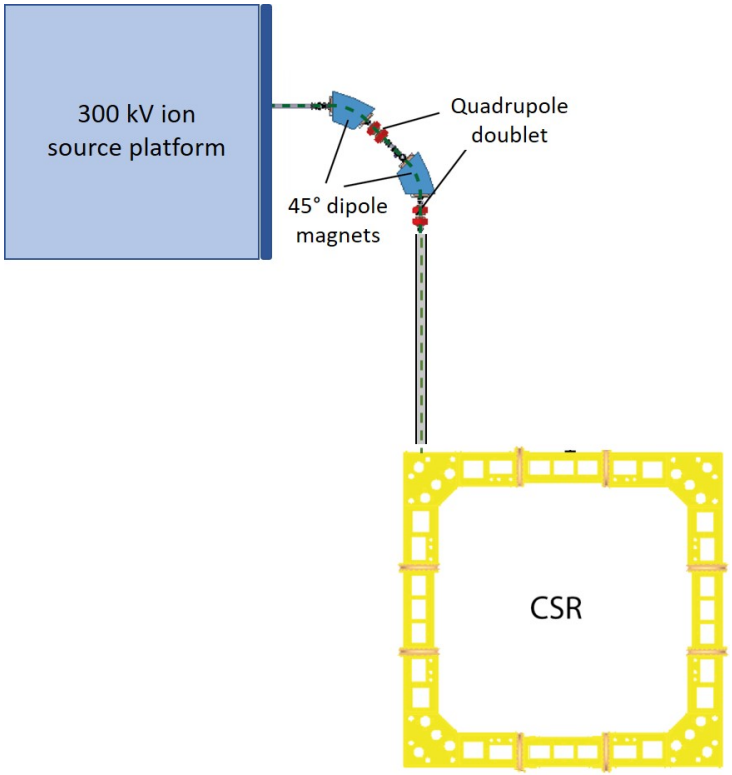

Figure 3.1: Simplified schematic for the transfer path from 300 kV ion source platform to the CSR. Ion beam path has been represented by the dashed green line.

A simplified schematic of the ion beam path at the experimental facility for CSR, at MPIK, has been shown in the figure 3.1. The aforementioned Penning ionisation source can be attached on the 300 kV source platform, which can be lifted to a floating potential U_{acc} (upto 300 kV) with respect to ground, set according to the required ion energy for the experiment. The extracted ions at the set energy are then transferred through the transfer beamline to the CSR wherein two 45° dipole magnets placed along the beam path can be used to mass-select the produced ions from the source on the basis of their magnetic rigidity ($\propto m/q$ see eqn. 2.2). However, this implies that other ions with similar magnetic rigidity can also pass through and enter the experimental ion beam. For our case of TiO^+ (molecular mass 63.9423 u) ion beam with m/q ~64 u/e, the other species which can be produced

by the source with similar m/q have been listed in table 3.1, where naturally occurring isotopes of titanium with respective approximate abundance viz., ^{46}Ti (8.3%), ^{47}Ti (7.4%), ^{48}Ti (73.7%), ^{49}Ti (5.4%), and ^{50}Ti (5.2%), may be present in the pure titanium target used. High purity ^{16}O is distinctly used in the production, while ^{1}H can be introduced from the residual atmospheric gases in the source. To better understand the composition of the ion beam, we use the fragmentation mass spectrum method as discussed further.

m/q **[u/e]**	**Molecular ion species**
62	$^{46}TiO^{+}$
63	$^{46}TiOH^{+}$, $^{47}TiO^{+}$
64	$^{47}TiOH^{+}$, $^{48}TiO^{+}$, O_4^{+}
65	$^{48}TiOH^{+}$, $^{49}TiO^{+}$

Table 3.1: A list of produced molecular ions from the source used in the experiment, tabulated with respect to the magnetic rigidity (see eqn. 2.2) proportionality parameter m/q. Here the molecular mass for specific Ti isotope involved has been mentioned, while the superscripts for ^{16}O and ^{1}H have been dropped for brevity.

Fragmentation mass spectrum

The mass spectrum for the fragmentation products of the molecular ion collision with a relatively inert gaseous target can be used as a probe to understand the molecular ion composition resulting from the source. The technique is implemented at the CSR by using the first 45° dipole magnet on the transfer beam-line (see fig. 3.1) to select the precursor (parent molecular ion) mass, 64 u in this case, while the second dipole magnet can be used to obtain a fragment mass spectrum. It is to be noted that the fragment mass energy (E_{frag}) dissociated from the parent molecular ion is given by

$$E_{\mathrm{frag}} = U_{acc}\frac{m_{\mathrm{frag}}}{m_{\mathrm{i}}} \tag{3.1}$$

where, m_{frag} and m_{i} are the fragment mass and precursor ion mass respectively.

The comparative fragmentation mass spectrum measured for magnetic rigidity corresponding to m/q= 62, 63 and 64 u/e has been presented in figure 3.2, recorded under identical conditions with a picoammeter range of 1 nA. The observed fragments are expected to correspond to the following species: TiH^{+}, Ti^{+}, O_3^{+}, TiO^{2+}, O_2^{+}, Ti^{2+}, Ti^{3+}, O^{+}, Ti^{4+}, and O^{2+}, with respect to the initial m/q selected. To understand the molecular

ion species produced with $m/q = 64$, it is imperative to estimate the contributions from ^{47}TiOH$^+$ [71], and O_4^+ which may contaminate the intended ^{48}TiO$^+$ ion beam. Results from the investigations in this context can be summarised as follows:

- **O_4^+ contribution**: Similar magnetic rigidity yields a molecular abundance peak at the same position as for TiO$^+$ in the mass spectrum. Fragmentation species for O_4^+ can be expected to exhibit O_3^+ (similar to ^{48}Ti$^+$, and ^{47}TiH$^+$), O_2^+ (similar to ^{48}TiO^{2+}), and O$^+$ (similar to ^{48}Ti^{3+}) contributions, which would appear at $m/q = 48$, 32 and 16 u/e respectively. However this should only occur for the precursor ion selection of $m/q = 64$ u/e (see black curve in fig 3.2), and not for others, given that we use highly pure O^{16} which only contributes to the said case. Here, it can be noted that the feature at $m/q = 32$ shifts in accordance with the change in precursor ion rigidity selection (green and blue curves), validating the presence of TiO^{2+} ion fragment. Further, on observing the intensity peak ratio between the TiO^{2+} and Ti^{2+} features in the spectrum for different precursor rigidity selections being identical, it can credibly be argued that O_2^+ ion specie makes up for a negligible fraction in the $m/q = 32$ u/e feature, given that the structures near $m/q = 24$ u/e are purely attributed to Ti^{2+}.

- **TiOH$^+$ contribution**: For a rigidity selection corresponding to each of m/q =62, 63 and 64 u/e, only one specific isotope of Ti can be involved to form a molecular ion with ^{16}O. However, in case of the presence of TiOH$^+$ in the original beam, an isotope of Ti, namely ^{47}Ti can take part in the ion formation cumulating to the same resultant rigidity as the target ion, TiO$^+$. This is evident in the figure 3.2 where the isotope peak for fragmented Ti$^+$ is visible as a strong feature for m/q= 63 u/e selection at the first magnet, as a merging shoulder for m/q= 64 u/e selection, and absent for m/q= 62 u/e selection due to the fact that no isotope combination in that case forms TiOH$^+$ ion. The high ion-current investigations suggest approximately 10% contribution from TiOH$^+$ species in the target beam of TiO$^+$. The effect of this contamination has been accounted for in the analysis (see sec. 5.3.2).

3.2 Measurement parameters

The measurement campaign dedicated to TiO$^+ - e^-$ recombination was aimed at understanding the energetics of the dissociative recombination (DR) reaction process for the molecule, along with the rate constant for the same. This was especially challenging, mainly due to the high ion mass, and extremely dense level structure for the molecular

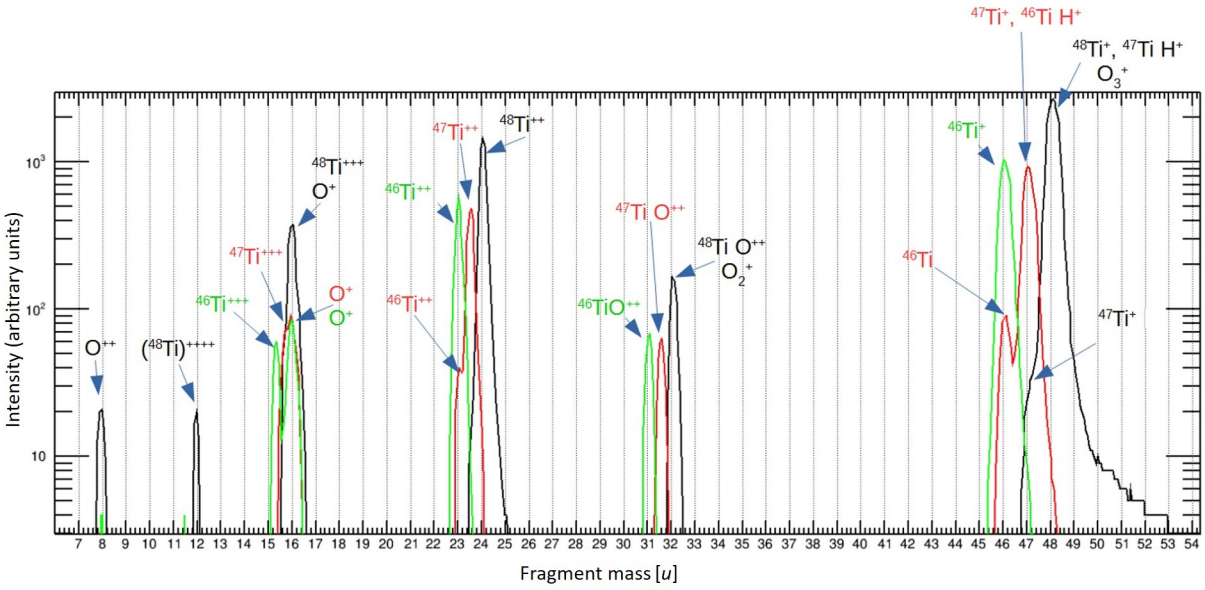

Figure 3.2: Recorded fragmentation mass spectrum for magnetic-rigidity based selected molecular ion species corresponding to m/q= 62 (red), 63 (green) and 64 (black) u/e.

system, implications for which have been highlighted further in the experimental progression and the analysis in this work. Following from the ion beam production (see sec. 3.1), a $\sim$20 nA strong ion beam was injected in the CSR with a mean beam energy corresponding to U_{acc} =279.81 keV. The ion number for a single injection in the CSR was kept steadily within $1-4 \times 10^6$ ions (at the start of the injection cycle) throughout the beamtime for the given conditions, and was measured using the RF-bunching technique as discussed in the section 2.2. It could be observed that the beam spread and injected ion intensity in the ring was sensitive to the ion optical arrangements in the transfer beamline, which were adjusted carefully to optimisation. Once injected, the ion optical elements in the ring sustained the Gaussian profile beam in a closed orbit, revolving at a frequency of 26.165 kHz. The final beam adjustments were done to optimise the ion beam size in the ring using various techniques, finally yielding a width within effective 6 dB-intensity of the ion beam as $\sim$13.4 mm.

Following this, the electron beam at the eCool was set up with typical electron beam currents of $\sim$5 μA obtained from the CEEB (refer to sec. 2.3.1). The electron beam size as at the interaction region conditions (low B-field as compared to production region), can be measured by scanning over the beam in the collector region using a pinhole aperture before the Faraday cup, which can then be used to calculate the conditions at the interaction region taking in consideration the effective expansion factor $\alpha = 30$ (refer to sec. 2.3), as was used

in this experiment. The scan measurement yields the electron beam data in various visualizations, produced in figure 3.3 is one representation for the beam conditions as observed in the experimental beamtime for $\alpha = 15$. It is to be noted that electron beam radius at

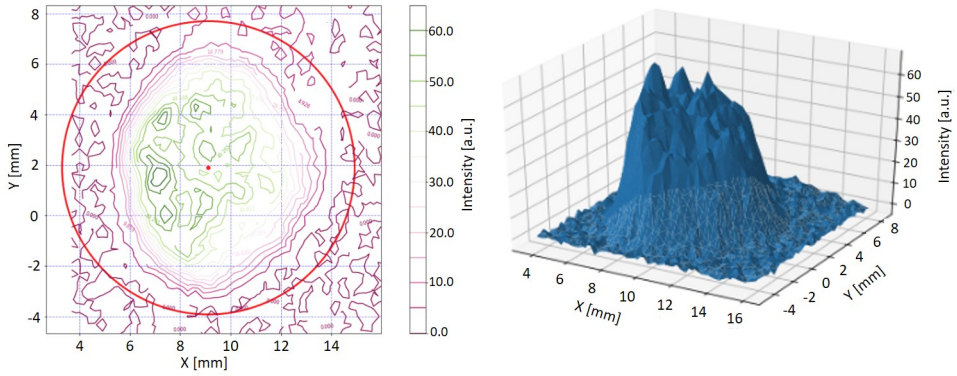

Figure 3.3: Plots depicting the electron beam profile measurements for $\alpha = 15$ from the beamtime in contour plot and intensity plot visualizations. The red circle in the contour plot represents the circular cross-section for the assumed radius of the electron beam in the interaction region corresponding to α =30, as in the recombination measurement conditions.

the production conditions, termed as the cathode radius, for the current measurement was measured to be 0.9465 mm. Considering the beam expansion in the interaction region, the beam physically inflates by a factor $\sqrt{\alpha}$, yielding an effective electron beam radius $r_{\mathrm{e}} =$ 5.184 mm. The electron number density in the beam at a set energy is given as,

$$n_e = \frac{I}{e \cdot \pi r_e^2 v_e} \,\mathrm{electrons/m^3} \tag{3.2}$$

where, I is the electron beam current, r_{e} the electron beam radius in the interaction region, v_{e} the calculated electron beam velocity in the lab-frame at set detuning energy E_{d}, and e, the elementary charge.

3.2.1 Setting electron beam energy

For an aimed detuning energy E_{d}, the electron energy in laboratory-frame can be set using two operation modes at the eCool (see sec. 2.3), namely the *standard mode*, and the *drift-tube mode*. A functional potential energy schematic for the two has been produced in figure 3.4. The standard mode requires that the cathode voltage (U_0) at CEEB be set to the required negative potential (according to the aimed electron beam energy), and the beam

can then be accelerated with respect to ground. In cases of low electron-beam energy, however, the current density is limited by the space-charge limited mode of operation, as highlighted in section 2.3.1. This issue can be dealt with by using the drift-tube mode of operation, wherein the electron beam is produced at a higher energy and then decelerated to the required energy further in the setup. The procedure effectively increases the Perveance (see eqn. 2.13) of the system in consideration which now includes the drift tube setting. The mode implementation involves setting a voltage U_{kep} with respect to the cathode voltage U_0, at the drift tube electrodes, which are placed in the interaction region of the eCool, ultimately defining the electron beam energy in the lab-frame. It is noteworthy that for both modes of operation, the electron energy in the interaction zone is given by the potential difference between the cathode and the drift tubes.

In this experimental study, given the high molecular mass and $\sim$300 keV energy ion beam, required collision energies demand electron beam energy on the order of a few eV in the lab-frame, consequently the drift-tube mode of operation has been used. The electron beam was first generated at the CEEB with the cathode voltage $U_0 = 23$ V, with extraction and Pierce electrodes set to 7.1 V and 2.6 V respectively, extracting a current of $\sim$6.7 μA. In order to implement the wobbling scheme (see sec. 2.7) for measurement, the U_{kep} was used to rapidly set the required electrode potentials, accordingly decelerating the $\sim$23 eV energetic incoming electron beam from the CEEB.

3.2.2 Cooling voltage search

The merged beams technique employed at eCool allows for setting electron-ion collision energies down with a resolution of meV. To achieve the required accuracy, it is imperative to find the velocity matched conditions for the two beam precisely, according to the eqn. 2.28, for the electrons with respect to the given ion beam conditions. As mentioned in the section 2.5, electron cooling for stored ions is optimal for the velocity-matched conditions (see eqn. 2.33), and thus we refer to this condition as the *cooling energy*, E_{cool}. For the given case of 280 keV TiO^+ ion beam, the velocity-matched condition yields a value of cooling energy E_{cool} =2.4 eV. While this is an ideal estimate, the energy in realistic conditions is affected by the cathode contact potential, as well as the space charge effects at the CEEB and that of a charged particle beam traversing through space, which contribute to a potential offset. Precise values for these offsets can only be determined experimentally, consequently yielding the required cooling energy conditions for the cooling voltage used to tune the beam at, accounting for the realistic offsets.

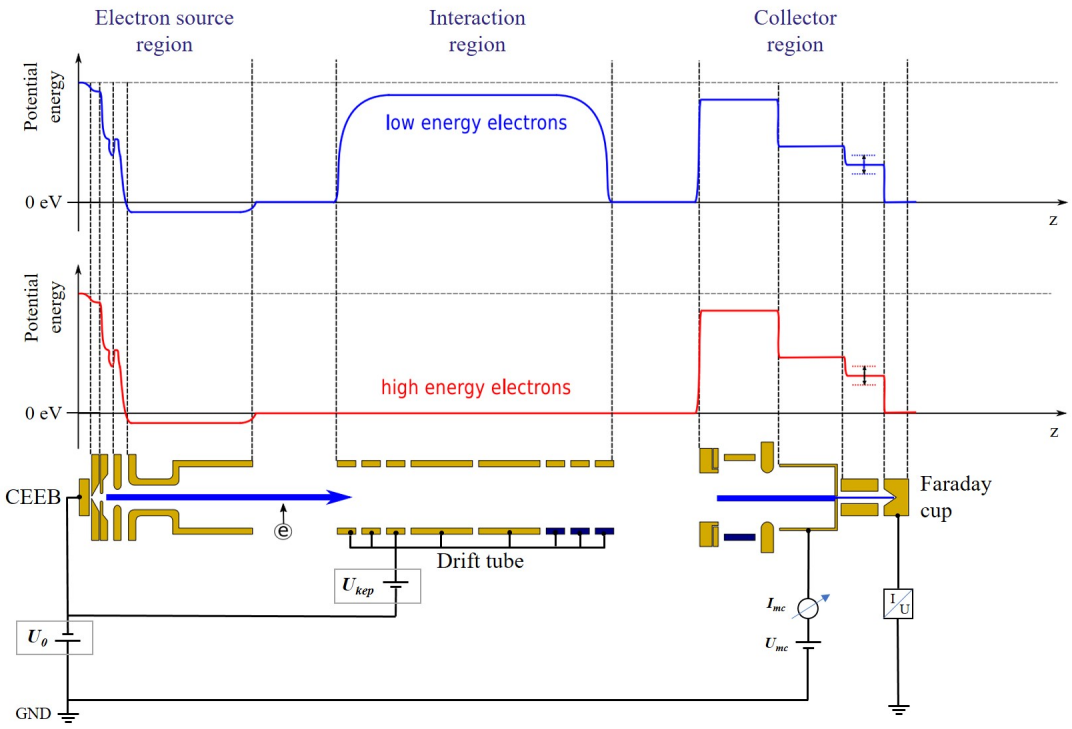

Figure 3.4: Functional schematic of the potential energy landscape of the electron beam as it traverses the eCool setup and the simplified circuit connections used for realisation. The red curve shows the configuration for the standard mode operation wherein the drift-tube electrodes are held at ground (U_{kep} =0, as in figure) and only the (CEEB) cathode-potential defines the lab-frame electron energy. The blue curve exhibits the drift-tube operation mode with electrons produced at high energy and consequently decelerated at the drift tube (U_{kep} $\neq$0) to finally reach the aimed electron-ion interaction energy. Image adapted from the work of M. Rimmler [72].

The principle of electron cooling can be used to accurately detect the velocity-matched condition by searching for the optimum of ion cooling signal with respect to the fine-tuned electron beam energy values. In the cases when the ion current in the ring is considerably high ($\sim$ μA), the most straight-forward method to observe cooling is to tune the spectrum analyser to identify the second harmonic frequency signal (in the Fourier domain) versus power of the current signal (in RF-bunched beam setting) as detected by the current-pickups at the CSR. In case of effective electron cooling, the second harmonic of the revolution frequency of the bunches is expected to peak when compared to the signal without cooling. This is due to the fact that for a bunched-beam only pure sinusoidal time-structure, synchronous with the bunching frequency, is imprinted on the beam; whereas for a cooled beam, the longitudinal extents of the beam-bunches physically shrink due to cooling, thus

contributing to higher harmonics of the bunching frequency in the Fourier domain. A more visual manifestation of this effect can be used as another method wherein bunched current signal from the current pickup can be directly observed on a digital oscilloscope. On averaging the waveforms over $\sim$ms time-scales, the bunches appear like an approximate Gaussian shape. This is expected for an ion beam with a large longitudinal temperature spread. For an optimal cooling condition, this bunch-shape shrinks in width while growing in height simultaneously, which is a relatively direct depiction of shrinking beam size with decreasing energy spreads. It is important to note that the aforementioned methods require RF-bunching of the ion beam to be employed effectively.

A more prudent approach would involve cooling detection on the coasting (DC) beam, which is closer to the realistic conditions as used for recombination measurement. One such method uses the fact that the dissociative recombination (DR) reaction cross-section usually has a maximum at zero collision energy for the electron-ion system. Given this, the electron beam settings can be varied systematically and the recorded neutral fragment count-rate on the NICE detector can be used as a credible measure for the velocity-matched condition. For comparison, a high detuning energy (e.g., $\sim$30 eV in this case) is chosen as a reference at an expected low DR rate condition. Understandably, a good cooling point should exhibit highest ratio between the cooling and reference settings for the measured number of events on the detector. Another method uses the detected signal by the current pickup in a resonant regime, wherein the spectrum analyser is used to represent the ion beam signal intensity in the frequency-space using a time-flow representation. This enables time-evolution observation of the revolution frequency of the ion beam. From the slip-factor η definition as mentioned in eqn. 2.11, we understand that the revolution frequency spread of the beam inside the storage ring is directly related to ion beam momentum spread, which can be used to optimise the ion beam cooling.

Finding the velocity-matched condition for the TiO^+ ion beam was an especially challenging task given the high molecular ion mass, wherein an effective implementation of the electron cooling technique requires highly accurate knowledge of the ion dynamics in the storage ring (see sec. 2.2) and the electron beam overlap with respect to the ion beam, in addition to the accurately tuned electron beam energy. Following the various methods to effectively detect electron cooling, it was difficult to obtain a conclusive proof for the same. Further detailed investigations in the theoretical considerations of the electron cooling technique, along the lines of work by Beutelspacher et al. [73], highlight the crucial role played by the phenomenon of dispersive electron heating in our case. It can be noted that owing to the parabolic velocity profile of the electrons caused by its space charge,

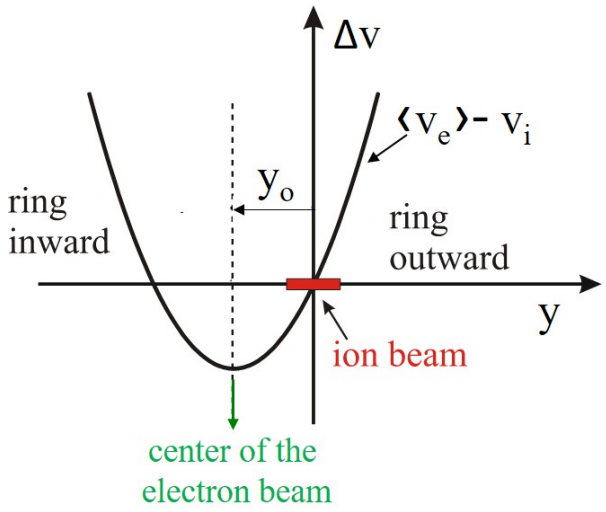

Figure 3.5: Due to the space charge of the electron beam the average electron velocity $\langle v_e \rangle$ increases quadratically with the distance from the electron beam axis. Displacing the electron beam with respect to the ion beam position in the ring leads to interaction with ions having velocity $v_i = \langle v_e(y_0) \rangle$, leading to a dispersive force acting accordingly. Adapted from Beutelspacher et al. [73].

a displacement of the electron beam center with respect to the ion beam gives rise to a heating force [73]. A schematic of the situation has been shown in figure 3.5, wherein the displacement of the electron beam's center with respect to that of the ion beam is given by y_0. Considering the experimental conditions for a mass 64 u, 280 keV TiO^+ ion beam, overlapped with an electron beam density $n_e \sim 5 \times 10^5$ electrons/cm^3 with 2.4 eV mean energy in the lab frame, the dispersion $D_y \sim 2$ m in the CSR standard mode dictates that the ion beam undergoes a dispersive horizontal heating for $y_0 < -1.06$ mm, and dispersive longitudinal heating for $y_0 > 0.53$ mm. This is a consequence of the coupling between the longitudinal and horizontal degrees of freedom introduced due to the particle dynamics in the ring, manifested in the invariant obtained by the sum of the cooling decrements, α_i, in the three directions, i.e.

$$\alpha_x + \alpha_y(y_0) + \alpha_\parallel(y_0) = K \tag{3.3}$$

where, α_i is defined as $-\partial F_i / \partial v_i$, for the electron induced frictional force F_i (see eqn. 2.36) and the ion velocity v_i, in i direction, while K is a constant (refer to [73] for a detailed discussion).

Given the required beam merging accuracy within ∼1.6 mm for the distance between

the center of the electron and ion beams, the experiment presented a formidable situation to deduce the precise velocity-matched conditions using the detection of electron cooling. Hereby, the method of maximizing reaction rates with respect to fine tuning in electron beam energy was used, wherein the detailed investigations led to a convergent value of U_{kep} =5.28 V finally used as the cooling voltage, yielding a velocity-matched condition in accordance with the experimental observables.

3.2.3 Implemented measurement schemes

The planned measurement schemes for the recombination experiment performed as a part of this work, following from the discussion in section 2.7, can be classified in to two categories– rate intensive and imaging intensive measurements. This has been summarised in the table 3.2. With all the data fields recorded for the measurements staying the same (see 4.2), rate intensive measurements were more focused on acquiring the fragmentation data over a broad range of detuning energies, E_{d}, in a determined energy range, traced in the measurement step, for a relatively short time ($\sim$20 ms per meas step in a single cycle) amounting to a total of $\sim$0.5 - 1 second of total measurement time at a specific E_{d} for each run. In contrast, the imaging intensive measurements probed a small set of detuning energies but acquired high statistics for each ($\sim$50 ms per measurement step in a single cycle), typically amounting to $\sim$ 5-40 seconds per E_{d}, per run, given that the number of cycles now span over a smaller set of E_{d}.

Another parameter varied over different runs was the storage time wherein the ions were allowed to circulate in the low-radiation field of the CSR, without electrons for a given time duration, prompting radiative cooling of the molecular ions (see sec. 3.3). This was done for durations of 0 sec, $\sim$500 sec, $\sim$1000 sec and $\sim$1500 sec after injection, wherein ions were stored immaculately in the CSR, following which the electron beam was switched on and DR measurement was performed for the next $\sim$100 seconds – the typical times over which the DR signal submerged within the background on the detector.

3.2.4 Detector settings and physical estimates

Detection of the neutral product fragments resulting from the DR reaction is done using the NICE detector system. As discussed in section 2.6, the detector is a compound setup of MCP followed by a Phosphor-screen and a fast-camera. The former two devices are used in the cryogenic environment, while the fast-camera is kept outside the CSR at room-temperature. The MCP, usually operated at $\sim$1700 V potential difference between the

Type	Energy range probed (E_d)	Storage time (electrons off)
Rate Intensive	-30 meV to +190 meV (32 steps– divided equally in log-scale)	0 sec
		500 sec
		1000 sec
		1500 sec
	10 meV to 38 eV (22 steps– divided equally in log-scale)	0 sec
		500 sec
	15 meV to 70 eV (12 steps– divided equally in log-scale)	0 sec
		500 sec
Imaging Intensive	0 eV	0 sec
	10, 20, 30, 40, 60, 90, 120, 150 meV	500 sec
	60, 90, 120 meV	1000 sec

Table 3.2: Classification table for the data measured and acquired during the measurement campaign for TiO^+. The storage time represents the waiting duration (off-step in the scheme, see sec. 2.7) immediately after the ion beam injection in the CSR (allowing for radiative cooling of the molecule). Following this, electron beam was switched on, and E_{d} values represent the tuned electron-ion collision energies (measurement step in the scheme) probed into for various measurement runs.

front-back surfaces, shows a drastic increase in path resistance with decrease in temperature which is unfavorable for signal pulses generated by the impinged fragments. Thus, the MCP was separately heated during the measurement campaign, realising the operating temperatures close to 40 K. The MCP front was lifted to a potential of $+1100$ V, while the back surface was kept at -678 V, which resulted in an effective resistance of $\sim$385 MΩ. Following this, the Phosphor-screen was kept at $+8000$ V to attract the emergent electron cloud, consequently producing a short-lived bright spot which could be observed by the fast-camera with a 50 mm objective lens. The assembly effectively enables position-sensitive neutral fragment detection at a typical rates from a hundred to few kHz in the experiment, wherein the recorded pixels span approximately 0.4 mm each, a detailed analysis for which has been followed in section 4.1.

Using the discussed detector settings, separation between the product fragments after dissociation, viz. Ti and O, as noted in section 2.6, can expressed by the equation 2.38. In the experiment, fragment separation is manifested as a 2D projection of the distance in transverse plane. Given that the fragment distance information is directly related to the kinetic energy release (KER) of the reaction and thus is one of the fundamentally crucial experimental observables for our case. To better illustrate this behaviour, the table 3.3

E_{d} or E_{KER} [eV]	E_{lab} [eV]	Fragment distance [mm]
0.0	2.400	0.000
0.005	2.625	1.017
0.01	2.721	1.439
0.02	2.859	2.035
0.03	2.967	2.492
0.06	3.220	3.524
0.09	3.420	4.316
0.12	3.594	4.984
0.15	3.751	5.572
0.5	5.092	10.17
1.0	6.499	14.39
5.0	14.33	32.17
10.0	22.20	45.50
30.0	49.37	78.81
70.0	98.33	120.4

Table 3.3: An instructive list of laboratory frame energies of the electrons (E_{lab}, same as the quantity E_{e} in expression 2.29), listed corresponding to the aimed electron-ion collision energies in the center-of-mass frame, E_{d}, calculated for a 280 keV TiO^{+} ion beam. Also listed are corresponding 3D fragment distances (same as the maximum of 2D fragment distance as in equation 4.7 for similar parameters) for representation, calculated according to the expression 2.38 with $D = 3296.7$ mm and E_{KER} taken to be the same as the tabulated collision energy value, E_{d}.

lists energies in the center-of-mass frame of the electron-ion system (E_{d}), and correspondingly tuned lab-frame energy E_{lab} calculated in accordance with eqn. 2.29 with cooling energy, $E_{\mathrm{cool}} = 2.4$ eV. Further, the table also lists the 3D fragment distance (same as the maximum of the 2D distance) for representation, calculated according to the expression 2.38 with $D = 3296.685$ mm and E_{KER} taken to be the same as the listed energy value, E_{d}. Physically this can be interpreted as a simplified case wherein the collision energy is completely manifested as KER of the reaction, analogous to the case with $E_{i,f} = 0$ in the expression 4.6. This is instructive to understand the behaviour of the experimental observables, to finally deduce the energetics of the reaction from a detailed analysis of the same, as discussed further in this work.

3.3 TiO^+ radiative cooling model

The CSR provides a unique possibility of storing the molecular ions in a black-body radiation field of temperature less than 10 K, for time durations on the order of $\sim$1000 seconds. This allows for the infra-red active molecular ions (with finite dipole moment) to de-excite by radiating out the rotational and vibrational energy introduced at production. Consequently, the choice of ion storage times before commencing electron-induced recombination measurements is based on the rovibrational lifetime estimates for the molecule. The underlying rationale is to probe into the reaction with the initial conditions closest to the ground state of the molecular ion in order to understand the rotational-level dependence for recombination, and to minimize the reaction's energy uncertainty introduced by the rotational-level population distributions arising at the ion source (vibrational excitations are extremely short-lived in our case, and contribute negligibly). Further in this section we discuss the vibrational and rotational lifetime estimates for the TiO^+ molecular ion under the storage conditions at the CSR.

To make the first approximations for the calculation of rotational-state lifetimes, we invoke the treatment of Einstein's A-coefficient, A_{fi}, defining spontaneous transition probability between states f and i allowed by the electric dipole selection. In the CGS units, the A-coefficient is given as [74],

$$A_{fi} = \frac{64\pi^4}{3h}\Delta\widetilde{\nu_{fi}}^3\frac{1}{(2J+1)}\mathcal{T}_{fi}\cdot 10^{-36}\cdot F_{hl} \tag{3.4}$$

here, h is the Planck's constant, $\Delta\widetilde{\nu_{fi}}$ is the energy difference between the initial and final states in terms of wavenumbers, $(2J+1)$ accounts for the degeneracy of the state i, $\mathcal{T}_{fi}$ is the transition dipole moment which in this case is $\mu^2_{\mathrm{TiO^+}}$ (where, $\mu_{\mathrm{TiO^+}}$ =6.3) is the electric dipole moment for the TiO^+ [courtesy of N. Shuman, obtained as private communication] molecular ion in Debye (conversion of which to CGS introduces the multiplicative factor), and F_{hl} is the appropriate Hönl-London factor (R_1 for Ω = 3/2 and R_2 for Ω = 5/2) used to define the relative intensity distribution between the rotational levels for a diatomic molecule [75]. In order to calculate the rotational level energy for TiO^+, we use the data from Huang et al. [48], wherein the rotational constants for the two fine-structure states have been calculated to be $B_{3/2} = 0.5613$ cm^{-1} and $B_{5/2} = 0.5715$ cm^{-1}, while the energy difference between the two states due to the spin-orbit coupling is given as Δ = 105.9

Rotational state characteristics Ω = **3/2**						
J_{i}	$E(J_{\mathrm{i}})$ [cm^{-1}]	J_{f}	$E(J_{\mathrm{f}})$ [cm^{-1}]	$\Delta\widetilde{\nu}$ [cm^{-1}]	A_{fi} [s^{-1}]	**t** [s]
2.5	2.8065	1.5	0 (reference)	2.8065	7.34×10^{-5}	1.36×10^{4}
3.5	6.7356	2.5	2.8065	3.9291	2.70×10^{-4}	3.71×10^{3}
4.5	11.787	3.5	6.7356	5.052	6.42×10^{-4}	1.56×10^{3}
5.5	17.962	4.5	11.787	6.174	0.00124	805
6.5	25.259	5.5	17.962	7.297	0.00213	470
7.5	33.678	6.5	25.259	8.420	0.00334	299
8.5	43.220	7.5	33.678	9.542	0.00495	202
9.5	53.885	8.5	43.220	10.665	0.00699	143
10.5	65.672	9.5	53.885	11.787	0.00953	105
11.5	78.582	10.5	65.672	12.910	0.01262	793
12.5	92.615	11.5	78.582	14.033	0.01630	614
13.5	107.77	12.5	92.615	15.16	0.02063	485
14.5	124.05	13.5	107.77	16.28	0.02567	390
15.5	141.45	14.5	124.05	17.40	0.03147	318

Table 3.4: Calculated estimates for the rotational level characteristics of TiO^{+} molecular ion, for Ω = 3/2 fine-structure level. The addition of rotational quanta increases J by 1 and the level energy is estimated using eqn. 3.5. The energy difference $\Delta\widetilde{\nu}$ $(E(J_i) - E(J_f))$ is used for calculation of Einstein's A-coefficient, A_{fi} according to expression 3.4. The reciprocal of A-coefficient yields the lifetime estimate $\boldsymbol{t}$ of the rotational level.

cm^{-1}. Using this, the rotational level energy, E_J, can be calculated as follows

$$E_J = \Delta + B(J(J+1)) \tag{3.5}$$

where, J denotes the rotational level number. This treatment can be used to estimate the rotational state lifetimes and a list for the first few levels has been produced in tables 3.4 and 3.5 for Ω = 3/2 and Ω = 5/2 respectively.

It is important to note that up till now we have not considered the inter-combination lines, i.e. the transitions between fine-structure states, Ω = 3/2 and Ω = 5/2. We account for this in the elaborate radiative cooling model, wherein we also consider the radiation field inside the CSR of $\sim$6 K causing stimulated transitions in addition to the spontaneous

Rotational state characteristics $\boldsymbol{\Omega}$ = **5/2**						
$\boldsymbol{J}_{\mathrm{i}}$	$\boldsymbol{E}(\boldsymbol{J}_{\mathrm{i}})$ [cm^{-1}]	$\boldsymbol{J}_{\mathrm{f}}$	$\boldsymbol{E}(\boldsymbol{J}_{\mathrm{f}})$ [cm^{-1}]	$\boldsymbol{\Delta\widetilde{\nu}}$ [cm^{-1}]	$\boldsymbol{A}_{\boldsymbol{fi}}$ [s^{-1}]	**t** [s]
3.5	4.0005	2.5	0 (reference)	4.0005	1.7077×10^{-4}	5.85×10^{3}
4.5	9.144	3.5	4.0005	5.144	5.2696×10^{-4}	1.89×10^{3}
5.5	15.431	4.5	9.144	6.287	0.00112	889.2
6.5	22.86	5.5	15.431	7.430	0.00202	495.2
7.5	31.433	6.5	22.860	8.573	0.00327	306.1
8.5	41.148	7.5	31.433	9.716	0.00492	203.1
9.5	52.007	8.5	41.148	10.859	0.00705	141.9
10.5	64.008	9.5	52.007	12.002	0.00969	103.2
11.5	77.153	10.5	64.008	13.145	0.01291	77.49
12.5	91.440	11.5	77.153	14.288	0.01676	59.68
13.5	106.87	12.5	91.440	15.43	0.02129	46.96
14.5	123.44	13.5	106.87	16.57	0.02657	37.63
15.5	141.16	14.5	123.44	17.72	0.03266	30.62

Table 3.5: Calculated estimates for the rotational level characteristics of TiO^{+} molecular ion, for $\Omega = 5/2$ fine-structure level.

transitions as discussed previously. This demands the use of detailed balance, considering both, the Einstein's A- and B-coefficients, with the appropriate accounting for relative level intensities using Hönl-London factors. The ions are considered to be produced as a Boltzmann distribution, in equilibrium with the Penning source temperature of $\sim$1100 K, and with an equal probability to occur in any of the two Ω states. This initial population distribution is then allowed to evolve according to the aforementioned processes and considerations, effectively yielding a set of first-order differential equations which can be solved numerically to deduce the rotational level population distribution after a storage time $\boldsymbol{t}$ inside the CSR. The results from this radiative cooling model of the TiO^+ molecular ion, averaged for storage time intervals of 0-100 sec, 500-600 sec, 1000-1100 sec and 1500-1600 sec have been produced in the figure 3.6. It can be noted that the initial rotational population distribution is extremely broad (see the 0-100 sec panel in fig. 3.6), spanning upto rotational levels with energies $\sim$500 meV. This distribution slowly cools down by emission of photons, on time-scales statistically given as the lifetimes (see table 3.4, 3.5), typically on the order of μs or ms for states with $J > 40$, sequentially falling down the rotational level ladder. As the inter-combination transitions are allowed, the ion population also converges closer to the $\Omega = 3/2$ ground level with passing time, and the rotational bunch spread (number of excited levels) decreases. However, due to proximate energy-levels at low rotational excitations the states have successively longer lifetimes, not allowing the relaxation to the lowest states for even up to 1500 seconds of ion storage. These estimates have been used to pragmatically choose the appropriate storage time intervals for measurement schemes (see 3.2), and the models have further been used in the endothermicity analysis (see chapter 5).

Further for the purpose of completeness, the vibrational state characteristics for TiO^+ system have been estimated. This is implemented using a similar treatment as for the rotational state characteristics, to calculate the vibrational lifetimes wherein we invoke the Einstein's A-coefficient (formulated in eqn. 3.4) and modify it to use for evolution of molecular vibrational state populations. Here we make reasonable assumptions to calculate the results in first approximation, such as– assuming J-independence for the different v states, level separation within harmonic approximation yielding the vibrational level spacing as $\Delta\widetilde{\nu_0} = 1056.1$ cm^{-1} (refer to calculations by Huang et al. [48]), and the dipole moment gradient along the internuclear axis given by $\mathrm{d}\mu/\mathrm{d}r = 6.2 \times 10^8$ D/cm for TiO^+ [calculations courtesy of N. Shuman; obtained as private communication], using which we can obtain the dipole transition matrix element as in 3.4 for vibrational transitions, $\mathcal{T}_{\mathrm{vib}}$

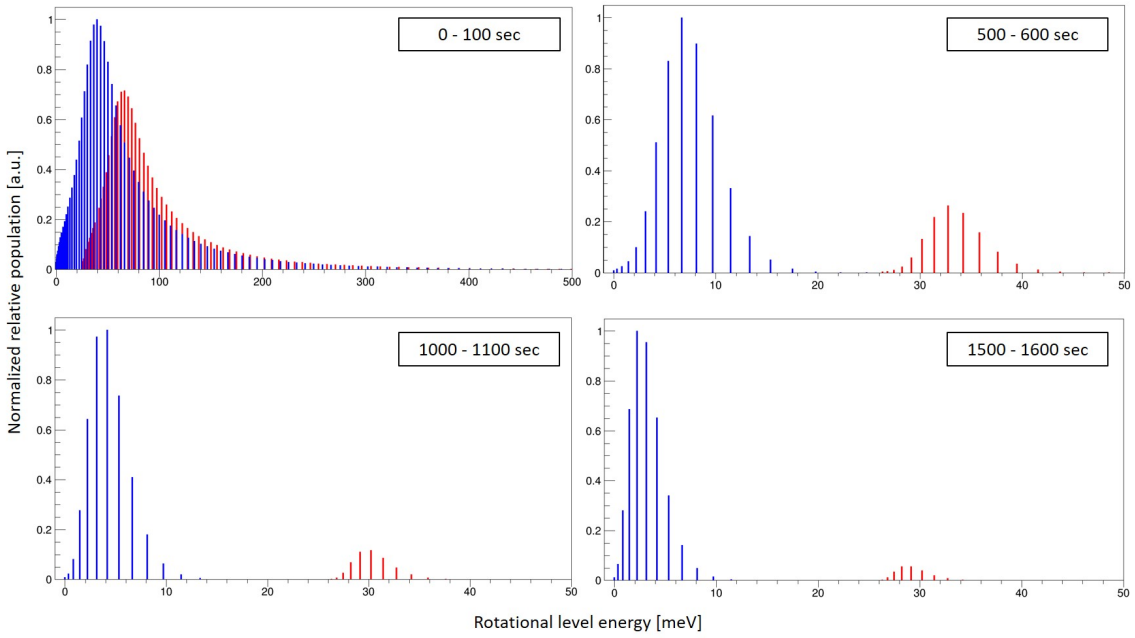

Figure 3.6: The results obtained from the radiative cooling modelling for TiO^+ in the CSR environment, considering the dipole moment $\mu_{TiO^+} = 6.3$ D for molecular ion, and the initial source temperature of 1100 K. The plot shows populations for both $\Omega = 3/2$ (in blue) and $\Omega = 5/2$ (in red) fine-structure levels, wherein each line represents a rotational level. The plotted populations are results from cumulation over the indicated time intervals, wherein the population fraction of the highest populated rotational level is used to normalise the distribution, thus finally representing the relative normalised population fractions. Note the different X-axis range for the population distribution curve for 0-100 second interval.

as [76],

$$\mathcal{T}_{\text{vib}} = \frac{h(v+1)}{8\pi^2\, m_{\text{red}}\, \nu_0} \left|\frac{\mathrm{d}\mu}{\mathrm{d}r}\right|^2 \tag{3.6}$$

where, ν_0 is simply the level energy separation in terms of frequency calculated as $\Delta\widetilde{\nu_0} \cdot c$. The obtained results for first few vibrational states have been listed in the table 3.6. It can be noted that the highest sustaining lifetimes, i.e. for the transition from $v = 1$ to $v = 0$ is ~ 53 ms, with an energy spacing between levels of ~ 131 meV– a consequence of the characteristic high dipole moment of the TiO^+ molecular ion. Thus, the vibrational excitations of the ion can be safely assumed to be quenched within the first few seconds after ion beam injection in the CSR.

Vibrational state characteristics				
v_{i}	v_{f}	$E(v_{\mathrm{i}})$ [cm^{-1}]	A_{fi} [s^{-1}]	**t** [s]
1	0	0 (reference)	18.899	0.0529
2	1	1056.1	37.797	0.0265
3	2	2112.2	56.696	0.0176
4	3	3168.3	75.595	0.0132
5	4	4224.4	94.494	0.0106
6	5	5280.5	113.39	0.0088
7	6	6336.6	132.29	0.0076
8	7	7392.7	151.19	0.0066
9	8	8448.8	170.09	0.0059
10	9	9504.9	188.99	0.0053
11	10	10561.0	207.89	0.0048

Table 3.6: Calculated results for vibrational level characteristics of TiO^+ molecular ion. We consider J-independent behaviour for vibrational excitations in the ion, and calculate the Einstein's A-coefficient according to eqn. 3.4, wherein the transition matrix element for vibrational level transitions, $\mathcal{T}_{\mathrm{vib}}$, is given by the expression 3.6. It can be noted that the highest sustaining lifetimes, i.e. for the transition from v =1 to v =0 is $\sim$ 53 ms, with an energy spacing between levels of $\sim$ 131 meV, a consequence of the characteristic high dipole moment of the molecular ion.

Chapter 4

Fragment Imaging Data Processing and Modeling

The course of this chapter traces through the progression from the experimental techniques to their manifestation in the consistency of the acquired data. Following the structure of the acquired data, section 4.1 describes the procedure used to calibrate and appropriately transform the recorded data by the NICE imaging detector into the physical units. Section 4.2 elucidates the process of using this calibration to plot the measured data as 2D fragment distance versus event count/intensity. In progression, section 4.3 describes the Monte-Carlo modelling required for the interpretation of the recorded fragment distribution data, and gives an insight into the physical behaviour of the measurands, instrumental to draw conclusions for the measurement objective in chapter 5.

4.1 Pixel-to-mm calibration

Imaging measurements are recorded with the aid of a position-sensitive detector, coupled with a phosphor-screen and camera setup. Once the planned measurements are performed and the data recorded, what follows foremost is the proper calibration of the same before the analysis and interpretation. The recorded data, as is extracted from the camera frames, is based in a 2D pixel-space. Thus, as a first step to understand the data, it is imperative to transform this to the appropriate 2D physical space, i.e. mm-scale on the detector plane in our case.

The idea involves a calibration mask, essentially a hole grid with precisely calibrated distances. The mask, effectively, is a movable flap on the NICE detector designed such that it can be moved in or out of the ion beam's path to the detector surface. This movement is about a horizontal axis parallel to the detector plane passing from above the MCP. Once

in place, the mask serves as a filter, allowing the ions to pass only through the grid-holes. Given that the distance between the holes in each direction is precisely 10 mm (except for three outliers from the pattern, essential in determining the orientation of the imaging camera with respect to the grid), an identical behaviour is expected from the measured data on the detector. Thus, ideally the pixel-to-mm calibration procedure defines the conversion of the recorded pixel-coordinates in the image by the camera, to the precise spot positions as on the mask. This takes into account the physical effects which may be introduced due to an infinitesimal angular tilt of the camera with respect to the calibration mask plane, or image distortion due to the finite size of the object, lens aperture, reflective elements used for directing the light path, and due to the object-camera distance being comparable to the lens' focal length. Given the percipient design of the system, individual contributions from these effects are small, which can be cumulated together and accounted for using an appropriate fitting function for the camera-to-mask transformed coordinates $\mathrm{X_{msk}}$ and $\mathrm{Y_{msk}}$:

$$\begin{aligned} X_{msk} &= f_x(x_{px}, y_{px}), \\ Y_{msk} &= f_y(x_{px}, y_{px}) \end{aligned} \tag{4.1}$$

The transformation (fitting) functions f_x and f_y take the pixel-space coordinates x_{px} and y_{px} as the arguments. For the current work, we consider three kinds of fitting functions: 1) The **linear 1D fit**, which only takes a single argument and fits according to $\mathrm{X_{msk}}$= a + bx_{px} (analogous for $\mathrm{Y_{msk}}$) dependence. This model only performs a scaling, including an offset, but disregards any transversal correlation. 2) The **linear 2D fit** uses a $\mathrm{X_{msk}}$= a + bx_{px} + cy_{px} (analogous for $\mathrm{Y_{msk}}$) functional relation. This systematically accounts for longitudinal scaling, a constant offset, along with X-Y correlation. One of the ways this interdependence may be introduced is by camera's rotational tilting with respect to the assumed axes-orientation in the calibration mask plane, among other cases. 3) The **elaborate 2D fit** case uses a $\mathrm{X_{msk}}$= a + bx_{px} + cx_{px}^2 + dy_{px} + $ex_{px}y_{px}$ (analogous for $\mathrm{Y_{msk}}$) relation. Compounding on the linear 2D fit, this further introduces quadratic correction along the primary axis, as well as in form of a correlation. However, it is to be noted that according to the defined precision of the detector setup these corrections risk posing as a mathematical overdefinition.

Taking in view the physical conditions, the data is measured and recorded, as on the detector, placed between the calibration mask and the camera. While the detector does not limit the resolution of the camera, given the construction and moving mechanism of

the calibration mask, an off-parallel alignment (assume, by an angle α) of the mask with respect to the detector may result in an additional distortion. If the realistic transformed coordinates in the detector plane are denoted as $\mathrm{X_m}$ and $\mathrm{Y_m}$, in case of an α tilt, this would give:

$$\begin{aligned} X_m &= X_{msk} = f_x(x_{px}, y_{px}), \\ Y_m &= Y_{msk}.\cos(\alpha) = f_y(x_{px}, y_{px}).\cos(\alpha) \end{aligned} \tag{4.2}$$

It is important to note that the pixel-to-mm calibration procedure, as mentioned before, is expected to return radially symmetric solutions in an ideal case. However, in the physical picture, it becomes apparent that the X_{m}-Y_{m} correlations tend to make the deductions unsymmetrical in the transverse directions. This can be observed by using the goodness of fitting and the residuals from the fitted parameters. The effects propagated due to the introduction of detector in the model, including the angular tilt of the calibration-mask can be independently observed by using the projection of the circular detector aperture, which is independent of α, as has been discussed later in the section. This can be accordingly corrected for, and the final parameters for the pixel-to-mm calibration deduced. The systematic procedure for the same has been elucidated below.

4.1.1 Determining measured-spot positions

Calibration procedure involves a first measurement with the calibration mask placed in front of the NICE detector. Through the measurement the detector only sees the impression of the ion beam (reacting with the residual gas and producing neutral products) passing through the mask in place. The measured plot is produced in figure 4.1. The measurement essentially provides sample points (seen as dense 'spots' in the figure), spaced precisely on the mask grid, projections of which are obtained in the recorded data in the pixel-space coordinates. The other data-points visible as randomly distributed uniformly over the detector area are a result of cosmic-ray induced signals, and dark counts, recorded by the detector over the acquisition time.

While these spots are of finite size, it is important to find a center for each to precisely determine the positions with single pixel accuracy. To deduce these center coordinates for each spot, termed as the 'calibration points', the recorded event plot is used. Each dense spot appearing on the plot is selected using a customised algorithm which scans over the complete data and picks out the appropriate points with high density within a pragmatically specified box span defined in pixels, thus selecting the relevant spots. In our

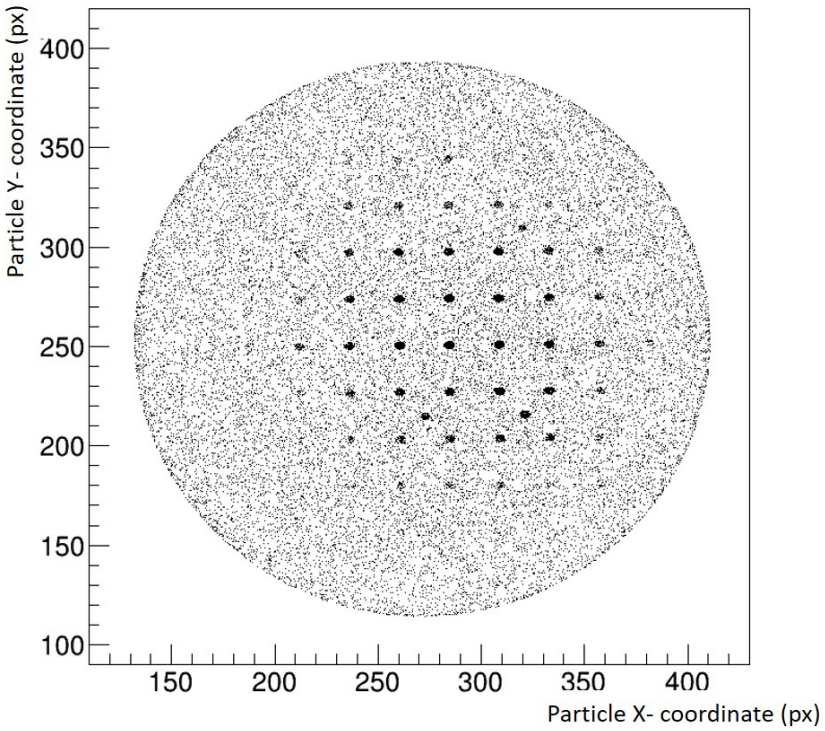

Figure 4.1: Plot for the recorded events on the NICE detector with the calibration mask placed in front of it. On the calibration mask, each 'spot' is precisely separated by 10 mm, except for three outliers from the pattern, essential to determine the orientation of the imaging camera with respect to the calibration grid.

case, we obtain a total of 28 spots with statistically significant event density to use for the calibration procedure. To pin down the calibration point positions for each of the spots, we consider the same box-span for the X and Y spread for each spot independently, and use the event density projections along both axes. Along each axis, this projection is fitted by a Gaussian function. The centre point of the fitted Gaussian obtained in this way is taken as the calibration point, along with the error for the same. The calibration point positions obtained in this way has been produced in the figure 4.2 as cross marks.

4.1.2 Transformation functions

Once the calibration points are obtained, these pixel coordinates can be compared with their corresponding mask hole positions to obtain the calibration mask-camera transformation functions $f_x(x_{\rm px}, y_{\rm px})$ and $f_y(x_{\rm px}, y_{\rm px})$. Ideally (as on the mask) these points are separated by (10 mm, 10 mm). There are three special points present, one in the upper right quadrant, and one each in the lower two quadrants, which aid in fixing the mask and camera's relative

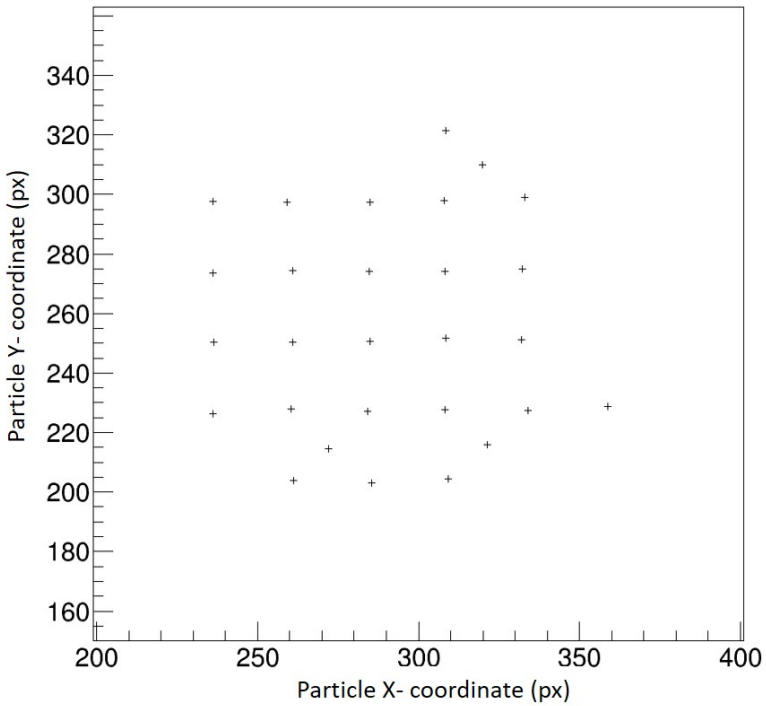

Figure 4.2: The *calibration points* obtained as a result of using the identified spots by the algorithm, projecting the event densities of each spot along both axes as histograms, and fitting the binned histograms with Gaussian functions to find the center position.

orientation. For uniformity with previous works, we assign the upper right special point as the absolute position (25mm, 25mm), and use this as a reference to assign all other positions when needed. Once this is done, we have a sorted list of calibration points as seen using on the detector. This data can now be used to fit the pixel-coordinates to mm-positions through various functional dependencies as mentioned before.

The 1D linear fit (of the kind, $a + bx$), produced in the figure 4.3 takes into account a constant axis scaling and an offset, while assumes no interdependence between transverse axes coordinates. As can be observed from the plot, the obtained pixel coordinates (x_{px} and y_{px}) plotted along the X-axis fit fairly well with the mask hole coordinates in mm, plotted along the Y-axis. The residuals from the plot are used as quality parameters. In this case it can be noted that the residuals record as high as 0.4 mm deviation from the measured and transformed data. The second fit, termed as the 2D linear fit (of the kind, $a + bx + cy$) in figure 4.4, that accounts for transversal coordinate dependence on a linear scale, along with the scaling and offset, fits a plane to the distribution in each case separately for $\mathrm{X}_{\mathrm{msk}}$ and $\mathrm{Y}_{\mathrm{msk}}$. Noteworthy is that the residuals have mostly shrunken within 0.26 mm maximum

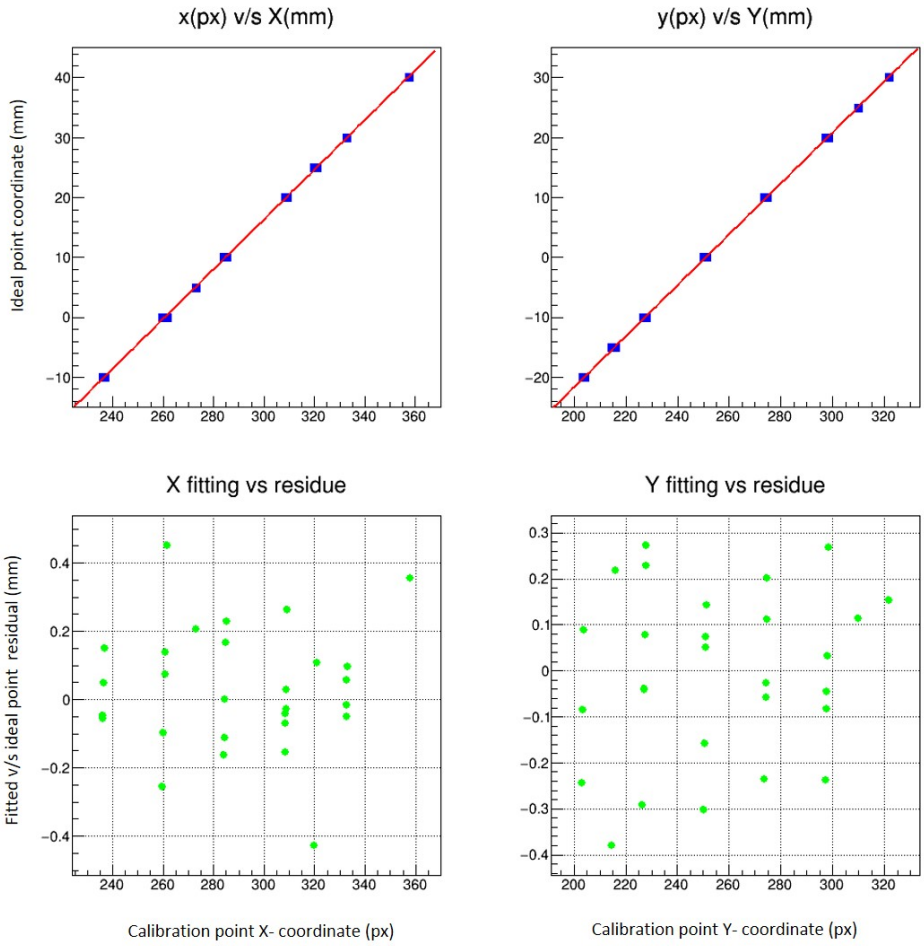

Figure 4.3: 1D linear type does a (first degree polynomial, $ax + b$) fit ($x_{\mathrm{px}}[y_{\mathrm{px}}]$ versus $\mathrm{X_{msk}}[\mathrm{Y_{msk}}]$ plot)– this takes into account the constant scaling and an offset. This also assumes no correlation between transverse axes coordinates. The top curves show the fitting as compared with the pixel coordinates along each axis. The lower curves show the residuals from the fitted curve.

deviation from the actual hole positions. The 2D elaborate fit ($a + bx + cx^2 + dy + exy$ type) that further considers second-order corrections in the coordinate space along with the X-Y linear correlations, scaling and offsets has been produced in fig. 4.5. The residuals in this case lie mostly within 0.2 mm maximum deviation.

It is to be noted that each of the fitting methods have two consistently related parameters– the principal scaling and offset. The principal scaling parameter gives the mm-per-pixel measure, which is the crucial quantity in our analysis and subject to comparison for different methods. The offset parameter is just the first order displacement for the absolute scales, which may be arbitrary by design. The fitting parameters obtained using the men-

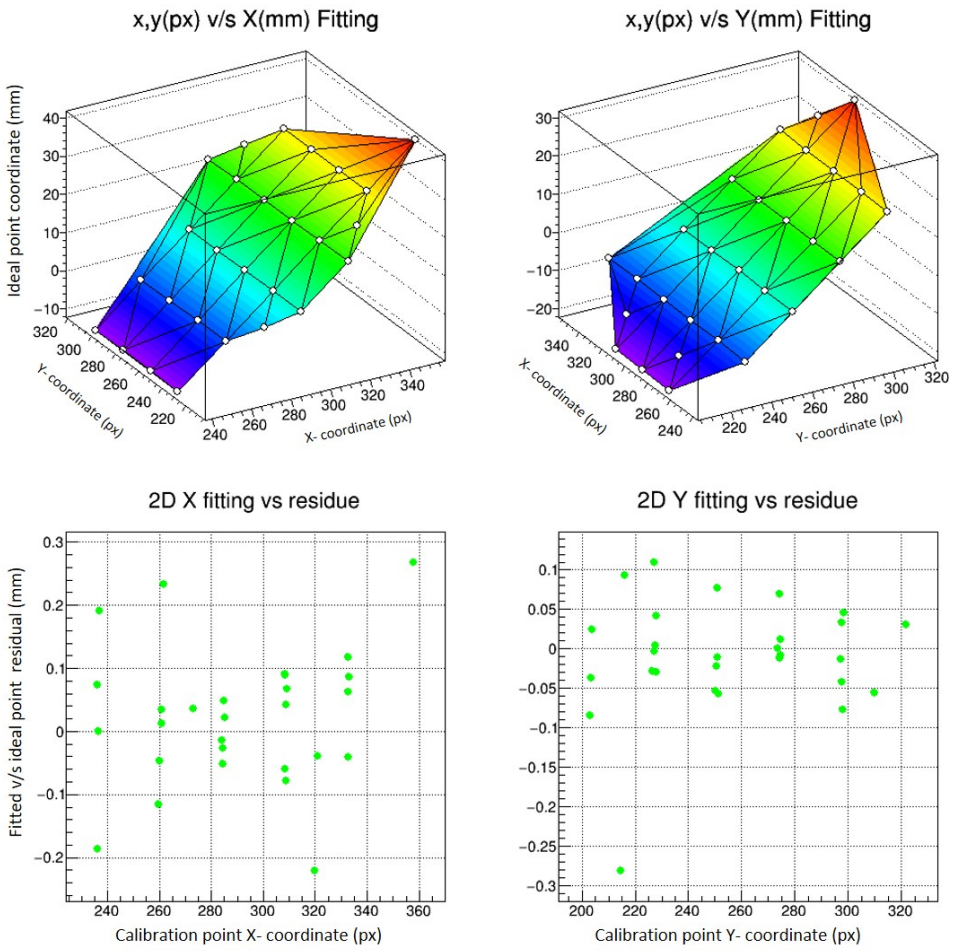

Figure 4.4: 2D linear a mixed linear fit ($ax_{\mathrm{px}}[y_{\mathrm{px}}] + by_{\mathrm{px}}[x_{\mathrm{px}}] + c$ versus $\mathrm{X_{msk}}[\mathrm{Y_{msk}}]$ plot) – assumes transversal coordinate dependence on a linear scale, accounting for the mask's rotation with respect to the assumed X and Y directions, along with the scaling and offset. This also assumes linear correlation between transverse axes coordinates. The top curves show the fitting while the lower curves show the residuals from the fitted curve.

tioned methods have been tabulated in 4.1. It can be observed from the table that the deduced principal parameters along the respective directions are close for the linear 2D and elaborate 2D fitting methods, along with the residuals being less scattered as compared to the linear 1D fit. Further on, we understand that while the elaborate fit does not improve the value (as compared with linear 2D fit) better than 10^{-3}, but the method places mathematical constraints which are not physically relevant for the detector system in consideration. Thus, we use the linear 2D fitting routine in the further steps of the analysis.

To logically follow up the consistency of the calibration procedure, given the cylindrical symmetry of the setting, it is sensible to expect a result reflecting the same property. How-

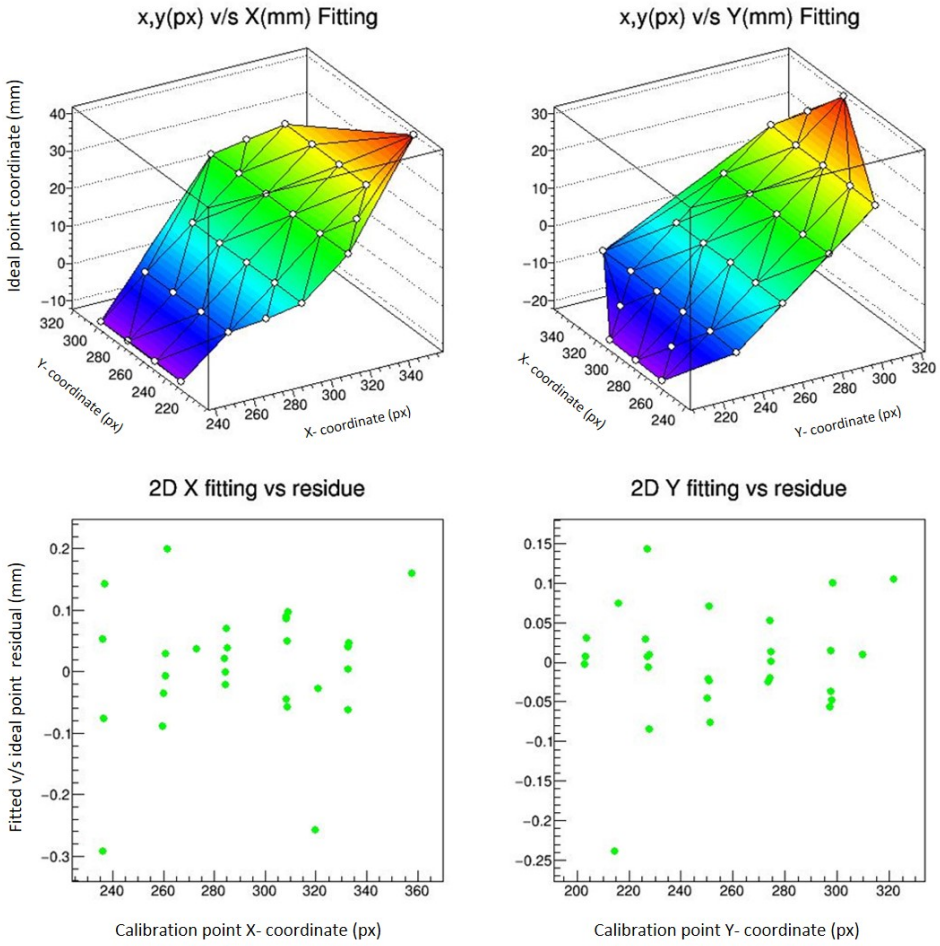

Figure 4.5: 2D elaborate has a higher order mixed polynomial fit ($a + bx_{\mathrm{px}}[y_{\mathrm{px}}] + cx_{\mathrm{px}}[y_{\mathrm{px}}]^2 + dy_{\mathrm{px}}[x_{\mathrm{px}}] + ex_{\mathrm{px}}y_{\mathrm{px}}$ (pixels) versus $\mathrm{X_{msk}[Y_{msk}]}$) accounting for even higher order corrections but physically less relevant given the apparatus constraints. The top curves show the fitting as compared with the pixel coordinates along each axis. The lower curves show the residuals from the fitted curve.

ever, it is noteworthy that the results at this stage (the principal scaling parameters obtained through the linear 2D fitting procedure) in the respective transverse directions do not agree within the error bars. To understand this effect, we transform the pixel-space histogram (see figure 4.1) to mm-space according to the parameters listed in the table 4.1 for linear 2D fit. This has been presented in the figure 4.6 on the left. It can be observed that the regenerated histogram structure departs from an otherwise expected circular projection of the detector aperture (circular with radius as 60 mm), shown in red. This indicates the need for correction due to the physical effects introduced by the presence of the detector between the calibration mask and camera's path. The calibration mask's off-parallel alignment with

Method used	[0]	[1] (principal scaling)	[2]	[3]	[4]	Fitted parameter
Linear 1D fit	-108.18 ±0.03	0.4152 ±0.0001	X_{mc} ([0] + [1] x_{px})			
	-106.79 ±0.03	0.4258 ±0.0001	Y_{mc} ([0] + [1] y_{px})			
Linear 2D fit	-109.26 ±0.04	0.4156 ±0.0001	0.0038 ±0.0001	X_{mc} ([0] + [1] x_{px} + [2] y_{px})		
	-105.31 ±0.04	0.4253 ±0.0001	-0.0046 ±0.0001	Y_{mc} ([0] + [1] y_{px} + [2] x_{px})		
X_{mm} = [0] + [1] x_{px} + [2] x_{px}^2 + [3] y_{px} + [4] x_{px} y_{px} ; Y_{mm} = [0] + [1] y_{px} + [2] y_{px}^2 + [3] y_{px} + [4] x_{px} y_{px}						
Elaborate 2D fit	-113.82 ±0.45	0.4418 ±0.0024	-3.6078e-5 ±3.433e-6	0.0100 ±0.0011	-2.1017e-5 ±3.913e-6	X_{mc}
	-102.29 ±0.38	0.4100 ±0.0021	1.4276e-5 ±3.468e-6	-0.0117 ±0.0010	2.7164e-5 ±3.919e-6	Y_{mc}

Table 4.1: The fitting parameters and error bars deduced using the fitting routines as explained in the section 4.1. The functions used to fit are presented in the table, while the parameters are listed corresponding to each fitting function (method) used.

the detector surface due to imperfect mechanical movement at the flap's end-points can cause this effect. This prompts the use of equation 4.2, correcting for an angular tilt α.

The physical understanding suggests that a relative angle α between the mask and detector plane could create an effective Y-projection of the calibration spots on the detector scaled by $\cos\alpha$ as compared to the ideal positioning with the detector parallely in place. This has been modelled and implemented in the fitting algorithm by assuming an explicit tilt-angle (α) value for equation 4.2, running the fitting according to the linear 2D fitting method and obtaining the parameters for each angle, thus yielding a_α, b_α and c_α. With these parameters, a pixel-to-mm transformation is carried out for the raw plot. Following this, a circular shape is iteratively fitted (with centre and radius as free variables) around the regenerated distribution until all the data points lie inside the model circle. To quantify the goodness of such a fit, the distance of the recorded data points (in mm-space) lying closest to the distribution edge as a function of the angle ϕ (ranging from 0-360°) within a 10° bin about the circle, is used as a measure. This has been produced in the figure 4.7 which shows the smallest recorded distance from the center of the filled data bin closest to the model circle's edge. To understand the trends, it is instructive to note that there are two separate asymmetries expected to play a role in the distance distribution– first, the inherent P-screen asymmetry which is completely random, dependent on subtle manufacturing artifacts; second, the effect due to the relative mask-detector plane tilt that we aim to correct

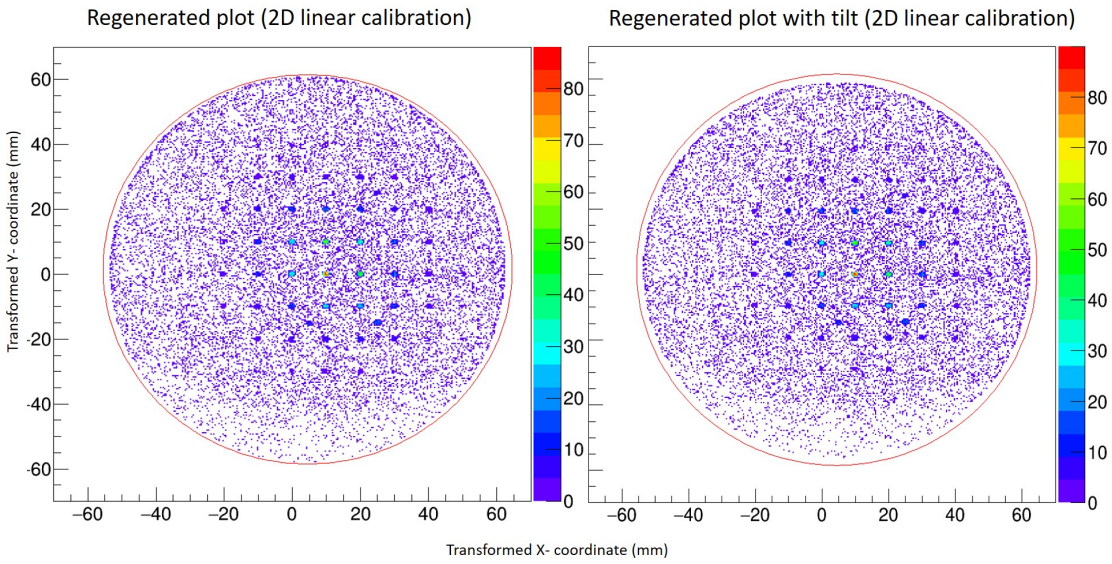

Figure 4.6: The transformed original (see fig 4.1) histogram in mm-space using the calibration parameters deduced using linear 2D fit method. X and Y axes are in mm, while the count intensity in each bin is shown on colour scale. The outer red circle is representative of the detector aperture projection, circular in shape with 60 mm radius. The regenerated histogram for X_{msk} and Y_{msk} can be seen considerably deviating from the expected circular projection in the left figure. The right figure shows X_m and Y_m plot, i.e. including the tilt by angle α correction, generated using the final parameters as in equation 4.3.

for. The procedure is carried out iteratively for different angles α, wherein it is possible to understand the interplay of two aforementioned effects, noting:

- The oscillatory behaviour of the smallest distance of a data-point from the model circle, depicts the ellipticity of the generated distribution for the chosen α. This implies a maxima or minima behaviour occurring at ϕ =90°/270° angle pair or at ϕ =180°/360° similarly define the two extremes of conditions that may occur.

- Given the oscillatory behaviour, the pattern is expected to be symmetric close to the mentioned angle pairs. This can be used to isolate the screen asymmetry effect, which is expected to be random, and thus should achieve a maximum amplitude around a given ϕ angle.

Considering these remarks, it can be observed that the fit shows a converging trend, expectedly, for small angles, viz. α= 13° and α= 16°, while the distance plots for α = 10° and 18° seem to converge towards the two extremes, as shown in figure 4.7. These investigations lead to the result by optimising on aforementioned considerations, yielding α= 14.5°,

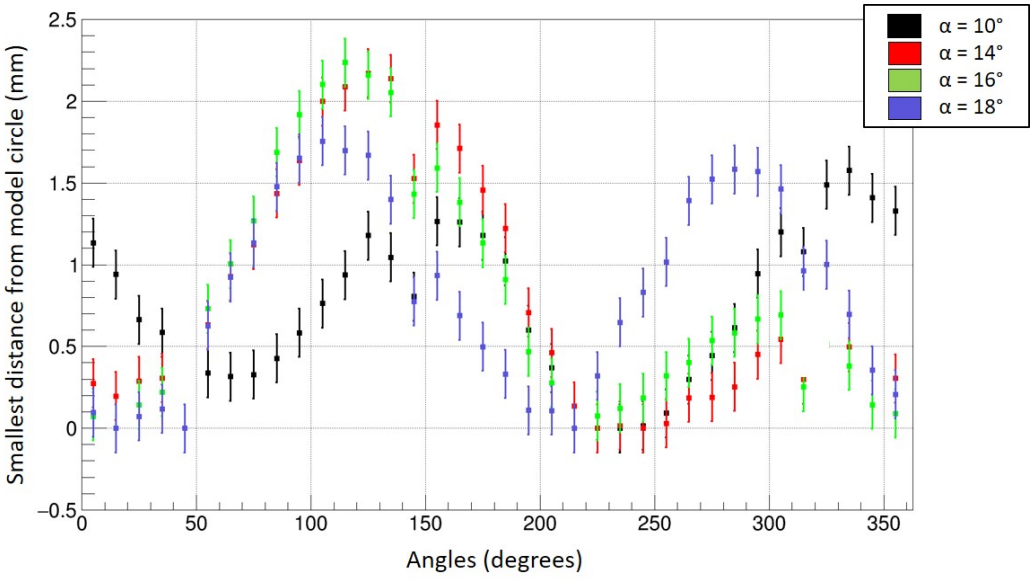

Figure 4.7: The depiction of the smallest distance from a recorded data bin center closest to the modelled circle, used as a quality measure used to determine the tilt-angle α for finding the $\mathrm{X_m}$ and $\mathrm{Y_m}$.

which is our choice for the further analysis. The regenerated curve for $\mathrm{X_m}$ and $\mathrm{Y_m}$ with the α= 14° has been produced in the figure 4.6 on the right.

It is to be noted that the determined tilt angle of 14.5° results in a mm-space transformation of recorded data that spans noticeably smaller than the detector's true circular projection, as shown in figure 4.6. This can be justified by the presence of an aperture in NICE setup covering the outer edges of the detector's sensitive area, as mentioned in A. Becker's work [65].

Finally, to generate the final fitting parameters, the 2D linear fitting is used for finding the $\mathrm{X_m}$ and $\mathrm{Y_m}$ transformation functions correctly. The fitting parameters ultimately deduced from the procedure have been listed below:

$$\begin{aligned} X_\mathrm{m} &= -109.26\,(\pm 0.004) + 0.4156\,(\pm 0.0001)\,\boldsymbol{x_{px}} + 0.0038\,(\pm 0.0001)\,\boldsymbol{y_{px}} \\ Y_\mathrm{m} &= -101.95\,(\pm 0.004) + 0.4117\,(\pm 0.0001)\,\boldsymbol{y_{px}} - 0.0045\,(\pm 0.0001)\,\boldsymbol{x_{px}} \end{aligned} \tag{4.3}$$

The results suggest that each pixel has a physical expanse of ∼0.413 mm, which can further be seen in conjunction with the online data acquisition and compression algorithm, leading to sub-pixel resolutions extending upto ∼0.1 mm resolution for fragment distances on the NICE detector. These values form the basis of the next section and the fragment distance interpretations in the further analysis.

4.2 Imaging data

The data acquisition system at the CSR has been optimised for recording the data in structures efficient for sorting, as well as storing. The recorded data from each subsystem can be compiled together for each run using a script developed by the group to generate ROOT data-analysis framework based file, which is then conveniently customisable, and can be manipulated to extract the relevant data through cuts and filters on various dimensions of the recorded physical quantities. A simplified list of recorded variables relevant for this analysis has been produced in table 4.2.

Once the pixel-to-mm calibration is in place, it is possible to plot and visualise the recorded data from the measurements. As elucidated by the table 4.2, the data recorded for the TiO^+ system is multi-dimensional– available for different times, and measurement energies. However, to study the energetics of the reaction, the recorded data from the imaging intensive runs can be visualised as 2D fragment distance distributions (see eqn. 4.7), i.e. the transverse distance between the dissociated fragments as observed on the detector. These distance distributions give an intuitive and rather straightforward picture of the energetics in the experiment, which is manifested in form of internal excitations or kinetic energies of the fragments. As a first step to understanding the complete dynamics of the process, thus, the understanding of fragment distance distribution plots play a central role. It is important to note here, as was deduced using the pixel-to-mm calibration, the fragment distance uncertainty resolution for the imaging system is 0.1 mm, thus defining the distance histogram binning limit as 0.1 mm per bin. Further on, the absolute resolution to determine impinged fragment position on the detector is limited by the fast-camera resolution, combined with the finite spot-width (in pixel-space) of the electron cloud impinged on the phosphor-screen in the NICE detector assembly (see sec. 2.6). The conservative estimate for this limit according to our investigations is $\sim$1.5 mm – transverse distances between fragments lower than this value are not resolved credibly and thus, the recorded data shows a zero towards the very low distances ($\sim 0.0-0.8$ mm) and then a sharply rising feature between ($\sim 0.8 - 1.5$ mm) which is an accumulation of some of the low-distance events, and has been discussed further in section 4.2.1.

The plotting routine takes into account the processed data files with the pixel variables transformed accordingly to mm space, along with the data filters defining the target quantity and the regime that the data is to be plotted for. For instance, we consider here the data recorded for condition when an ion beam is first stored in the CSR without electrons for $\sim$500 seconds, followed by the electron beam switched on, and the data recorded for ion-

Recorded data structure		
Quantity/Variable	Stored data type	Comments
Injection	Integer number	The number of ion beam injection in the CSR, within a given run.
Scheme	Integer number	The predefined measurement routine identification.
Type	Integer number	Uniquely defines each kind of step possible in a measurement for electron energy (thus Ecm), i.e. cooling, measurement, reference, or electron beam off.
Step	Integer number	Labels each step type sequentially within a routine defined by the scheme to separate same 'type' within a scheme.
Cycle	Integer number	Repetition number of each schemed measurement routine within a given injection.
Number of fragments (in a given event frame)	Integer number	Online algorithm detecting the number of fragments hit for a recorded frame after an event trigger.
Fragment-hit spot coordinates	Floating-point number	The pixel coordinates of the deduced center of the spot where the fragment impinges on NICE.
Spot amplitude	Integer number	The maximal numerical intensity of the spot as recorded by the camera in the optical frame.
Spot intensity	Integer number	The integral of the detected spot by the online DAQ algorithm in an optical frame.
iBeam	Boolean	Records the status of ion beam stored in the ring (1= true; 0= false).
eBeam	Boolean	Records the status of electron beam switch. (1= true; 0= false).
Storage time	Double number	Records the time elapsed after the ion beam injection, until the recorded event.
Collision energy (E_{d})	Floating number	Records the tuned energy by the DAQ for electron–ion collision (detuning energy) at the time of the registered event.

Table 4.2: A conceptual list for the recorded variables/quantities for each measurement in an experiment run time relevant for the current analysis.

electron recombination happening at the velocity matched conditions (E_{d}= 0.00 eV) until ∼600 seconds after injection. The plot is produced in figure 4.8. Similarly, it is possible to produce the distance distribution plots for other measured detuning energies (electron-ion collision energies in the center-of-mass frame), E_{cm}, by filtering further on the electron energy value from the recorded data. In the figure plots for 40 meV, 90 meV, and 150 meV plots have been produced for instantiation.

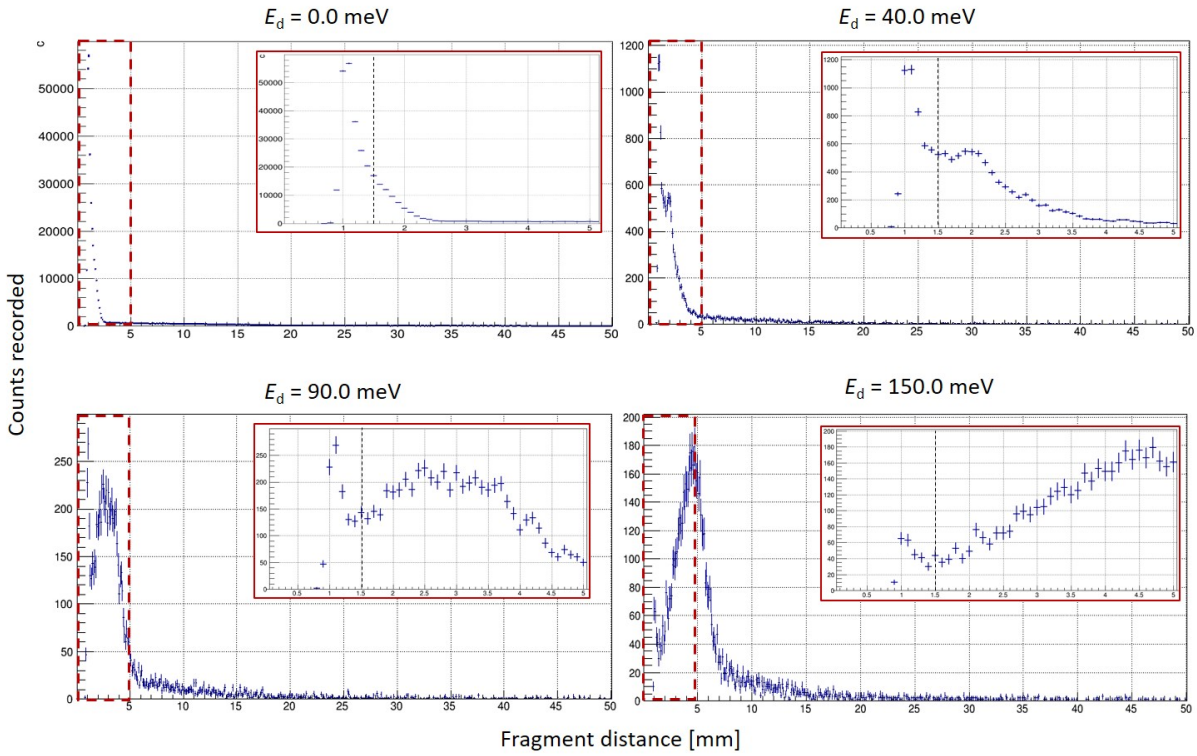

Figure 4.8: A direct raw set of distance plots for $E_{\mathrm{d}} = 0.0, 40.0, 90.0, 150.0$ meV detuning energies, measured between ∼500 to 600 seconds after ion injection in the CSR. The inset image shows a zoomed view at lower distances (0.0− 5.0 mm) in the histogram, with the vertical dashed lines representing the 1.5 mm mark as used in the artifact analysis (see subsection 4.2.1).

Few notable points from the plots at this stage are– the distance distributions are concentrated mainly below distances of 10 mm; the features are visible as a compound smooth distribution which moves further with increase in E_{cm}; and a clear, rather anomalous peak is visible at ∼1 mm. Invoking the ideas developed in section 1.2, it is expected that with higher electron-ion collision energy pumped into the system, with higher E_{cm}, the kinetic energy release (KER) is also directly affected with further channels accessible for the recombination products, as well as due to the simple conservation of energy input in the sys-

tem. This resolves the shifting peak features. Further, due to the low KER, small fragment distances are expected on the detector, which is in line with the observed data, exhibiting high density of events at distances below 10 mm. Further, the anomalous peak at $\sim$1 mm can be attributed to the DAQ algorithm (see section 2.6) which optimizes on the recognition and classification of events recorded in a frame by the NICE detector, using box-selection for identifying the fragment-spot as produced on the phosphor-screen. A real fragment-spot is expected to be a circularly symmetric pixel pattern with a spot-width closely related to the corresponding fragment energy. However, if two fragments hit at a distance smaller than the single spot-width, these features overlap with each other. Consequently, the on-line algorithm while scanning through the frame may recognise the first spot, and cut out the box-selection. This leaves an asymmetric spot feature on the frame, recognised as the second fragment-spot, however, the positioning is not credible. This issue can however be dealt with in the following way: for each impinged fragment spot, the corresponding recorded data also contains spot amplitude and spot intensity (see table 4.2). The spot amplitude can be used as check for separation of a fair event and a dark count, while the spot intensity gives an integral of the pixel-amplitude within the selected box defined in the DAQ algorithm, which can further be used to separate the credibility of the recorded fair spot positions. The effect of the asymmetric box-cut, and thus unfair spot recognition is visible as reasoned, and can be verified in the trends from figure 4.8. The high counts peak at the lower distances near $\sim$1 mm in the 2D fragment distance plots is henceforth termed as a low-distance artifact and reasoning to deal with this has been discussed about further.

4.2.1 Low-distance artifact analysis

As has been pointed out, the counts recorded for the low-distance artifact is directly related to the number of events falling close to the resolution limited distances of the NICE camera. Following logically why for high detuning energies, this artifact gets smaller whereas for low detuning energies, its amplitude is considerably high. It can be noted, the artifact is mainly visible for distances greater than $\sim$1.5 mm, with a visible kink. Further, as deduced from the earlier discussions, this is directly related to the spot-amplitudes and spot-intensities recorded for each event. We try to investigate into the effects of making cuts and checking the distributions for each iteration to understand the effect properly. It is important to note that inversely, the amplitude and intensity of the events is independent of the fragment distances in general. Thus, the aim is to find an optimal solution to negate the events accumulating in the artifact peak, while still keeping the statistics from the rest

of the curve identical to the original. A plot for the raw data measured from ∼500 to 600 seconds after the injection in the ring, with electron and ions tuned to 0.0 eV collision energy has been shown in the figure 4.9, with a distance range covering 0.0 to 8.0 mm fragment separation.

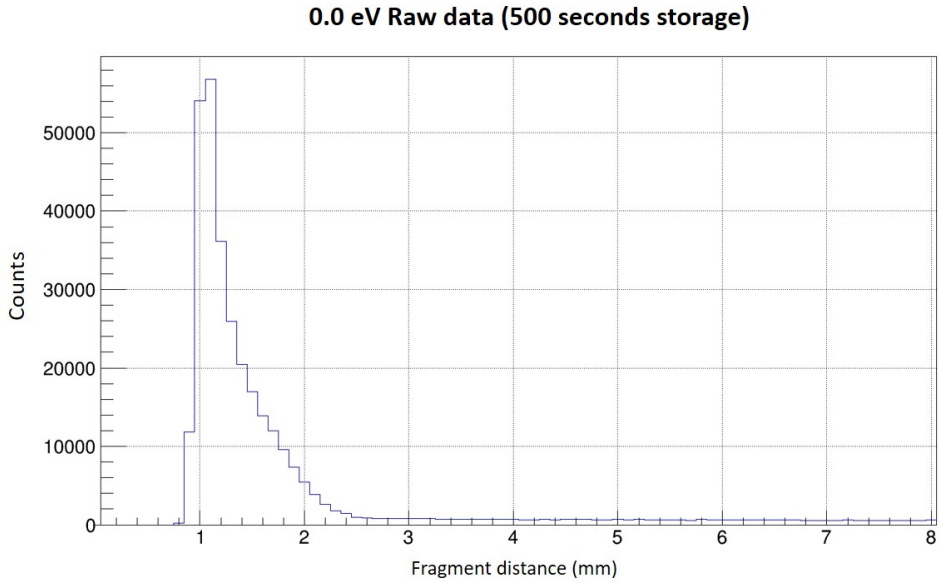

Figure 4.9: A plot for the raw data measured from ∼500 to 600 seconds after the injection in the ring, with electron and ions tuned to 0.0 eV collision energy.

To find an optimal filtering condition for the data, we investigate into the trends for the ratio of spot intensities (sIratio) of the second recorded fragment spot ($sI(2)$) with the first ($sI(1)$), given as:

$$\text{sIratio} = \frac{sI(2)}{sI(1)} \tag{4.4}$$

A plot of sIratio for the data measured for E_{d}= 0.0 meV (see plot 4.9), filtered to include only the events with electron and ion beams on, and ones with two recorded fragments, is shown in the figure 4.10.

It can be observed that sIratio shows an anomalous peaking behaviour near ratios less than 0.1, wherein the plot grows three times in count magnitude. This is also consistent with the discussion earlier about the hypothesis for the origin of the artifact. Further, investigation of a similarly defined ratio for the spot amplitudes (sAratio) revealed that the data was isotropically distributed over all amplitudes, verifying the aforementioned assumption. To delve further, we try to make cuts on the sIratio systematically and note the number

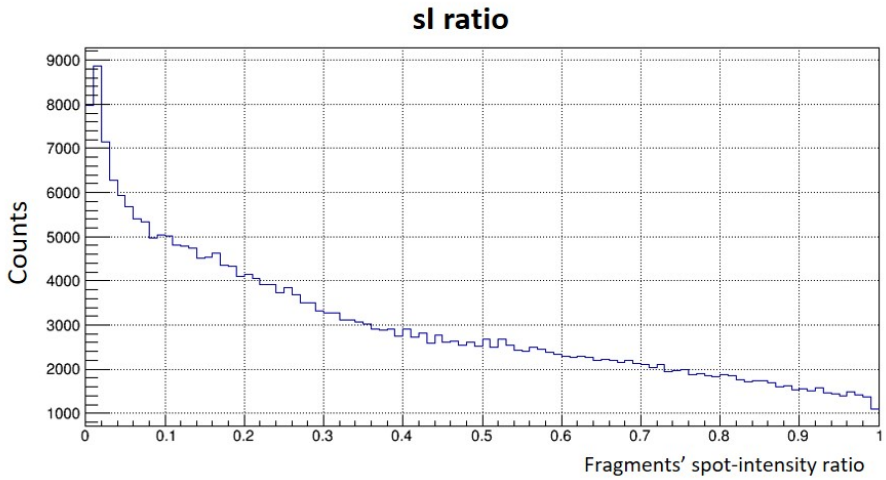

Figure 4.10: A plot depicting the ratio of spot intensities (sIratio) of the second recorded event with the first, generated for the dataset measured with E_{d}= 0.0 meV as plotted in figure 4.9. The plot depicts raw data filtered to include only the events with electron and ion beams on, and wherein two fragments were detected.

of events cut out from the distribution in each case. The comparative figures have been produced in 4.11.

To analyse the effect of changing the sIratio parameter, we use the following procedure– first, we list out the curve integral divided in two intervals, $\Pi^{\mathrm{sI}}_{\mathrm{left}}$ (left integral with limits 0.0 - 1.5 mm) and $\Pi^{\mathrm{sI}}_{\mathrm{right}}$ (right integral with limits 1.5 - 8.0 mm), where the superscript denotes the $sIratio$ threshold value used for the plots that the integrals are calculated for. The lower threshold of 1.5 mm is defined conservatively based on the discussion regarding the detector resolution, qualitatively ratified by the sharp, noticeable kink in the 2D fragment distance plots at distances consistently close to of less than $\sim$1.4 mm, as visible in figure 4.8. The left interval can be seen as the one contributing majorly to the artifact, whereas the right interval for the most part consists of fair data. This is done systematically for different values of sIratio from 0.1 to 0.4. To compare these values, we normalise them using the value of raw data counts, or the total left and right section counts at sIratio = 0 threshold. This then gives the fraction of counts left with each succeeding sIratio cut. Understandably, the aim is to find an optimal trade-off in an interval wherein the left integral decreases maximally, and starts showing saturating behaviour (for further threshold cuts), while the right integral decrease is the minimal to preserve the fair statistics. To ease the comparison, this is further listed as consecutive differences to depict the trends in the data, i.e. $\Pi^{0.10}_{\mathrm{left}} - \Pi^{0.15}_{\mathrm{left}}$, $\Pi^{0.15}_{\mathrm{left}} - \Pi^{0.20}_{\mathrm{left}}$, and so on, similarly for the right section, denoted by Π_{right}. The table for the data accumulated for E_{d} = 0.0 eV, measured after $\sim$500 seconds of ion storage,

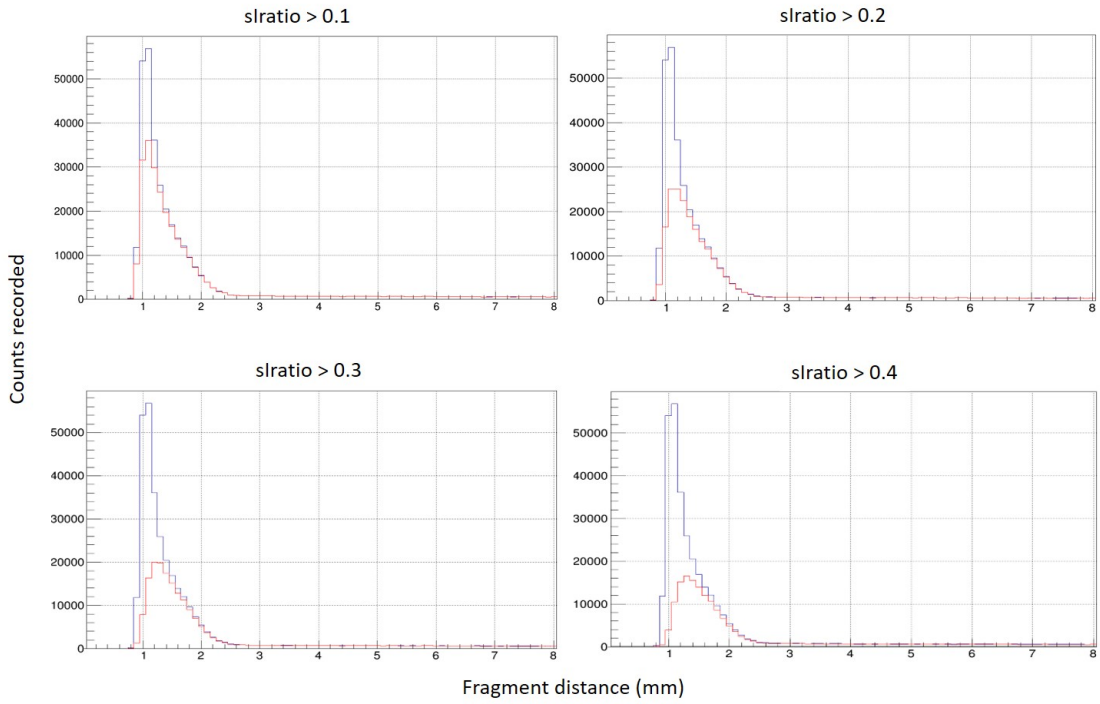

Figure 4.11: A plot depicting the sIratio cuts on the data measured for 100 seconds with E_{d}= 0.0 meV, after ∼500 seconds of storage. The raw data is shown in blue while the data after the implemented cut is depicted in red. The dashed line represents the 1.5 mm mark used for calculating count integrals as in table 4.3.

until ∼600 seconds has been produced in table 4.3. From the data it can be observed that the difference in the left integral, Π_{left}, keeps decreasing until the 0.25-0.3 data, where it reaches a minimum decrease and then it increases again. This can be attributed to the idea that as the irrelevant counts are cut out, the (relative) percentage difference keeps increasing but it reaches a minimum when reached around the optimal threshold for false events. Further on, the relative difference value increases again and saturates as then the filtered events are more or less uniformly distributed. On the right side, Π_{right}, the percentage difference is chosen such that it can be maintained to a minimal decrease, in the optimal range obtained from the left side trends. This is seen, as shown, in the 1.5 mm cut at the 0.25 – 0.3 range. This trend is concurrent for the procedure when repeated for distance cuts of 1.7 and 1.9 mm as well, which defines the sIratio= 0.3 as our cut selection for the current data. Further, given the $sIratio$ threshold, it is also important to note that the artifact makes the data statistics at low-distances inexact, wherein the fragment distance counts are not fairly represented. The quantitative reasoning for choosing a lower threshold for the credible data follows from our investigations which show that the data above 1.6 mm is not

sI ratio	Π_{left}^{sI}	Π_{right}^{sI}	$\Pi_{left}^{sI}/\Pi_{left}^{0.0}$	$\Pi_{right}^{sI}/\Pi_{right}^{0.0}$	$\left(\frac{\Pi_{left}^{sI(i-1)} - \Pi_{left}^{sI(i)}}{\Pi_{left}^{0.0}}\right) \times 100$	$\left(\frac{\Pi_{right}^{sI(i-1)} - \Pi_{right}^{sI(i)}}{\Pi_{right}^{0.0}}\right) \times 100$
> 0.0	222308	112244	1.0	1.0	-	-
> 0.10	166115	110471	0.747	0.984	25.3	1.58
> 0.15	146045	109542	0.657	0.976	9.02	0.83
> 0.20	127771	108338	0.575	0.965	8.22	1.07
> 0.25	111816	106719	0.503	0.951	7.18	1.44
> 0.30	97933	104739	0.441	0.933	6.24	1.76
> 0.35	86217	102305	0.388	0.911	5.27	2.17
> 0.40	76087	99270	0.342	0.884	4.56	2.70

Table 4.3: Table listing the Π_{left} (limits 0.0 - 1.5 mm) and Π_{right} (limits 1.5 - 8.0 mm), the left and right count integrals respectively, for changing sIratio thresholds, their normalised percentages to $\Pi^{0.0}$ values, and the consecutive difference between the percentages to finalise on an sIratio cut for dealing with the low-distance artifact in the obtained data.

affected significantly by the artifact from the spot-recognition algorithm. Thus, we remark that the obtained 2D transverse fragment distance imaging data can be interpreted credibly for distances $>$ 1.6 mm, which has been marked as a dashed vertical line in the recorded data plots produced henceforth.

4.2.2 Residual-gas background subtraction

The data counts recorded on the NICE detector are not completely contributed by the intended measurement (c_{m}), but are a sum of the counts produced as a result of the ion reaction with the residual background gas (c_{bg}), electron induced reactions with the contaminant ions (c_{ci}) from the ion source stored in the ring (see sec 3.1 for more details), and the dark counts due to the detector electronics. This can be represented as:

$$c_{\mathrm{total}} = c_m + c_d + c_{bg} + c_{ci} \tag{4.5}$$

As mentioned in the table 4.2, the recorded physical quantities for each measured event can be used to filter and extract only the relevant events from the stored data. While we deal with the counts induced due to contaminant ion-electron reactions, c_{ci}, in detail in chapter 5, the c_{d} and c_{bg} contributions can be accounted for simultaneously using proper filters on the data as an immediate step to remove the systematic disparities in the recorded counts.

In the CSR, the residual gas pressures of 10^{-14} mbar have been achieved [5], indicating the the general conditions at the experimental chambers are extremely well-suited for such studies. In the experimental beamtime for the TiO^+, the residual gas pressures were low and maintained steady, which led to a very low residual-gas background rate count. The systematic procedure for finding the precise background counts and subtracting it from the data has been described further.

Here, we consider that once the TiO^+ ions are injected in the CSR, they can be stored without making them react with the electrons explicitly for thousands of seconds, appropriately quantified by a lifetime of $>$1100 seconds, after which time the ion beam intensity is observed to be reduced to $1/e$ times the initially injected. This slow decay process is majorly defined by the stored beam tuning in the ring, as well as the background reaction count rate with the residual-gas which can provide exit pathways for the stored ions. Further, in case of electron beam switched on, various effects step in, viz. the electron-ion targeted DR interaction leading to neutral products, and the effects due to the charged beam interactions leading to ion beam tune shifts (see sec. 2.2), leading to a loss of the stored beam.

The reactions with background gas may be recorded by the detector if this happens close to the electron-cooler section in the CSR, leading to neutral products. Thus, it is vital to understand and systematically subtract this background, a characteristic of which is that it can be assumed to be independent of the presence of the electron beam, given that the reaction happens between the residual gas and the stored ions. Consequently, these events can be segregated from the recorded set of events by filtering on the electron beam status, which is a boolean parameter. In the measurement scheme, an electron beam 'off-step' is generally included to account for the same. To use the events recorded in this case, the fragment distances are calculated as per the usual procedure, and a histogram is made. This fragment distance distribution histogram can then be scaled, using the ratio between the time dedicated in the run to the 'off-steps', and the time dedicated to the actual measurement at a given detuning energy in the 'measurement-step' of the run. Once this background is scaled, the errors are calculated appropriately, and this is then subtracted bin-wise from the measured histogram, with the errors propagated faithfully. A representation of this procedure in different stages has been shown in the figure 4.12.

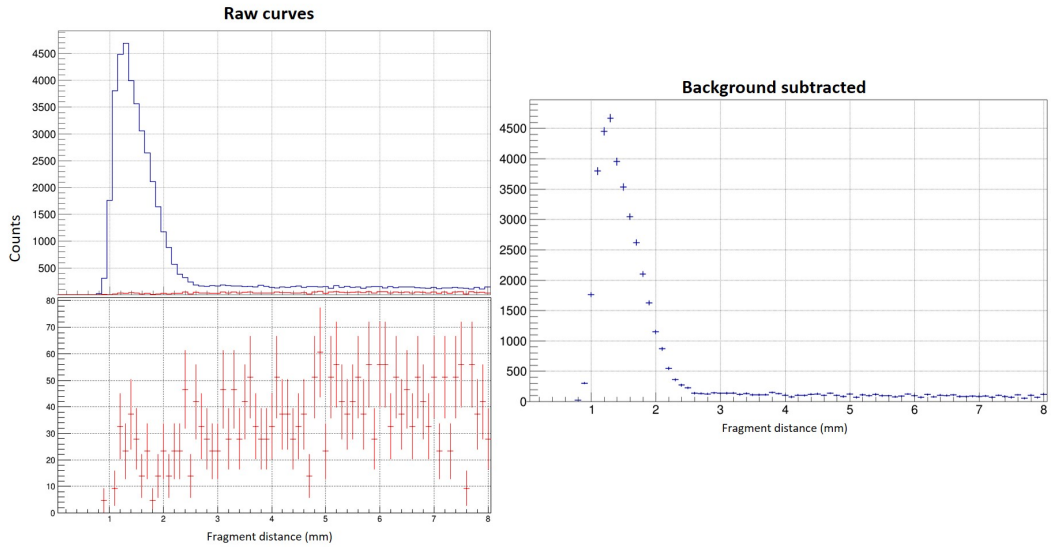

Figure 4.12: The plots have been produced for the $E_{\mathrm{d}} = 0.0$ meV runs measured after $\sim$500 seconds of storage in the ring. The plot on the top left shows the recorded signal data in blue containing all the contributions (c_{total}) as mentioned in eqn. 4.5, filtered to omit the low-distance artifact (sIratio >0.3); while in red is the scaled residual-gas background (c_{bg}) in the same curve. On the curve directly below, the unscaled residual gas background (with dark counts contribution included) histogram has been plotted with the relevant error bars, acquired in the measurement by recorded the signal on NICE detector with electron beam switched off. On the right is produced the fragment distance histogram obtained after the subtraction of background from the raw data.

4.2.3 Final imaging data plots

Produced below are the fragment distance distribution plots obtained for the TiO^+ molecular ion undergoing the dissociative electron recombination process during the experiment at the CSR, wherein the reaction was studied under various storage time and detuning energy conditions. The produced plots show the measured data as listed below:

- 0 seconds storage (measurement: $\sim$0.0 to $\sim$100 sec after injection)
  - E_{d} = 0.0 meV (figure 4.13)
- 500 seconds storage (measurement: $\sim$500.0 to $\sim$600 sec after injection)
  - E_{d} = 0.0 meV (figure 4.14)
  - E_{d} = 10.0 meV (figure 4.17)
  - E_{d} = 20.0 meV (figure 4.17)
  - E_{d} = 30.0 meV (figure 4.17)
  - E_{d} = 40.0 meV (figure 4.17)
  - E_{d} = 60.0 meV (figure 4.18)
  - E_{d} = 90.0 meV (figure 4.18)
  - E_{d} = 120.0 meV (figure 4.18)
  - E_{d} = 150.0 meV (figure 4.18)
- 1000 seconds storage (measurement: $\sim$1000.0 to $\sim$1100 sec after injection)
  - E_{d} = 0.0 meV (figure 4.15)
  - E_{d} = 60.0 meV (figure 4.19)
  - E_{d} = 90.0 meV (figure 4.19)
  - E_{d} = 120.0 meV (figure 4.19)
- 1500 seconds storage (measurement: $\sim$1500.0 to $\sim$1600 sec after injection)
  - E_{d} = 0.0 meV (figure 4.16)

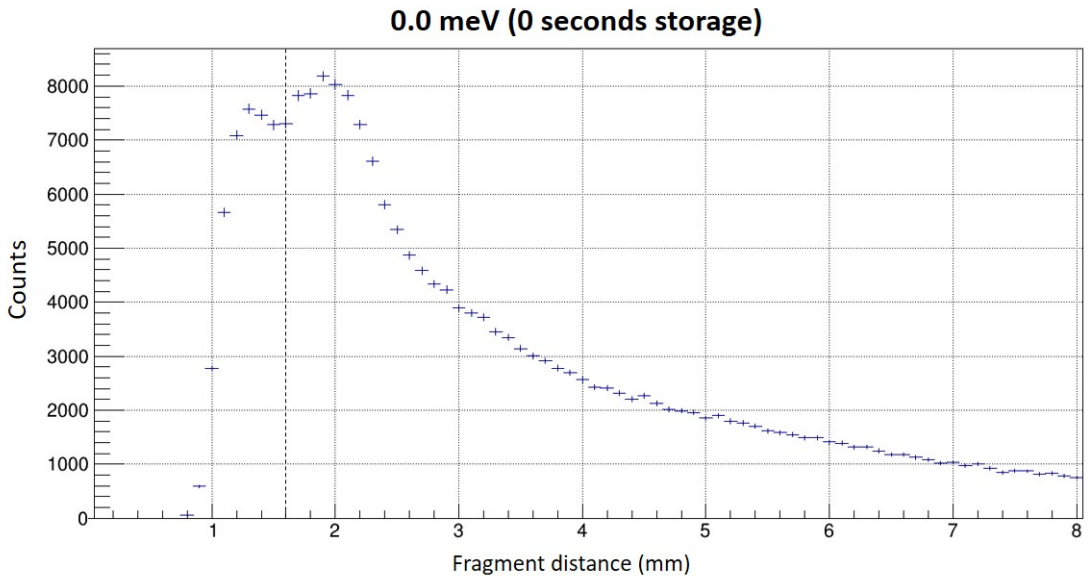

Figure 4.13: The final plot for data recorded between 0 to ∼100 seconds measurement for $E_{\mathrm{d}} = 0.0$ meV.

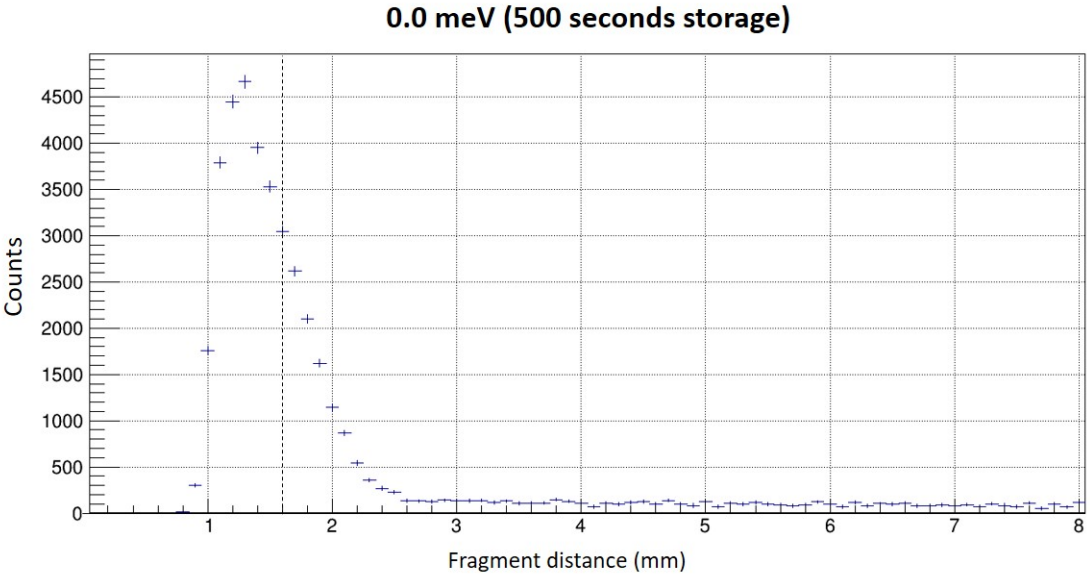

Figure 4.14: The final plot for data recorded between ∼500 to ∼600 seconds measurement for $E_{\mathrm{d}} = 0.0$ meV.

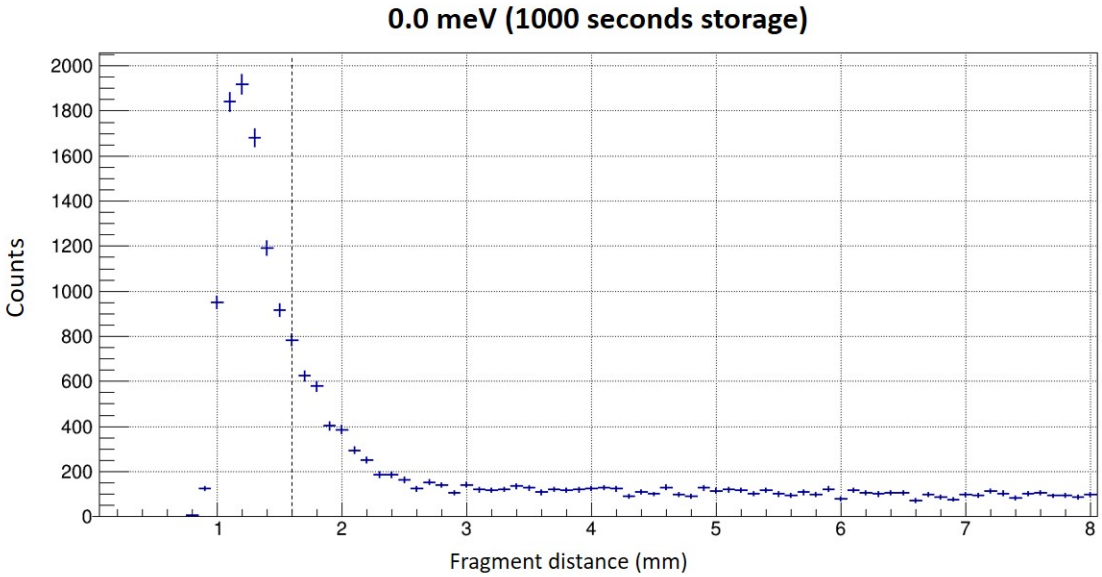

Figure 4.15: The final plot for data recorded between ∼1000 to ∼1100 seconds measurement for $E_{\mathrm{d}} = 0.0$ meV.

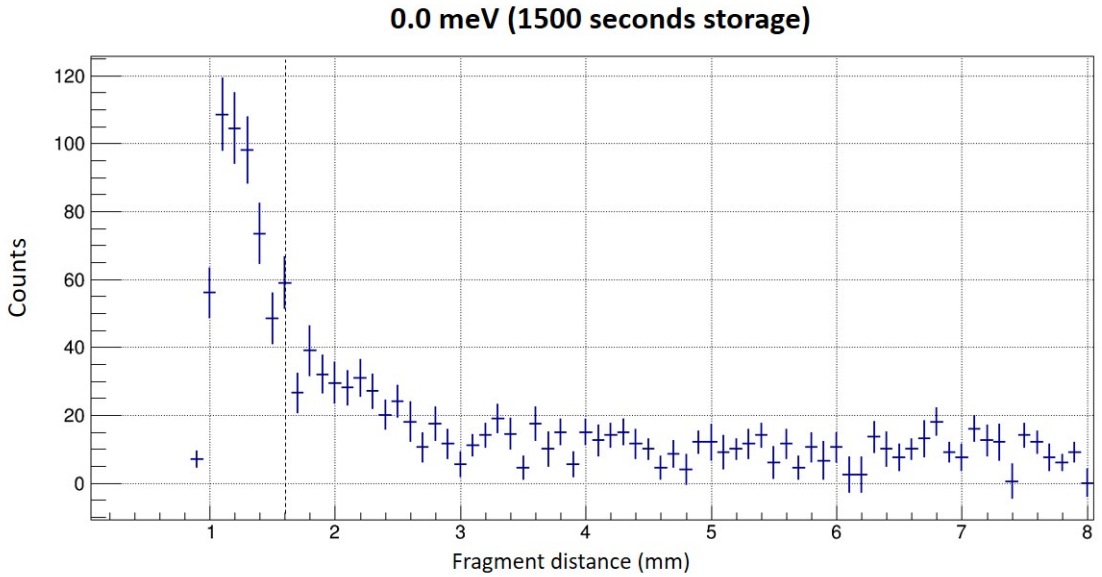

Figure 4.16: The final plot for data recorded between ∼1500 to ∼1600 seconds measurement for $E_{\mathrm{d}} = 0.0$ meV.

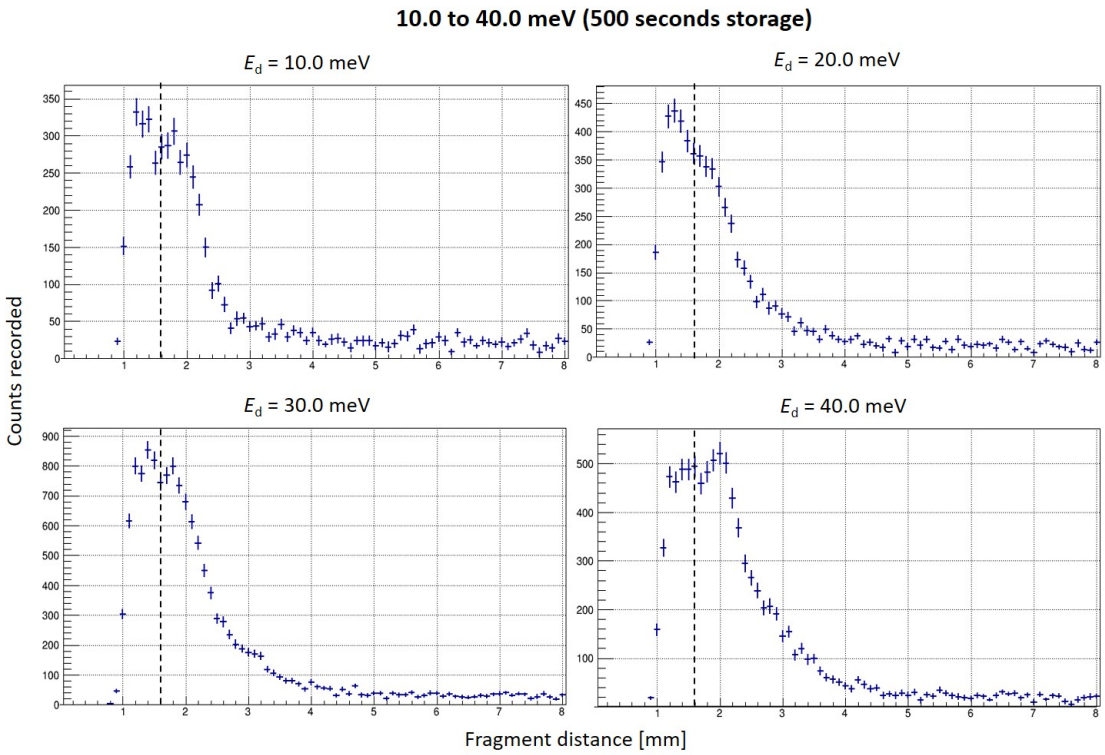

Figure 4.17: The final plot for $E_{\mathrm{d}} = 10$, 20, 30, and 40 meV (measure ∼500- 600 sec).

It is interesting to note a few characteristics about the curves at this point to understand the further course of analysis, as well as how the multiple dimensions in the data can be utilized for better visualization.

- **0.0 eV Data**: This data group comprises of different times of storage with excellent statistics available owing to the fact that it corresponds to the cooling energy, i.e. the velocity matched condition between the electron and ion beam, which is a recurring step in the measurement scheme. Thus, the data for this category is recorded for the rate intensive as well as the imaging intensive runs, and can be used cumulatively. As discussed in the section 1.1 that for a DR reaction, in general, the velocity matched condition is the regime where the process has the highest cross-sections for recombination, thus the maximal rates. Further, the E_{d}= 0.0 eV case also corresponds to an isotropic recombination cross-section which is independent of the molecule orientation (in the θ direction). Consequently, the 0 eV data presents an essential dataset to understand the dynamics of the reaction in the fundamental details. From the figures 4.13, 4.14, 4.15 and 4.16, depicting the 0 eV detuning data recorded for 0 sec, 500 sec, 1000 sec, and 1500 sec storage times, it can be observed that the feature at

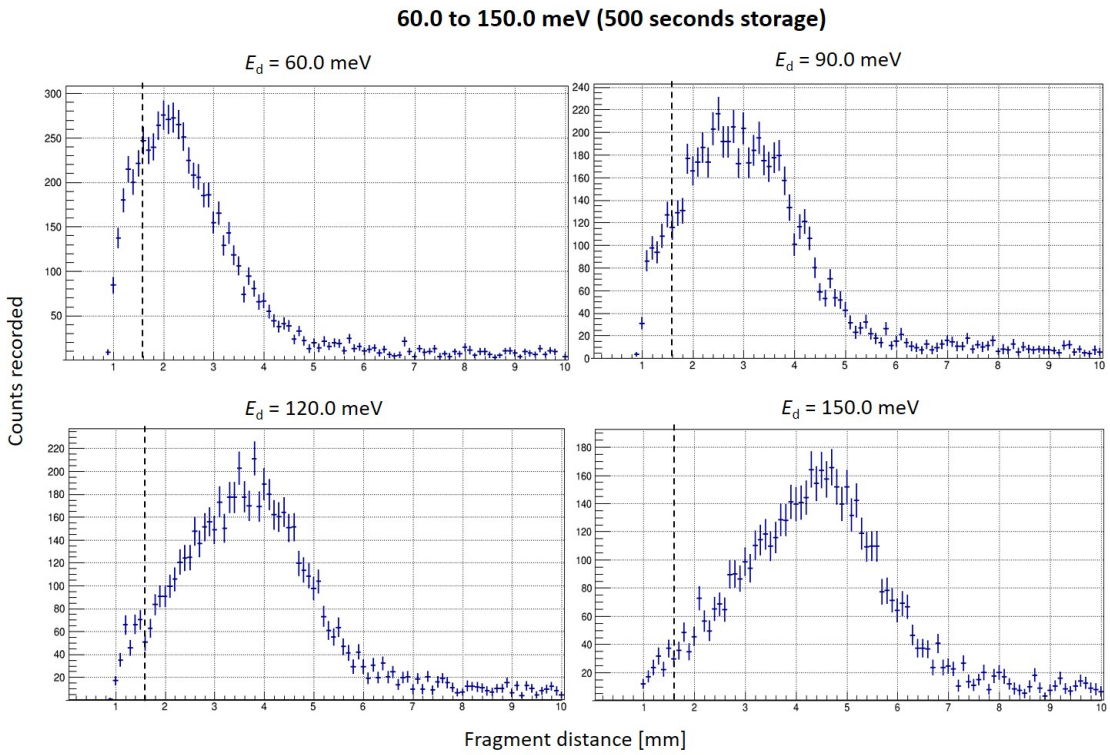

Figure 4.18: The final plot for $E_{\mathrm{d}} = 60$, 90, 120, and 150 meV ($\sim$500-600 sec measurement). Note the X-span from 0.0 to 10.0 mm included to exhibit the farthest extents of the 2D fragment distributions at high E_{d}.

$\sim$1.6$-$2 mm decreases over time. This possibly can be attributed to the rovibrational cooling of the molecule, which may also be coupled with other effects such as electronic dexcitation of the excited states to ground state population, which gets closer and closer to going below the threshold for an 'endothermic' reaction in such case.

To investigate the significant amplitude of events in the 0 to $\sim$100 second measurement (0 second storage) at even 6 mm distance, it is instructive to make time cuts for the data, which has been presented in figure 4.20 with changed extents of the X-axis. The considerably large extent of distances observed for the fragments is undoubtedly an interesting facet of the data. It is also interesting to note that the measurement made without ion storage in the ring suggests the presence of highly populated rotational and vibrational states of the molecule freshly introduced in the ring from the source. This can be further investigated by contrasting the 0-100 sec measurement data with 500-600 seconds measurement with similar time cuts (see figure 4.21). It can be noticed for the measurement made after 500 seconds the distance distributions fit back within 6 mm span.

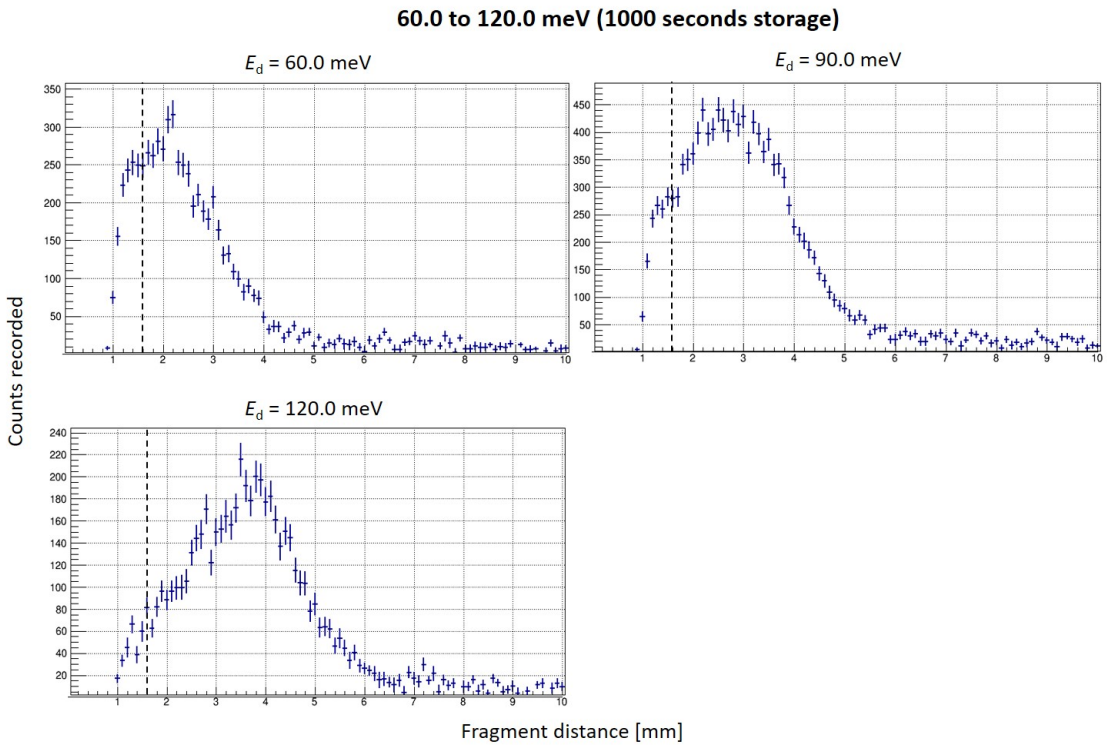

Figure 4.19: The final plot for data recorded between ∼1000 to ∼1100 seconds measurement for $E_{\mathrm{d}} = 60$, 90, and 120 meV. Note the X-span from 0.0 to 10.0 mm included to exhibit the farthest extents of the 2D fragment distributions at high E_{d}.

- **500 seconds storage data**: This data group comprises of the the measurements performed after waiting 500 seconds from the ion beam injection inside the CSR. The procedure allows for probing into the rovibrationally relaxed states of TiO^+ (see sec. 3.3) wherein measurements have been made at various detuning energies, viz. 0, 10, 20, 30, 40, 60, 90, 120, 150 meV. The dataset has good statistics and thus low error bars on the obtained points. Rather sharp features can be observed in the 10 and 40 meV data which are either emergent or absent in the 20 and 30 meV plots. The most obvious features in the low detuning energy plots do not seem to shift to higher distances (which would correspond to higher KER), whereas the shapes evolve subtly in the similar region. This regime of dataset also presents a possibility to estimate the energetics of the reaction based on the ideas discussed in section 1.2. Moving further in the detuning energies to E_{d}= 60 meV and above, an evident intensity shift towards higher distances and a smooth broad distribution alongwith can be noticed. These can be attributed to the energy levels crowding up closely in the region, leading to multiple closely spaced channels in energy, and thus producing a cumulative effect.

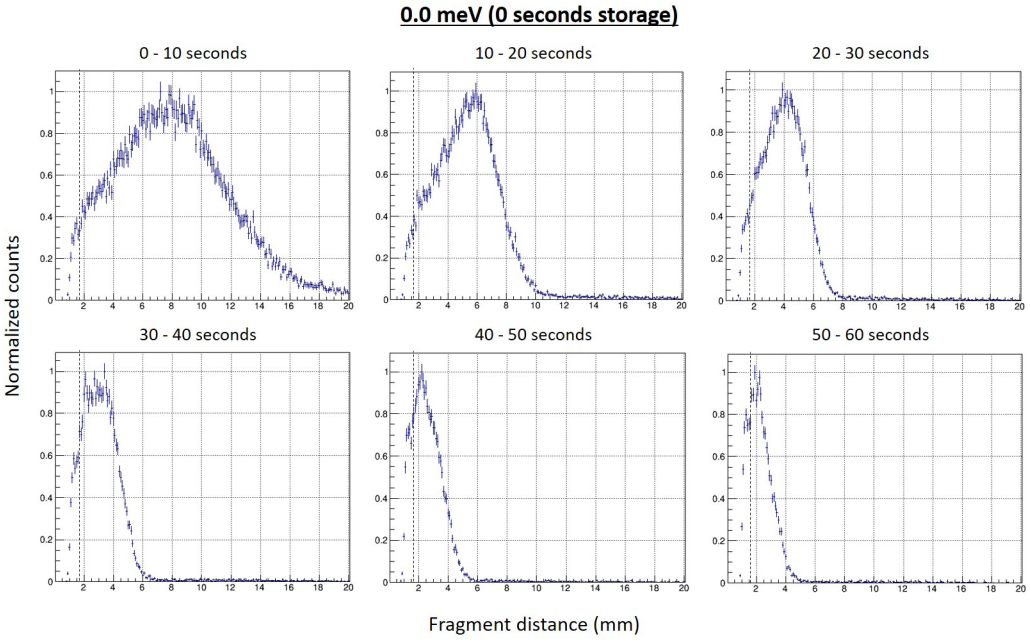

Figure 4.20: Time cut plots for the measurements made between the times 0−60 seconds after the ion injection in the ring. The X-axis shows fragment distances in mm (note the range 0−20 mm), while Y-axis shows the counts normalised to the maximum in each panel.

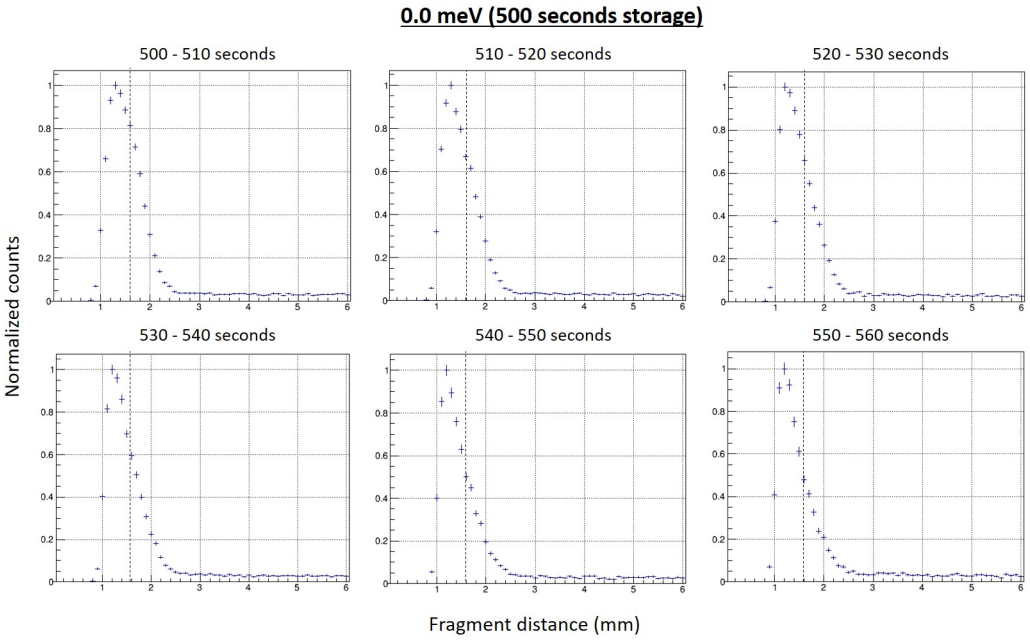

Figure 4.21: Time cut plots for the measurements made between the times 500−560 seconds after the ion injection in the ring. The X-axis shows fragment distances in mm (note the range 0−6 mm), while Y-axis shows counts normalised to the maximum in each panel.

4.3 Fragment distance distribution simulation

Electron-ion recombination is a statistical process. In order to study and determine the rate constants of such reactions, it is sufficient to measure the number of resultant product species in a suitable arrangement. However, at the CSR, it is possible to study the energetics of such reactions in great detail as well, with the use of the neutral fragment imaging detector NICE (refer to 2.6). In order to study the energetics of the DR for TiO^+ molecular ion, it is imperative to study the further statistical effects that come into play due to the geometrical considerations of the experimental conditions and the setup. These statistical effects can be modelled using analytical considerations, which has adroitly been used in previous works such as in Z. Amitay et al [68] to understand and identify the participating channels in the DR process of CH^+ molecular ion, using the 2D fragment distribution modelling and comparing it with the obtained data. Another effective way to implement this is using the Monte-Carlo (MC) modeling method, which has been used in this work. Similar methods have also been used previously, as in the work of O. Novotny et al [30] the MC-simulations were used to study the plasma DR rate coefficient.

The first step in implementation of such a procedure is to generate a MC-model that includes the physical effects, and represents the experimental reality of the 2D fragment distance distribution from a single KER channel as closely as possible. This forms the subject matter of this section wherein realistic effects have been defined in steps segregated as collision modelling, followed by fragmentation modelling, finally completed by the inclusion of detection model. This MC-model is ultimately followed on by its application in the generation of a composite picture for multiple KERs arising from various initial and exit channels for the specific molecule under consideration, and using a rationally defined fitting method to discover the energetics of the DR, which has been discussed in detail in chapter 5.

4.3.1 Collision model

Consider a DR induced by an electron with energy E_{cm} in the center-of-mass frame of the ion-electron system, leading to neutral Ti and O fragments. If the initial (rovibrational) molecular energy level is considered to have an energy difference of $E_{i,f}(E_i - E_f)$ with respect to the asymptotic final electronic states of the fragments, the kinetic energy release

in the reaction is given by,

$$E_{\mathrm{KER}} = E_{\mathrm{cm}} + E_{i,f} \tag{4.6}$$

It is important to note here that for general DR reaction, which is exothermic, the quantity $E_{i,f}$ is a positive quantity, whereas here, the endothermicity hypothesis for the reaction proposes the possibility for $E_{i,f} < 0$. The E_{KER} is manifested as the kinetic energy of the product fragments, velocity vectors for which may be randomly distributed over a finite sized sphere, in accordance with the conservation laws of momentum and energy. Given that the initial energy of the ion in the storage ring U_{acc} ($\gg E_{\mathrm{KER}}$), the fragments after breakup separate out within a conical span along the ion beam direction. The transverse projection of the distance between fragments (d) recorded by a detector placed at a distance D away from the recombination point perpendicular to the initial ion beam velocity is given by,

$$d = D\frac{m_{\mathrm{Ti}} + m_{\mathrm{O}}}{\sqrt{m_{\mathrm{Ti}}\, m_{\mathrm{O}}}} \left(\sqrt{\frac{E_{KER}}{U_{acc}}}\right) \sin\theta \tag{4.7}$$

where, m_{Ti} and m_{O} are fragment masses for Titanium and Oxygen, and θ is the angle of molecular internuclear axis orientation with respect to the ion beam direction at the time of recombination (see fig 4.29).

This simple picture is complicated by the inclusion of various physical effects, which we now include stepwise. Firstly, the angle θ is not precisely known for each recombination event, thus a single E_{KER}, results in a distribution of 2D fragment distances d, accounting statistically for all projections. The MC-simulation result for the situation has been produced in figure 4.22, assuming a E_{KER}= 5.0 eV, and U_{acc}= 280.0 keV.

Secondly, the molecular ions stored in the CSR are merged with the electron beam for the reaction over a distance of $\sim$1 m in the interaction zone. This gives a longitudinal spread in the exact position of dissociation for the molecule, D, spanning from s_1 =3296.685 mm upto s_2 =4317.315 mm, and thus, the measured projected distance distributions are an average over the Z-coordinates in the interaction length.

Third, a physical picture of the ion beam demands a finite beam size, which according to the CSR characteristics, is a Gaussian-like distributed density of particles in the transverse cross-section. The Gaussian distribution in the two transverse direction need not be symmetrical ($\sigma_x^{\mathrm{ion}} \neq \sigma_y^{\mathrm{ion}}$). Further, given the ion beam energy (U_{acc}) is very high in comparison to the energy distribution of the ions produced in the source, the stored beam can

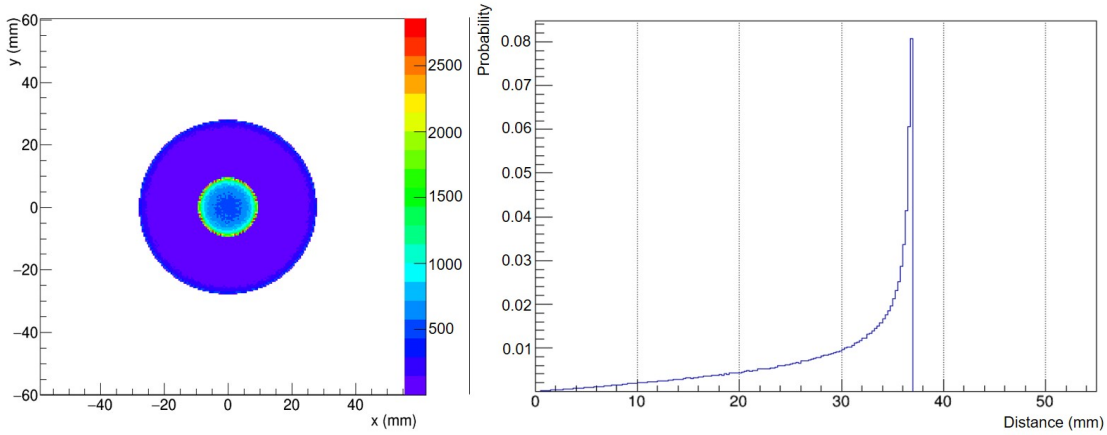

Figure 4.22: A 2D transverse fragment distance distribution (right) simulated for TiO^+ beam with 280 keV energy, fragmenting into Ti (48 u) and O (16 u) assuming a kinetic energy release E_{KER} =5 eV for dissociation occurring from a single point. On left is the fragment distribution (shown as z-axis– coloured by intensity) as seen on the detector accumulated for 10^6 Monte-Carlo trials.

be assumed to be monoenergetic with a mean velocity v_{ion} along the beam direction, given by

$$v_{ion} = \sqrt{\frac{2\,U_{acc}}{M}} \tag{4.8}$$

where $M \sim 64\ u$ is the mass for TiO^+ ion. It is instructive to note that for a typical value of $U_{\mathrm{acc}} = 280$ keV, the velocity for TiO^+ ion comes out as $\sim$926100 m/s.

Similarly, realistic model for the electron beam accounts for a finite-sized cylindrical beam (radius R_{e}) with a uniformly distributed particle density. Combined with the ion-beam spread, this gives a transversal uncertainty in the exact location of dissociation as well. A MC-simulation output for the effects introduced uptil this point has been produced in figure 4.23. Further, as the measurements at eCool are aimed at (or close to) the velocity matched conditions for the electrons and ions ($v_{\mathrm{e}} = v_{\mathrm{ion}}$), the electron energy is set to match the ion velocity, or the aimed ion-electron collision energy, termed as the detuning energy E_{d} (see eqn. 2.29). This translates to typical energies on the order of a few eV in the lab frame, making it imperative to consider the detailed contributions determining the electron beam velocity distribution, given as:

$$\vec{v_e}(r) = \vec{v}_{ion} + \vec{v}_d + \vec{v}_T + \vec{v}_{sc}(r) \tag{4.9}$$

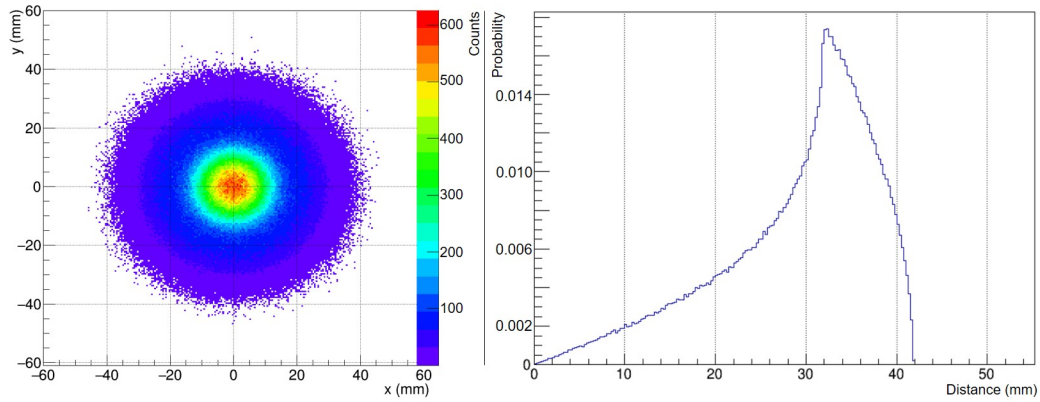

Figure 4.23: A realistic 2D transverse fragment distance distribution (right plot) simulated for TiO^+ beam with 280 keV energy, fragmenting into Ti and O assuming E_{KER}= 5 eV. Dissociation occurs with a uniform probability along the 1.02 m long interaction region, for an assumed 2D Gaussian ion beam with $\sigma_x^{\mathrm{ion}} = \sigma_y^{\mathrm{ion}} = 5$mm, and a cylindrically symmetric electron beam (10 mm diameter). On left is the fragment distribution (shown as z-axis–coloured by intensity) as seen on the detector accumulated for 10^6 Monte-Carlo trials with the cuts as mentioned previously.

here, the $(\vec{v}_{\mathrm{ion}} + \vec{v}_{\mathrm{d}})$ defines the set velocity in the absence of any other systematic uncertainties wherein $\vec{v}_{\mathrm{d}} = (\sqrt{2E_{\mathrm{d}}/\mu})$ is directed along the ion beam direction. The realistic scenario claims for corrections due to the electron beam kinetic temperature $\vec{v_{\mathrm{T}}}$, and due to the electron beam space-charge effects, $\vec{v}_{\mathrm{sc}}(r)$, which is dependent on the radial position of the electron from the beam center in the finite sized charged beam. Further, the electron-ion beam merging geometry in the eCool causes a vectorial redistribution of the velocity components for individual particles, which has been discussed later.

The cold electron beam produced at the CEEB has an isotropic velocity distribution in equilibrium with the cathode temperature ($\sim$27 meV/k_B), which is further reduced using various techniques (refer to section 2.3.1), finally reaching values of $T_\perp$= 3.0 meV/k_B and $T_\parallel$= 0.3 meV/k_B. This gives rise to a Gaussian velocity distribution included in the $\vec{v}_{\mathrm{T}}$ about zero mean, with the σ^{e} parameters given by:

$$\sigma^e_{x,y} = \sqrt{\frac{k_B \cdot T_\perp}{m_e}} \quad , \quad \sigma^e_z = \sqrt{\frac{k_B \cdot T_\parallel}{m_e}} \tag{4.10}$$

in the units of m/s, where k_B is the Boltzmann constant, and m_{e}, the electron mass. This gives a maximum velocity of 22970 m/s transversally and 7260 m/s longitudinally in the lab frame, within the edges of σ spread, for the assumed kinetic temperatures as mentioned

above.

The second contribution, $\vec{v}_{\rm sc}$, comes along due to the space-charge effect of the electron beam. This is based on the idea that in case of a charged beam, the particles at a distance r from the center are at a different electric potential as compared to the beam center. In the drift-tube mode of operation (see section 2.3 and 3.2.1) the electron beam is initially accelerated with respect to the negative cathode potential to the ground, and then is decelerated at the drift tube, finally reaching the set detuning energy for the run. Thus, the relative potential difference from the beam center of a particle at distance r, gives rise to a distribution in the beam energy. From the results of electrodynamics, we know that for a cylindrically uniform beam with current *I* flowing through it and surrounded by coaxial metal cylinder, the electric potential in its vicinity is defined as:

$$\phi(r) = \frac{I}{4\pi\epsilon_0 v_e} \begin{cases} 2\,ln\frac{R_0}{R} + 1 - (\frac{r}{R})^2, & \text{if } r \leq R \\ 2\,ln\frac{R_0}{r} & \text{if } r > R \end{cases} \tag{4.11}$$

where *I* is the beam current, v_e is the center-particle velocity in the beam, R is the beam radius, and R_0 is the radius of the surrounding metal cylinder. The electron energy in the lab frame, $E_{\rm lab}$, including the space-charge effect correction, is given as :

$$E_{lab}(r) = eU_{dt} - eU_{contact} - \frac{Ie}{4\pi\epsilon_0 v_e}\left(1 + 2\,ln\left(\frac{R_0}{R_e}\right) - \left(\frac{r}{R_e}\right)^2\right) \tag{4.12}$$

naturally, the equation is valid for $r < R_{\rm e}$, and here, e is the electronic charge, U_{dt} is the set drift tube voltage, $v_{\rm e}$ is the particle velocity in lab-frame at the electron beam-center, $R_0 =$ 50 mm is the CSR tube radius, electron beam radius is denoted as $R_{\rm e}$, and the cathode's contact potential as $U_{\rm contact}$. To elucidate this effect, the potential difference of a particle at a radial distance r (mm) in the electron beam with respect to the beam center is shown in the figure 4.24 for a lab-frame energy 2.4 eV ($E_{\rm d} = 0.0$ meV; velocity matched condition for the TiO^+ ion beam at 280 keV with electrons), and also for 3.75 eV ($E_{\rm d} = 150$ meV). It can be observed from the figure 4.24 that the potential difference reaches as high as $\sim$49 meV towards the outer edge of the beam. To instantiate the effect, consider the case with $E_{\rm d}$= 10 meV. The lab-frame electron-ion collision energy is calculated by rearranging the expression given in 2.29 for $E_{\rm e}$ analogous to $E_{\rm lab}$ here,

$$E_{lab} = \left(\sqrt{E_{cool}} + \sqrt{E_d}\right)^2 \tag{4.13}$$

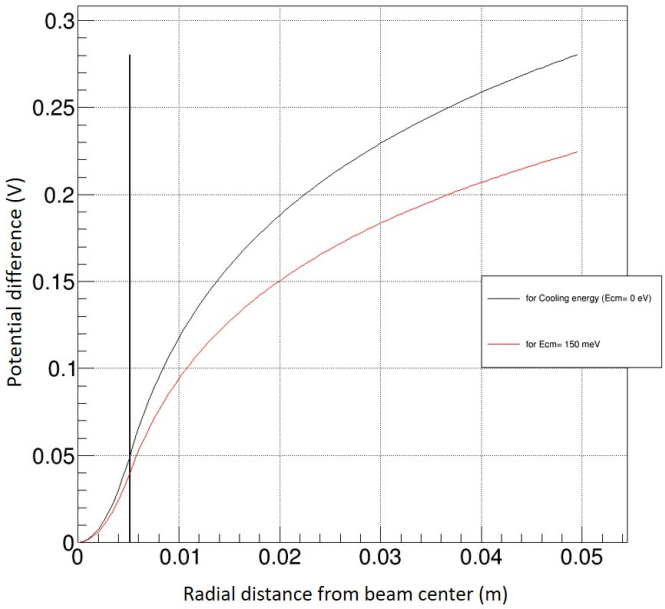

Figure 4.24: Potential difference (Y-axis, in Volts) between the electron beam centre and at a radial distance r away (X-axis, in meters). The black curve represents the electron beam lab-frame energy tuned to 2.4006 eV (velocity matched condition with 280 keV TiO^+ ion beam). The red curve represents the lab-frame electron beam energy of 3.75 eV (150 meV detuning energy). The black vertical line represents the extent of the electron beam (at expansion 30), i.e. 5.18 mm.

where, the velocity matched condition for the electron beam with respect to the 280 keV TiO^+, termed as the cooling energy $E_{\rm cool}$ = 2.4005 eV. The calculated $E_{\rm lab}$ is the used set value (calculated for the beam-center using $r = 0$ in eqn. 4.12), which for $E_{\rm d}$ = 10 meV, comes out to be 2.7205 eV. Due to the space-charge effect, the electron energy in the center-of-mass frame calculated as a function of the distance from the beam center r has been produced in the figure 4.25. It can be noticed that the electron-ion collision energy increases as one moves out radially and at the edge of the electron beam ($R_{\rm e}$ = 5.18 mm, in our case) reaches $\sim$13 meV, which is an appreciable deviation. Consequently, the velocity spread contributed by the space-charge effect is given as,

$$\vec{v}_{sc}(r) = \sqrt{\frac{2E_{lab}(r)}{m_e}} \tag{4.14}$$

where $E_{\rm lab}$ is calculated according to eqn. 4.12 and the vector has only the longitudinal component as non-zero.

Finally, the velocity contributions as discussed above are redistributed due to the elec-

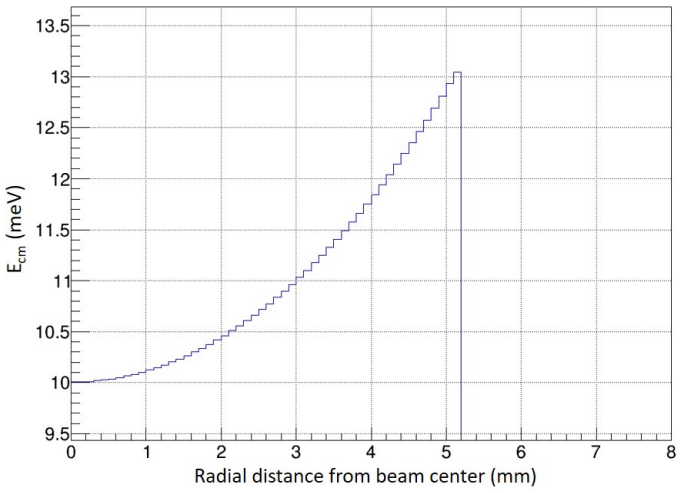

Figure 4.25: The resultant $E_{\rm cm}$ energy curve (Y-axis, in meV) after including the space-charge effect for an electron beam tuned for $E_{\rm d}$ =10 meV with respect to a 280 keV TiO^{+} beam, plotted as a function of the radial distance from the centre of the electron beam, r.

tron beam merging geometry as discussed in the section 2.3. Following a 90° horizontal turn to get it parallel to the ion beam, the electron beam is smoothly bent vertically to merge precisely with former. This causes an off-parallel overlap near the ends of the interaction zone, causing a part of the electron beam to merge with the ions at a non-zero angle, Ω. The merging geometry and the electron beam propagation through the setup was modelled in the work of S. Saurabh [77], the results of which have been used here to input the merging and demerging angles (Ω) of the electron beam as a function of the z-position (see figure 4.26). This leads to a coupling, consistent with our assumptions, in the vertical (X-direction) and the longitudinal (Z-direction) axes, which can be expressed as:

$$\vec{\boldsymbol{v}}_{\boldsymbol{e}} = \begin{pmatrix} \cos\Omega & 0 & -sin\Omega \\ 0 & 1 & 0 \\ sin\Omega & 0 & \cos\Omega \end{pmatrix} \begin{pmatrix} v_x^{(T_\perp)} \\ v_y^{(T_\perp)} \\ (v_{ion} + v_d) + v_z^{(T_\parallel)} + v_{sc} \end{pmatrix}$$

$$\vec{\boldsymbol{v}}_{\boldsymbol{e}} = \begin{pmatrix} v_x^{(T_\perp)} \cos\Omega - (v_{ion} + v_d + v_z^{(T_\parallel)} + v_{sc}) sin\Omega \\ v_y^{(T_\perp)} \\ v_x^{(T_\perp)} sin\Omega + (v_{ion} + v_d + v_z^{(T_\parallel)} + v_{sc}) \cos\Omega \end{pmatrix} \tag{4.15}$$

The result is indicative of the reasoning that the electrons initially have the velocity given by only ($\vec{v}_{\rm ion} + \vec{v}_{\rm d}$) in the longitudinal direction, which due to the merging and demerging geometry causes a coupling with the transverse direction, and thus a vectorial redistribution

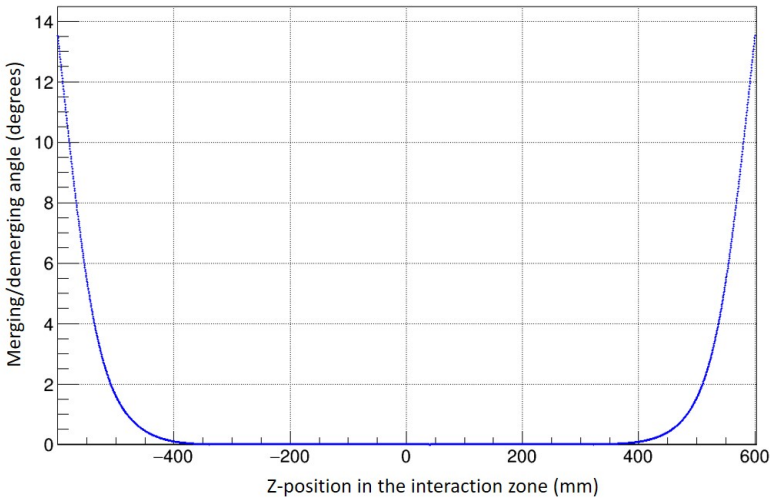

Figure 4.26: Merging and demerging angles, Ω, for the electron beam with respect to the ion beam direction have been depicted on the Y-axis, as a function of the beam position in the interaction region (z-position) on X-axis in mm, where zero marks the centre of the interaction region. Adapted from the results of work by S. Saurabh [77]

occurs.

Consequently, it can be noted that in the collision model, the final result of the MC-simulations leads to a concrete integration of the relevant velocity distribution broadening effects, yielding a final electron velocity distribution as produced in the plot 4.27. This can now be used to calculate the relative velocities for the electron-ion system $\vec{v}_{\mathrm{col}}$, as:

$$\vec{v}_{\mathrm{col}} = \vec{v}_e - \vec{v}_{ion} \tag{4.16}$$

where, $\vec{v}_{\mathrm{e}}$ is given by the eqn. 4.15 and $\vec{v}_{\mathrm{i}}$ = (0, 0, v_{i}). Thus, the collision energies in the electron-ion center-of-mass frame, E_{cm} can be calculated directly as,

$$E_{\mathrm{cm}} = \frac{1}{2}\mu v_{\mathrm{col}}^2 \tag{4.17}$$

which is a fundamental parameter deciding on the product internal states, as well as the resulting KER for the recombination reaction.

4.3.2 Fragmentation model

Delving into the details of collision, it has been observed in the previous DR experiments (see for e.g. [68] for CH^+, [78] for H_3^+) for various molecules that the projected 2D frag-

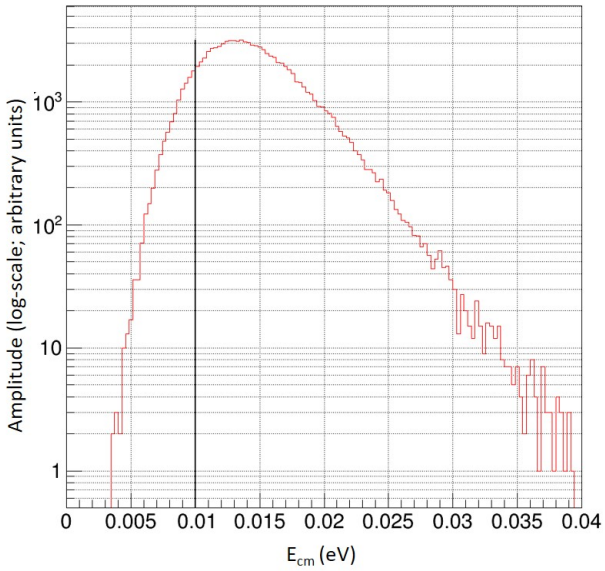

Figure 4.27: The E_{cm} distribution (electron energy in the center-of-mass frame) resulting from the inclusion of realistic conditions at the eCool section for an electron-ion system with TiO^+ beam stored with 280 keV energy, and the electrons tuned for an $E_{\mathrm{d}} = 10$ meV (represented as the black line vertical). Plot generated using Monte-Carlo modelling for 10^5 trials. (X-axis in eV; Y-axis represents log-scale intensity with arbitrary units.)

ment distributions are sensitive to the varying (anisotropic) reaction cross-sections dependent on the angle subtended by the molecular internuclear axis with respect to the electron velocity vector at the time of recombination, θ. We define the reference coordinate system with Z-axis pointing along the (longitudinal) ion beam direction, X-axis as the vertical transverse direction, and Y-axis as the horizontal transverse direction, as depicted in figure 4.29. Although, both the angles defining molecular orientation with respect to the electron velocity vector θ (X-Z plane), and ϕ (X-Y plane) are randomly distributed for the stored beam, ϕ is insensitive in the reaction observables due to the axial symmetry of the electron-ion system in the case of a diatomic molecule for our setup.

To model this θ dependence, along the lines of work by Z. Amitay et al [68], we can define a general angular distribution probability in terms Legendre polynomials as,

$$W(\theta) = \sum_{k=0}^{\infty} a_k P_k(\cos\theta) \tag{4.18}$$

where for the summation until kth order polynomial, normalization is defined as,

$$\frac{1}{4\pi}\int W(\theta)\, d\Omega = a_0 = 1 \tag{4.19}$$

Noteworthy here is that since the fragment distributions are symmetric in the transverse plane (ϕ symmetry), the odd polynomial contributions identically vanish. While the explicit values of weighting coefficients a_k depend intricately on the characteristics of the reaction process, the limits are defined by using the restriction on probability distribution function $W(\theta) \geq 0$. Considering only a weak angular dependence, we can limit our angular distribution contributions at $k = 2$, thus yielding,

$$W(\theta) = 1 + \frac{3a_2}{2}\cos^2(\theta) - \frac{a_2}{2} \tag{4.20}$$

where $a_0 = 1$ has been used from the normalization condition, while the positive probability condition yields $-1 \leq a_2 \leq 2$.

In order to model this using a MC-simulation routine, one first generates a uniform distribution for θ in the interval $[0, \pi)$ over a sphere, which follows a $\sin\theta$-like probability distribution. Following this, the key point is to correctly weigh this with the reaction probability for each angle θ in accordance with the function $W(\theta, a_2)$, for a given anisotropy parameter, a_2 (isotropic case is given by a_2 =2). Thus, an appropriately generated distribution of θ is then fed further into the routine (described below), finally yielding the fragment 2D distance distributions as produced in the figure 4.28. This can be verified with the analytical formula derived for the 2D fragment distance distributions in the work by Z. Amitay et al [68].

Moving a step back, we have defined the appropriate distribution for θ for a particular anisotropy (given by a_2 parameter). This reasoning for this distribution has been discussed before, however, to understand its manifestation in the experimental observables, it is important to note that the physical process of recombination, in general, can be taken to be much more rapid relative to the timescales of particle dynamics. This sets forth a credible assumption that molecule's orientation at the time of recombination, with respect to the z-direction (direction of the beam), angle θ, can be considered to be preserved over the interval of fragments' propagation to the detector. Thus the θ-dependence of a such a recombination reaction can directly be observed in the fragment distance distributions in our setup.

Once dissociated, the energetics of the reaction dictate the KER (see eqn. 4.6). This

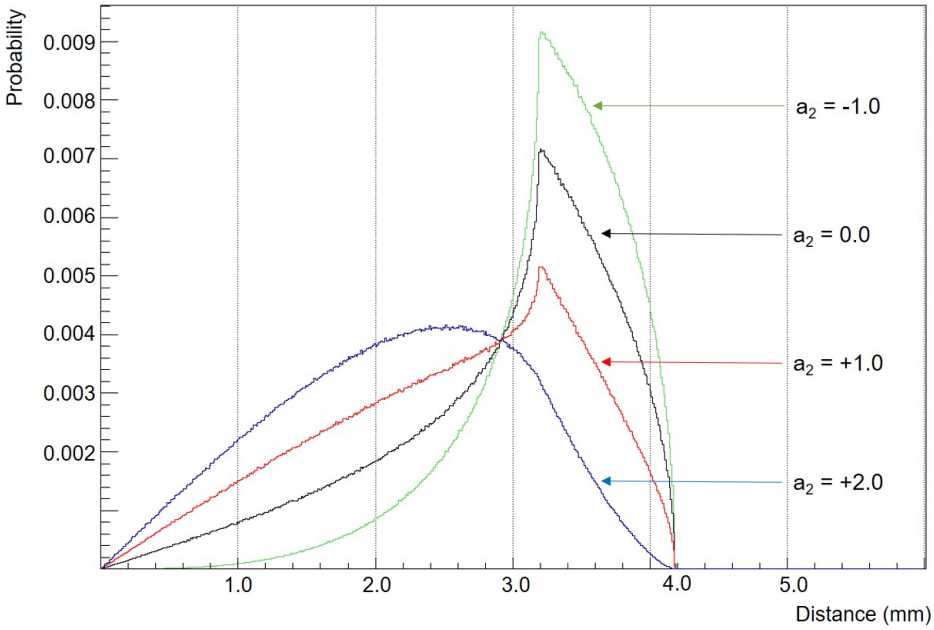

Figure 4.28: MC-modelled shapes of the projected 2D fragment distances for various initial anisotropy dependent on the angle θ at the time of recombination. Anisotropy parameter is given by a_2, introduced as the coefficient of the Legendre polynomial (see eqn. 4.20). Plotted are the MC-modelled distribution for a_2 = -1 (green), 0 (black), 1 (red) and 2 (blue). The distribution has been modelled for TiO^+ DR with an assumed E_{KER} =50.0 meV.

energy is manifested in the relative velocities of the fragments in the center-of-mass frame, following the conservation laws of momentum and energy given as,

$$\vec{v}_{1k} = \begin{pmatrix} v_{1k}\sin\theta\cos\phi \\ v_{1k}\sin\theta\sin\phi \\ v_{1k}\cos\theta \end{pmatrix}, \quad \vec{v}_{2k} = \begin{pmatrix} v_{2k}\sin\theta\cos\phi \\ v_{2k}\sin\theta\sin\phi \\ v_{2k}\cos\theta \end{pmatrix} \tag{4.21}$$

$$\text{where, } v_{1k} = \sqrt{\frac{2\,(E_{KER})m_2}{m_1\,(m_1+m_2)}}; \qquad v_{2k} = \sqrt{\frac{2\,(E_{KER})m_1}{m_2\,(m_1+m_2)}}$$

To transform the fragment velocities to the lab-frame, the initial molecular ion velocity is required, denoted as

$$\vec{v}_{COM} = \begin{pmatrix} 0 \\ 0 \\ v_{ion} \end{pmatrix} \tag{4.22}$$

where v_{i} has been defined in eqn. 4.8. This can then be added vectorially to the center-of-mass velocity vectors for the particles to yield the lab-frame velocities $\vec{v}_1$ and $\vec{v}_2$, for the recombination reaction with a kinetic energy release of E_{KER}:

$$\vec{\boldsymbol{v}}_{\mathbf{1}} = \begin{pmatrix} v_{1k}\sin\theta\cos\phi \\ v_{1k}\sin\theta\sin\phi \\ v_{ion} + v_{1k}\cos\theta \end{pmatrix}, \quad \vec{\boldsymbol{v}}_{\mathbf{2}} = \begin{pmatrix} v_{2k}\sin\theta\cos\phi \\ v_{2k}\sin\theta\sin\phi \\ v_{ion} - v_{2k}\cos\theta \end{pmatrix} \tag{4.23}$$

where m_1 and m_2 are the masses of the individual product fragments, and U_{acc} is the initial ion energy in the ring. The fragment velocity schematic for a situation with ϕ =0° has been presented in the figure 4.29.

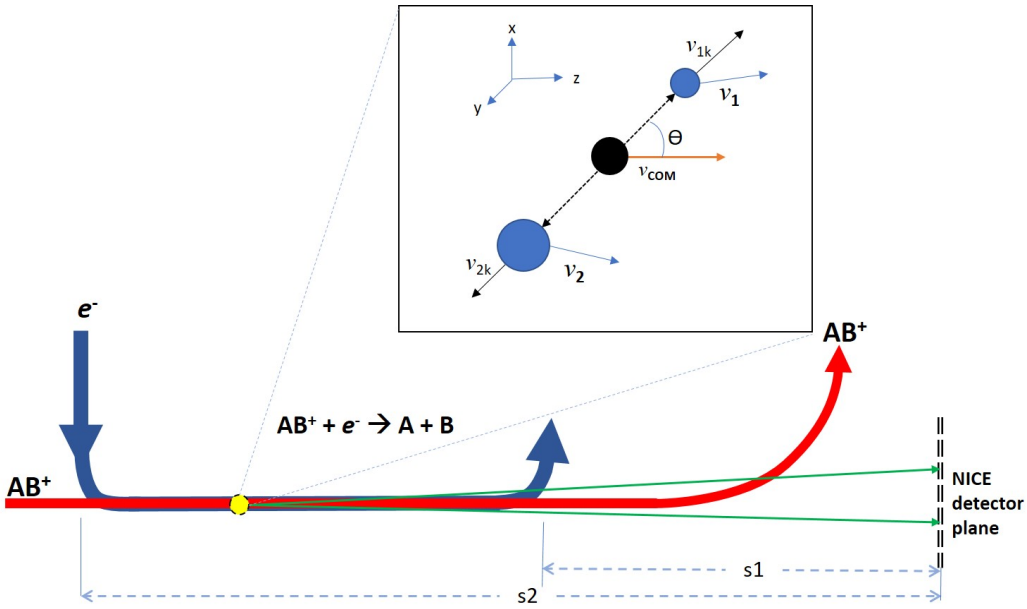

Figure 4.29: Schematic for an electron-ion recombination at the eCool followed by dissociation to neutral fragments.

4.3.3 Detection Model

Following the collision, dissociation, and KER, the final step in the model takes into account the fragment propagation to the detector, and the detector characteristics that may affect the recorded data. This puts in place the vitality of detector dimensions, which, in our case, is an MCP surface with a sensitive circular area with 120 mm diameter. If high KER is expected from the reaction and/or the fragments masses differ by a large factor, the transverse distances expected are high. This may lead to one of the fragments land-

ing outside the detector surface, and thus, affecting the detection efficiency for the events. However, in present case of Ti and O fragments, the fragment masses are in the ratio $\sim$3, and the KER expected is $<$ 200 meV, thus making the current measurements independent of this limitation.

Chapter 5

Endothermicity Analysis

The ideas and results developed in the earlier chapters encapsulate the rationale, experimental techniques, measurement conditions and schemes, and the essential filtering and calibration required to visualise the obtained data. Moving forth, in this chapter we intend to use these discussions to investigate and interpret the acquired data, using various methods and filters on the multi-dimensional data structure, and produce the interim results from the undertaken analysis.

According to the molecular characteristics and level structure for TiO^+ discussed in chapter 1, while the distinct electronic states of the molecule exhibit considerable energy separation (of a few eV– except for the fine-structure doublet splitting of the ground level), the rovibrational excitations make the energy ladder for the molecule increasingly dense near the ground level. This imbues a wide energetic dispersion in various modes of the ion, significantly dependent on the ion's source temperature, dipole moment, and the residual radiation in the CSR, as the molecular ion is allowed to radiatively cool in the CSR (see sec. 3.3). In contrast, while the atomic product species resulting from a binary DR do not possess a rovibrational structure, the high density of electronic states of titanium and oxygen close to the ground level furnish a plethora of exit channel possibilities for the reaction. To understand the energetics of the DR for TiO^+ molecular ion, it is imperative to account for all such possibilities within the relevant collision energies that our experiment probes into.

As has been mentioned previously, one of the distinctive aspects of the particular molecular reaction under investigation is the hypothesized endothermic energetics of the reaction [11, 15, 19]. Further in this work we use the term 'endothermicity' to refer to the reaction energetics, which construes the hypothesis – the minimum possible initial energy level of the molecule is assumed to be lower in energy than the minimum possible final product energy level, and also fixes a sign convention for the discussion (see eqn. 1.4). The idea,

in a graphical schematic, would translate to a relative shift between the ground electronic level of the TiO^+ molecular ion, and the cumulative ground energy level of Ti and O atomic species, as has been shown in the figure 1.4, wherein ΔE actualizes the aforementioned endothermicity. A relative shift of the molecular energy level ladder's zero- point below the products' is interpreted as a positive endothermicity. This endothermicity value can be pinned down using the measurements made as a part of the current work, the systematic progression of which forms the subject matter of this chapter. In this context, the measured data, as described in section 4.2, can be used to probe into different regimes of the initial rovibrational excitation distribution of the molecular ion using various ion storage times in the CSR before performing the recombination measurement (see sec. 3.3 and sec. 2.7). Further, for each storage time, measurements conducted for different collision energies for the electron-ion system presents an opportunity to probe into the effects of varying plausibility of accessible product channels with changing detuning energies, also allowing for an understanding of the reaction pathways possible for the DR.

5.1 Interpreting the fragment distance distributions

The fundamental idea for deducing the aimed reaction endothermicity rests within a detailed interpretation of the obtained 2D fragment distance distribution (FDD) data recorded from the imaging measurements (as produced in sec. 4.2). The discussions followed in section 4.3 highlight the cardinal characteristics for the behaviour of resulting statistical fragment distances and the distribution thereof from the cumulation of fragmentation events occurring within the interaction region (at distance D away from the detector plane), accompanied by an energy release E_{KER}, being the crucially deciding experimental variables, as made clear in eqn. 4.7. It is also to be noted that since the length of the interaction region is fixed and the molecule orientation θ is randomized uniformly, this implies that the 2D FDD obtained on the NICE detector has a direct one-to-one correlation with the E_{KER}.

As discussed in section 4.3, the kinetic energy release is given by the expression 4.6, wherein we have also worked on understanding the contribution by E_{cm} using the Monte-Carlo modelling of various realistic effects dependent on the setup details. This crucial conversion from the E_{d} ($= m_e v_{\mathrm{d}}^2/2$) to E_{cm} ($= m_e v_{\mathrm{col}}^2/2$) is explicitly given by the relation for the respective velocities as in equations 4.15 and 4.16. The effect of second contribution arising from the molecular and atomic electronic structure of the reactant and product species $E_{i,f}$ has been explored briefly in section 1.2 (also see table 1.3). It is to be remarked here that for the energy ranges considered in our experiment (< 200 meV),

the relevant initial energy levels for the molecule are only the $X^2\Delta$ doublet levels, and the pertinent final exit channels combinations in the same range for product fragments have been listed in the table 5.1 (with reference to table 1.2). This has to be further corrected for by including the rotational level structure, as described in section 3.3. Once these ingredients have been pertinently accounted for, what remains is the final piece of the puzzle, namely the endothermicity ΔE (see eqn. 1.3). On including all such contributions appropriately, the aforementioned Monte-Carlo model should be able to produce an expected 2D distance distribution via simulation, which should congruently match (within statistical error bars) with the recorded data for a specific value of endothermicity for various measurements recorded for different detuning energies, E_{d}, finally yielding an estimate for the target physical quantity, viz. ΔE. It is important to understand that with each step towards higher detuning energies, the initial energy of the system from where the reaction proceeds, increases. This gives way for the possibility that the reaction can traverse along different potential energy curves to reach an exit channel. This energy finally manifests as the internal excitation of the products or as the kinetic energy release (KER). Given a complete set of initial and final energy states, the KER can be deduced accordingly. Ideally, if all the product channels were equally probable, in other words, if the reaction cross-section was the same for all reaction pathways to various products, the interpretation of the endothermicity would be rather straightforward. As a given KER produces a characteristic FDD curve, with the assumption that all energetically plausible channels participate in the reaction equally, a composite representation of all these curves can be generated and used to compare with the obtained data.

To implement this idea for pinning down the endothermicity, we undertake the analysis in two steps to pragmatically approach the required precision. It has been mentioned (see eqn. 1.1) that the current estimates for the quantity, as in the literature, are $\Delta E = 50 \pm 70$ meV, yielding an error bar as high as the expected value. To coarsely narrow this interval down, we use the first method of level stick-diagram visualization (see sec. 5.2). Further, within this smaller interval we undertake a more elaborate search by explicitly fitting the 2D FDDs generated using the MC-simulation routine, and quantify the goodness of this fit by using a χ^2 parameter which has been discussed in section 5.3.

5.2 Level stick-diagram visualization

For implementing the first method to understand the recorded data, we use an analysis routine along the lines as mentioned further. It is to be noted that the logical sequence of the

Fragment exit channels for Ti and O			
State Index	O-state (index)	Ti-state (index)	Energy above ground [meV]
0	$^3P_2$ (0)	a^3F_2 (0)	0.0
1	$^3P_1$ (1)	a^3F_2 (0)	19.6
2	$^3P_2$ (0)	a^3F_3 (1)	21.0
3	$^3P_0$ (2)	a^3F_2 (0)	28.1
4	$^3P_1$ (1)	a^3F_3 (1)	40.6
5	$^3P_2$ (0)	a^3F_4 (2)	48.0
6	$^3P_0$ (2)	a^3F_3 (1)	49.1
7	$^3P_1$ (1)	a^3F_4 (2)	67.6
8	$^3P_0$ (2)	a^3F_4 (2)	76.1

Table 5.1: A complete list of relevant exit channels combinations for the product Ti and O fragments from the TiO^+ dissociative recombination with electron within the energy ranges of < 200 meV as probed in the current work, along with the cumulative energies above the ground level listed in meV in increasing order. The Ti and O states have been depicted in the conventional atomic state notation, with the state index according to the table 1.2 listed within parentheses for reference.

steps involved is similar for various detuning energies and storage times involved (unless mentioned otherwise), and thus we only discuss one such case in detail for instantiation.

We consider the data recorded for measurement interval between $\sim$500 - 600 seconds for illustration of the routine, wherein measurements for eight separate detuning energies have been made, corresponding to $E_{\rm d}$= 0, 10, 20, 30, 40, 60, 90, 120 and 150 meV. Here, we assume that all the initial states denoted using $\Omega = (\Lambda + \Sigma)$– angular momentum quantum number (Λ being quantum number for the total orbital angular momentum of the electrons, and Σ the projection of spin angular momentum S of the same about the internuclear axis), J– rotational level quantum number, v– vibrational level quantum number, have equal cross-sections, irrespective of the specific product state. Hereby, we use the radiative cooling model (described in sec. 3.3) to estimate the rotational population distribution of TiO^+ between the considered time interval for measurement (molecule is expected to be in the vibrational ground state after < 1 sec). Such a distribution averaged for $500-600$ seconds time interval after the ion beam injection in the CSR has been produced in figure 5.1. The produced plot, for each $(\Lambda + \Sigma)$ bunch independently, has been normalised to the population fraction of the maximally populated rotational state. The modelled results

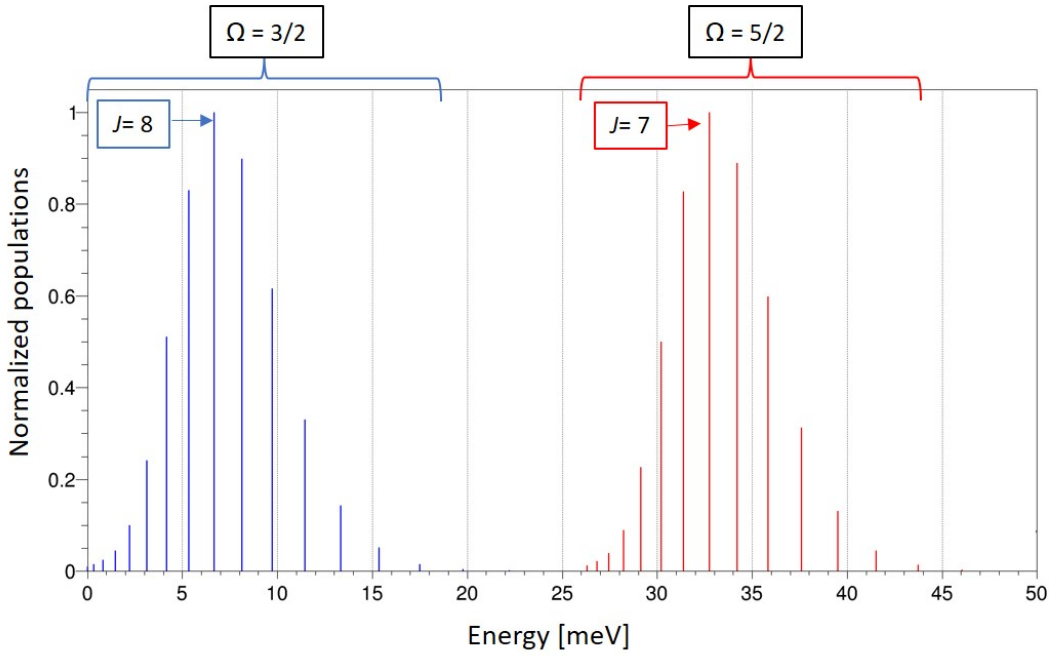

Figure 5.1: Rotational state population distribution plotted with respect to the TiO^+ ground state level (in meV) for the fine-structure split states, $\Omega = \Lambda + \Sigma = 5/2$ (red) and $\Omega = 3/2$ (blue). Each $\Omega-$cluster is normalized to the highest level population, which for $\Omega = 3/2$ is J =8, while for $\Omega = 5/2$ is J =7 averaged for 500−600 seconds interval in the CSR. Model assumes molecular dipole moment of 6.3 D with the initial source temperature of ∼1100 K.

suggest that after ∼500 seconds of ion storage in the ring, the molecules are still expected to have rotational excitations up to $J = 14$ level occupying a dominant fraction of the total population. Thus, we expect that the KER contributions arise from the multiple rotationally excited levels populated at the given time, as opposed to a single ground energy level.

Once the population distributions and level energies are known, the E_{KER} can be calculated as:

$$E_{\mathrm{KER}} = E_i + E_{\mathrm{d}} - E_f - \Delta E \tag{5.1}$$

where E_i encapsulates both the electronic and rotational energy contributions, E_{d} is the set electron detuning energy, E_f is the energy of the product fragments in their respective internal states, and ΔE is the assumed endothermicity for the iteration. It is remarked here that in this method we do not invoke the energy contributions introduced due to electron energy spread, which are typically on the order of a few meV.

Further, we note that following from previous discussions it is known that a specific

KER in the reaction with known fragment masses produces a characteristic FDD curve with a peaking feature, and it can be modelled well. This peaking feature, as shown in the figure 5.2, is the feature with highest probability/intensity, related uniquely to a KER for a given system by the following relation:

$$d_{\mathrm{rep}}(E_{\mathrm{KER}}) = D_{min}\frac{(m_{\mathrm{Ti}}+m_{\mathrm{O}})}{\sqrt{m_{\mathrm{Ti}}m_{\mathrm{O}}}}\sqrt{\frac{E_{\mathrm{KER}}}{U_{\mathrm{acc}}}} \tag{5.2}$$

here, d_{rep}, the representative distance for a given KER (E_{KER}) is the most probable 2D distance between fragments of mass m_{Ti} and m_{O} following break-up, obtained when the D_{min} is used, while the initial energy of the stored ion beam in the ring is given by U_{acc}. This has been represented as a dashed line in the figure 5.2.

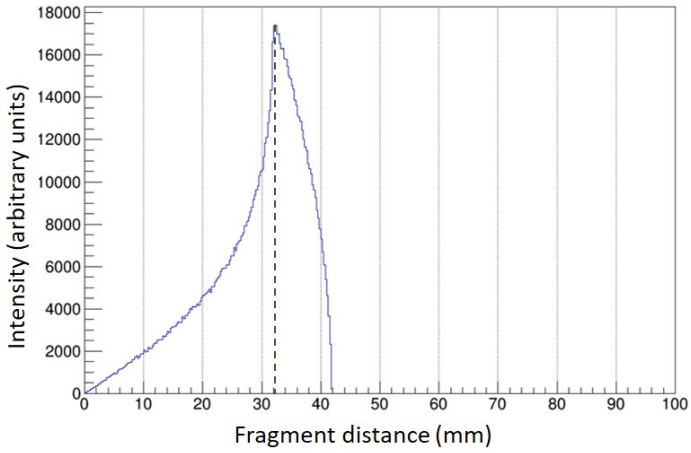

Figure 5.2: The 2D FDD as seen on the NICE detector for a kinetic energy release of 5.0 eV manifested in Ti and O fragments. The dashed line marks the highest intensity feature at a distance d_{rep} for the distribution used as a KER's one-to-one representation on the distance curve.

Putting this together– for a specific measurement run with defined E_{d}, we use the E_{KER} calculation (eqn. 5.1) to deduce the energetically plausible channels at a particular ΔE, and plot the corresponding representative 2D fragment distance peaks at $d_{\mathrm{rep}}(E_{\mathrm{KER}})$ for each. This has to be carried out for various possible values of endothermicity, such that a sensible conclusion can be made based on the first principles, keeping in view the assumptions used for the method– mainly the fact that the resulting E_{KER} at this stage does not include the energy contribution due to electron energy spread, and that the recombination reaction may follow anisotropic probability, which may also change the shape and thus slightly shift the peak feature of the FDD (see fig. 4.28). Further, this can be repeated for different

$E_{\rm d}$ measurements, each of which yield a distinct FDD, as has been produced in 4.2. A cumulation of these investigations has been used to deduce a narrower range plausible for the physical quantity ΔE. Few noteworthy points arising from the procedure giving a clearer understanding of the behaviour of changing endothermicity value are:

- For a given set of conditions, on only changing the ΔE value, the resulting $d_{\rm rep}$ moves according to a square-root energy dependence (see eqn. 5.2). For an increase in assumed endothermicity, the distance lines shift towards lower distances, or to the left of the plot relatively. This is due to a decrease in the $E_{\rm KER}$ (see eqn. 5.1), leading to a smaller velocity imparted to the fragments, and thus a smaller distance traversed on average over a similar time-of-flight. The opposite can be deduced for a change towards a smaller ΔE value, wherein the distance lines shift towards higher distances.

- The resulting distance lines are present such that the first appearing lines (having the highest KER) stem from the excited doublet state Ω = 5/2 of the TiO^+ molecule being the initial state. Naturally, the first lines arising from the initial state as the ground state (corresponding to Ω = 3/2) of the molecule is separated by $\sim$ 26 meV in energy, given by the fine-structure splitting. The intermediate plausible channel/line distribution is dictated by the separation of rotational energy levels and the difference between further electronic states.

- Using the expression 5.1 it can be noted that $(E_{\rm i} - E_{\rm f})$ is strictly dependent on the states of the molecular and atomic species involved, thus, is a constant over the various iterations conducted here. The variable quantity, $(E_{\rm d} - \Delta E)$ is the defining parameter for the outcome in each case.

- Following from the remarks above, and reviewing the FDD patterns obtained by measurements, we can converge on an upper limit for the plausible endothermicity values by investigating behaviour of the distance lines $d_{\rm rep}$ with the lowest $E_{\rm d}$ data available. However, following from the discussion in the sec. 4.2.3, the 0 eV data has only feeble characteristics spilling in the sensitive zone of $>$1.6 mm, thus we use the lowest non-zero $E_{\rm d}$ available, i.e. for 10 meV in our case (see fig. 5.3), which has a sharper feature coming into view at $\sim$ 2.0 mm. The rationale being that even the maximum endothermicity value must inevitably allow for the highest rotational population line (corresponding to J = 7, for Ω = 5/2, see fig. 5.1) to be an energetically plausible channel ($E_{\rm KER} > 0$), also on the other hand ensuring that

the first distance line in the bunch appears within the sensitive imaging range for the plot. This threshold condition is fairly conservative, and is achieved at a value of $\Delta E \approx 42.72$ meV for $E_{\rm d} = 10$ meV, thus prompting the definition an upper bound for possible endothermicity as: $\boldsymbol{\Delta E < 43}$ **meV**.

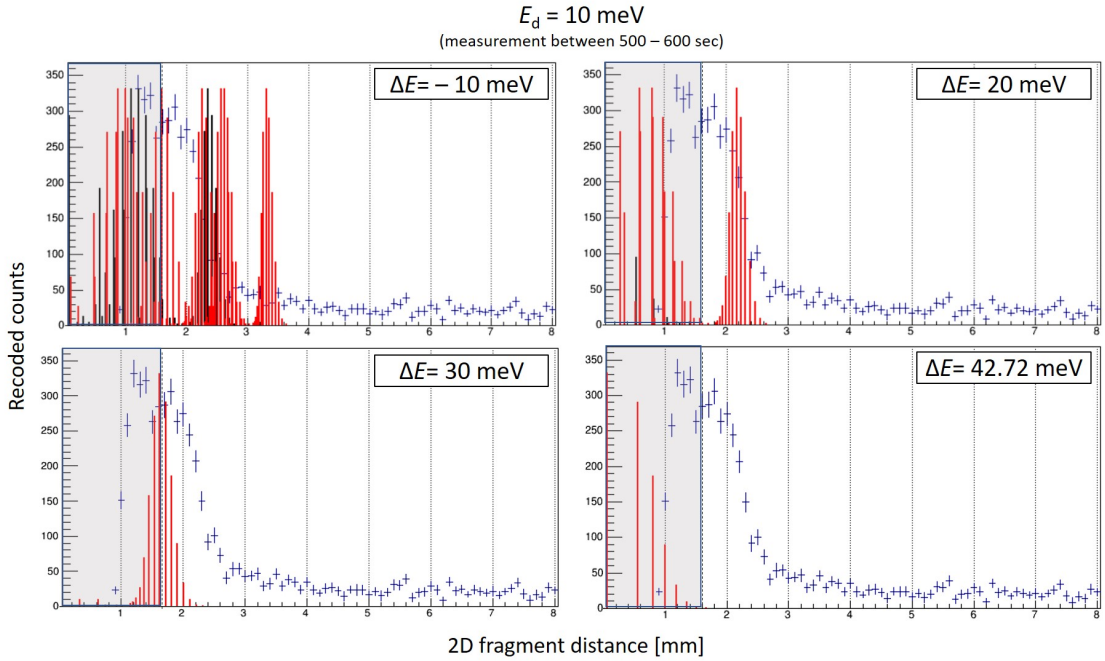

Figure 5.3: Level-stick diagram plots for $E_{\rm d} = 10$ meV data recorded between 500−600 sec, for endothermicities $\Delta E = -10$, 20, 30 and 42.72 meV. The dashed vertical black line defines the sensitive imaging limit of 1.6 mm, the data to the right of which is credible and thus used for analysis. The figures present an intuitive representation for the behaviour of FDD patterns as the endothermicity is changed, and depicts the two extremes of the first limits deduced on the possible endothermicity for the target reaction.

- To deduce the lower endothermicity limit for our further investigation, we note that the dominant features in the FDDs recorded for high detuning energies, viz. $E_{\rm d} = 120$ and 150 meV are present as finite bunches at distances ~ 3.8 and 4.6 mm respectively, with clear rising and falling slopes (as in fig. 5.3). This implies that there are plausible channels opening initially (with increasing slope), but after a certain ΔE there are no new channels opening (see table 5.1), thus the slope decreases. This indicates that the endothermicity cannot be lower than a threshold value which can be deduced by understanding that the last possible channel in the level-sick diagram should at least account for the peaking feature in the experimentally obtained FDD, which is a highly conservative estimate. This condition is arrived at for ΔE = -

10 meV, as can be noticed in the figure 5.4. It is also remarked that there exist no channels with lower KER than the ones indicated in the plot and is not an approximation, thus prompting the justification for aforementioned reasoning. This can also be subtly backed by the idea that for the recorded data of lowest $E_{\mathrm{d}} = 10$ meV probed, wherein the dominant feature in the spectrum appears at $\sim$2.0 mm, should be aligned with the first channel opened for the recombination arising from the ground electronic state of TiO^{+} (fine-structure state $\Omega = 3/2$)– a fairly conservative limit. This results in, and substantiates, our deduction for the lower limit allowed for endothermicity as $\boldsymbol{\Delta E > -10.0}$ **meV**, where the 'negative endothermicity' includes the possibility that the reaction may be exothermic.

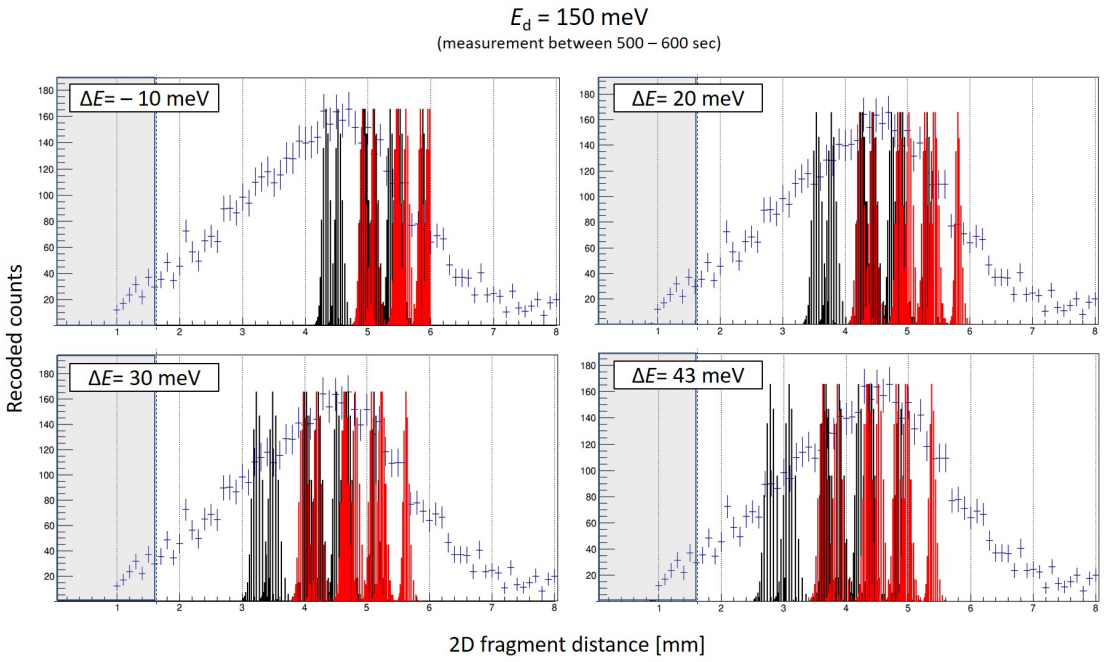

Figure 5.4: Level-stick diagram plots for $E_{\mathrm{d}} = 150$ meV data recorded between 500−600 sec, for endothermicities $\Delta E = -10$, 20, 30 and 43 meV. The plots depict a general behaviour of changing endothermicity for high E_{d} values, wherein the d_{rep} (distance lines) shift as the relevant parameters are varied.

This visualization method has been used to develop fundamental ideas to move forth towards a detailed analysis of the recorded data for various storage time intervals and detuning energies. The proposed range of feasible endothermicity for the targeted reaction, $\boldsymbol{-10\ \mathrm{meV} < \Delta E < 43\ \mathrm{meV}}$ has been further explored by the elaborate method of fitting the 2D distance distributions to the recorded data, as has been discussed in the following section.

5.3 2D distance distribution fitting

Moving further onto a detailed investigation, we use the method of fitting a composite of simulated 2D FDDs using the Monte-Carlo modelling as elucidated in the section 4.3. The routine has already been shown to include the details defining a realistic depiction of the electron energy distribution ensued as a result of the prevalent conditions at the experimental setup and the application of optimisation techniques. The procedure to implement this method involves a step-wise transition to a composite 2D FDD following along a logical resumption from the ideas developed for the level stick-diagram visualisation technique, wherein for a given set of $E_{\rm d}$ and ΔE the energetically feasible channels have been calculated. Following on, we note that there are only two distinct possible initial electronic states for TiO^+ in the reaction (i.e. the fine-structure ground states, denoted henceforth by $\Omega =$ 3/2 and $\Omega =$ 5/2), whereas a total of nine electronic state combinations are possible for the products, as have been listed in the table 5.1. All possible combinations of initial and final states correspond to a possible reaction channel. We use the notation *(initial, final)* to address a particular reaction channel, wherein *initial* is one of the two Ω values representing the initial molecular electronic state, while *final* stands for the state index (as in table 5.1) for the particular product state combination being referred to. It is also remarked that each channel corresponds to a 'bunch' of possible $E_{\rm KER}$ as elucidated in figure 5.1 due to the rotational state distribution available for the initial molecular state. For the analysis thus, we generate expected FDD curves for each of the channels for the given set of $E_{\rm d}$ and ΔE under consideration. Following this, these curves are fitted to the experimentally obtained FDD curves as produced in section 4.2.3 using an appropriately customised Chi-square (χ^2) parameter optimising fit algorithm available as a part of the ROOT-data analysis framework by CERN. This has been described in the following sections.

5.3.1 Generating composite FDDs

With a fair model of the incoming electron beam at hand, we move further to incorporate the conditions of the ion beam and the consequent electron-ion recombination followed by dissociation to neutral fragments and the recorded signal at the detector, to simulate a cumulative distance distribution corresponding to each $E_{\rm KER}$ possible according to the energetically feasible channels. This is then used to produce a composite FDD curve for specific parameters for the aimed distribution.

The routine commences with the input of $E_{\rm d}$ and ΔE parameters, following the calcu-

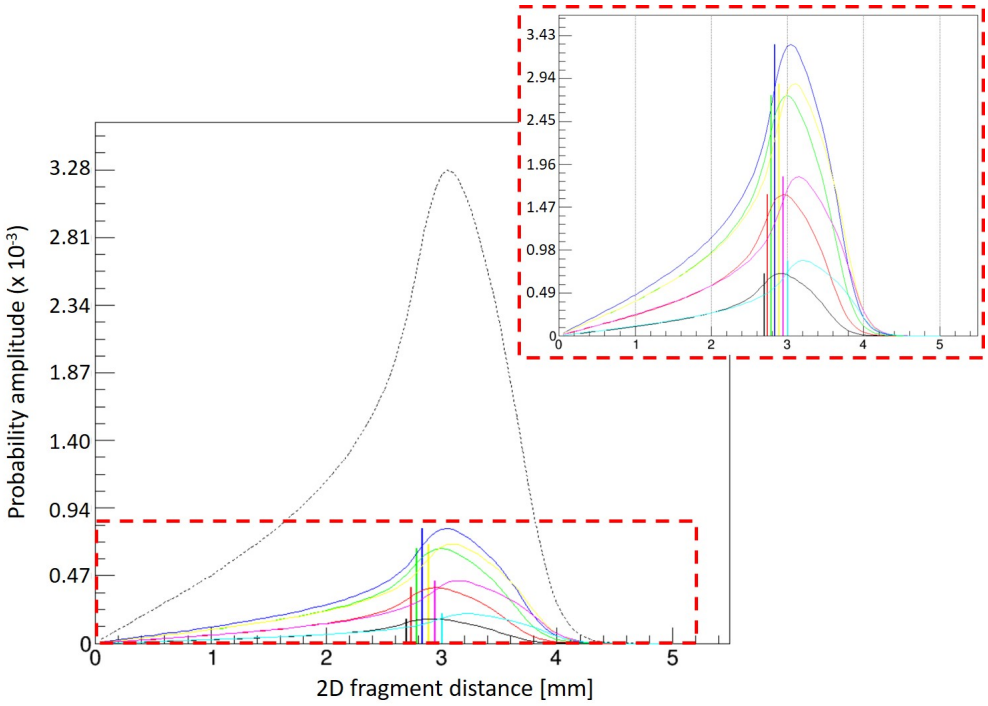

Figure 5.5: The simulated 2D FDD obtained by the KERs resulting from first channel, i.e. (5/2, 0), for $E_{\mathrm{d}} = 10$ meV and $\Delta E = 4$ meV. The dominantly populated and energetically feasible rotational levels yield KERs represented by coloured vertical distance lines at d_{rep}, with corresponding FDD curves simulated including the realistic electron energy spread plotted as solid coloured curves (see inset; Y-axis has been readjusted to account for the smaller number of total MC-iterations run for each sub-curve). Note that electron energy spread adds $\sim$3 meV on average to the KER deduced from the eqn. 5.1, shifting the distribution peak away from the corresponding d_{rep}. The dotted black curve represents the resultant cumulative single-channel FDD curve obtained from the addition of the constituent fragment distributions.

lation of the E_{KER} according to eqn. 5.1 for all of the 18 possible channels. This generates an ordered list of discrete possible kinetic energy releases. It is important to note again that each channel consists of a 'bunch' of kinetic energy releases, depending on the rotational energy level separations, with the information about relative rotational state population fractions as discussed previously. Such bunch within each channel is treated concurrently as a whole by the functions discussed further. We remark that here we only use the FDD simulations for isotropic case initially, i.e. $a_2 = 0$, as mentioned in the MC-modelling (see sec. 4.3). The list of kinetic energy releases thus obtained, is then passed to the MC-simulation routine, one channel at a time, wherein the electron energy distributions are generated using the detailed experimental considerations mentioned in section 4.3, includ-

ing the space-charge effects, finite electron beam temperature and the effects arising from the merged beam geometry. The routine also includes an ion beam size filter, detector size filter, and other relevant details to account for the realistic conditions in the performed experiment. Further, this electron energy distribution is effectively convolved with each KER, and a realistic 2D FDD is produced for the complete bunch but adding up individual contributions from each rotational line within a channel, with the distance contributions in the cumulative also weighted by the rotational population fractions. This has been depicted in figure 5.5, wherein the KER resulting from first channel, i.e. (5/2, 0) for $E_{\mathrm{d}} = 10$ meV and $\Delta E = 4$ meV, has been used and the d_{rep} along with full 2D FDDs have been produced. It is important to note that the electron energy spread adds ~ 3 meV on average to the kinetic energy releases deduced from the eqn. 5.1, which shifts the actual peak for the distance distributions further away from the corresponding d_{rep}.

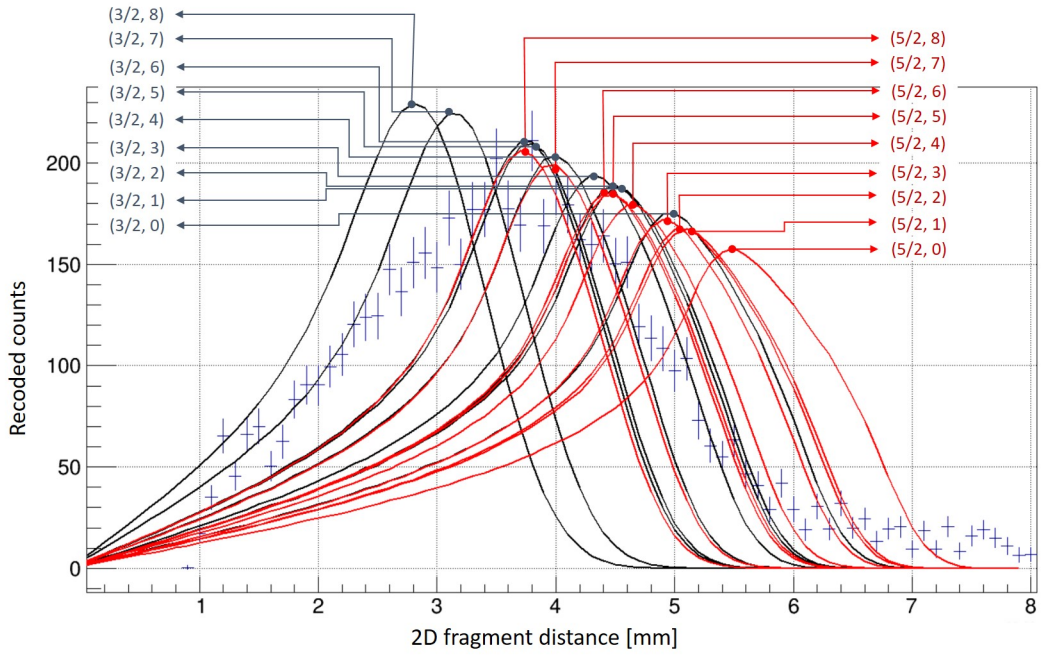

Figure 5.6: A composite curve for simulated 2D FDD produced for all open channels for $E_{\mathrm{d}} = 120$ meV and $\Delta E = 17$ meV. The red curves represent the channels with $\Omega = 5/2$ as the initial state, while black curves stem from $\Omega = 3/2$. Note that resulting FDDs are spaced extremely closely due to proximal values for E_{KER} which complicates the process of making inferences regarding the goodness of attempted fit.

Using this descriptive picture for the resulting 2D FDD from one channel, the idea can be extrapolated to use the same approach iteratively for multiple channels for a given set of E_{d} and ΔE parameters, leading to a composite curve. An instantiation of this has been

produced in figure 5.6, wherein all the open channels for $E_{\mathrm{d}} = 120$ meV and $\Delta E = 17$ meV have been plotted. The area under each curve is the same, owing to the normalisation sustained by using equal number of MC-simulation trials for recombination events. However, it is noteworthy that the FDD curves for some channels are spaced extremely closely due to the small difference in energies. This, in the automated fitting routine yields results such that for a closely spaced set of channels, the fit only accounts for one, while the others are identically given zero weight. To surmount this, acknowledging the lack of understanding about the reaction pathways at this stage, we use a systematic *channel grouping*. In the routine, this is implemented by using the generated 2D FDDs for each channel separately according to the aforementioned procedure, and cumulating the probability amplitudes for the proximal channels together in a single grouped-channel. We define the proximal channels as ones which have their energies within a vicinity of $\pm$ 0.1 meV from a center/average point in between. The inferred channel groups as a consequence have been listed in the table 5.2 and depicted for a representative stick-diagram plot of $E_{\mathrm{d}} = 120$ meV and $\Delta E = 17$ meV in figure 5.7. Given that the 2D FDD curve is essentially a probability amplitude representation along the Y-axis, it is helpful to note that the channel grouping procedure fundamentally divides the total probability equally among its constituents (due to normalised areas for each), and conserves the total span of the curves in the distance dimension– this is important for further steps of the procedure.

5.3.2 Contaminant ion background modelling

In order to delve further in to the analysis, it is important to note the significant details existent in the recorded data as produced in the section 4.2. One of the major characteristics, consistently present in the data is a faint background at $\sim 5\%$ (with respect to the maximum counts for the used binning) for most measurements, and ranging up to $\sim 12\%$ for few measurements with low statistics. For instantiation, figure 5.8 depicts the FDD recorded for $E_{\mathrm{d}} = 0$ eV, measured after between $500-600$ sec after ion beam injection in the CSR, showing statistics recorded for fragment distances upto 50 mm. As discussed previously in section 4.2.2, the residual-gas background has been dealt with appropriately using the run parameters and recorded data for electron-beam off conditions. This accounted for the c_{d} and c_{bg} contributions to the background, as indicated in equation 4.5. This correction has already been accounted for in the plotted curves produced in section 4.2.3. In figure 5.8, the total count statistics acquired (without any subtraction) has been shown in blue, while the residual-gas background has been plotted in red on the same can-

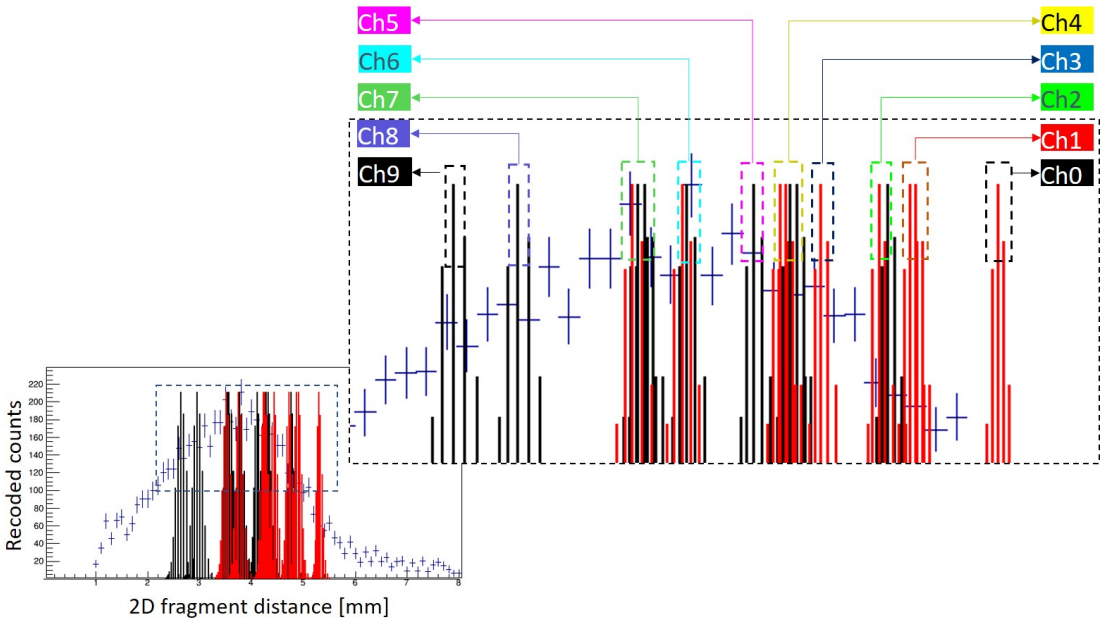

Figure 5.7: A representative stick-diagram plot for $E_{\mathrm{d}} = 120$ meV and $\Delta E = 17$ meV elucidating the channel grouping undertaken to optimise the fitting routine and data interpretation. Channels have been grouped on the basis of energy proximity wherein the channels within $\pm$ 0.1 meV of each other (measured from a central/averaged point in between) have been grouped (also see table 5.2). The grouped channels have been indicated here in the 2D FDD plot, with characteristic colours used further in the work.

vas. Here we remark that the fragment distance statistics observed at $\sim$20 mm result from KER close to $\sim$2 eV, a considerably high value which even after detailed investigations into the realistic effects and experimental error bars does not correspond to any possibility arising from our target molecule TiO^+. This validates our assumption that the aforementioned fragment distributions correspond to another species, and delving further it can be noticed that the background counts unaccounted for by the residual-gas collisions largely has two types based on trends: the decaying background from $3-25$ mm with significant amplitude (henceforth referred to as '*type-a*') and a low constant background from $25-50$ ('*type-b*'). Here, we primarily aim to understand the *type-a* which is prevalent in the area of our analytical interest, i.e. at low distances (< 8 mm); presumably a persistent background contribution c_{ci}, expected to arise from the recombination of contaminant ions present in the injected beam, with the electrons.

The composition of the produced ion beam used for the experiment has been discussed in section 3.1, which indicated an approximate 10% contribution by the $TiOH^+$ (with ^{47}Ti) ion species owing to the selection based on similar magnetic rigidity as the target ion TiO^+

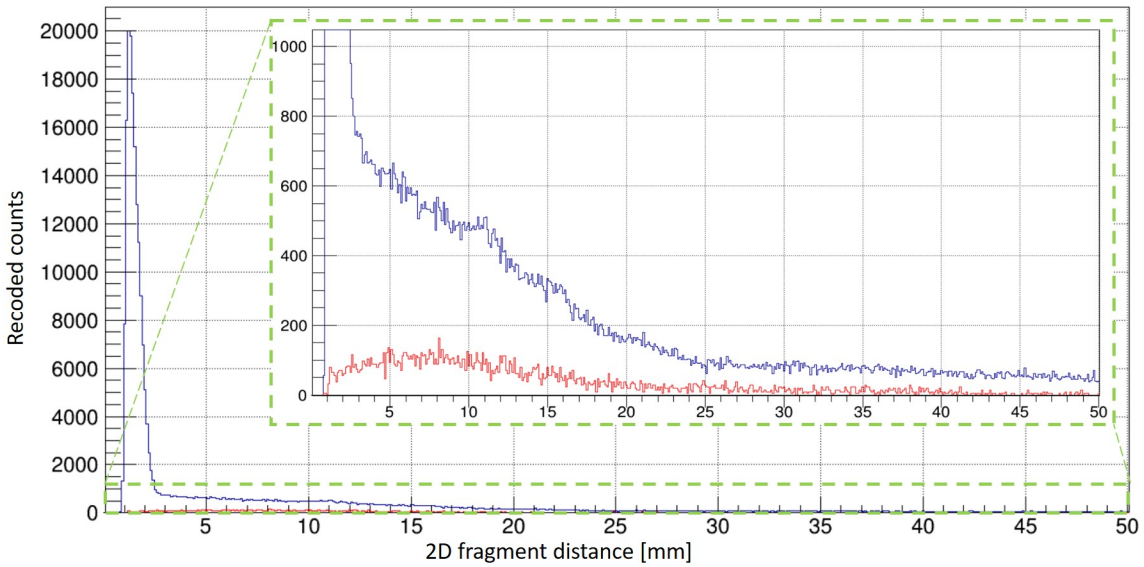

Figure 5.8: The FDD recorded for $E_{\mathrm{d}} = 0$ eV, measured between 500−600 sec after ion beam injection in the CSR, showing statistics recorded for fragment distances upto 50 mm. The total count statistics acquired (without any subtraction) have been shown in blue, while the residual-gas background has been plotted in red. The inset shows a zoomed view of the low count range wherein noticeable is background unaccounted for by the residual-gas collisions (red) which largely shows two trends: the decaying background from 3−25 mm with significant amplitude (referred to as '*type-a*') and a low nearly constant background from 25−50 mm ('*type-b*').

(with ^{48}Ti), i.e. m/q= 64 u/e. To delve deeper into this, we intend to understand the possible contributions from the $TiOH^+$ system in conjunction with the observed background. Noting that the triatomic molecule can fragment in three ways, i.e. (Ti + OH), (TiO + H), and (Ti + O + H), which are chemically most probable. Using a filter to separate 3-body events in the acquired data, we only find $< 1\%$ statistics, which is too low to account for the observed background, also supported by the fact that the required reaction pathway is endothermic by ∼2.3 eV (using data from [79]), ruling out the third possibility. The other two possibilities can be listed as follows,

$$\mathrm{TiOH^+} + e^- \longrightarrow \mathrm{Ti} + \mathrm{OH^\star} + 2.1\,\mathrm{eV} \tag{5.3}$$

$$\mathrm{TiOH^+} + e^- \longrightarrow \mathrm{TiO^\star} + \mathrm{H} + 4.5\,\mathrm{eV} \tag{5.4}$$

where we have used the relevant experimental values from [19], [79] and [80]. The second reaction 5.4 is calculated to be considerably exothermic, with a high difference in the fragment masses, implying that the resulting fragment distances are expected to be partaking

majorly in the *type-b* background, and thus we do not discuss this here for brevity. The reaction equation 5.3 depicts the break-up into Ti and OH fragments, where OH molecule may be present in rovibrationally excited states, while only the ground electronic state $(X^2\Pi)$ is accessible within the relevant energy range for the same. This implies that the reaction energy of 2.1 eV can also be manifested in the internal excitations of the OH and Ti, possibly yielding a broad kinetic energy distribution ranging from $0.0-2.1$ eV which is relevant for studying the *type-a* background.

In order to model the energetics for the reaction 5.3 and thus a plausible FDD as a consequence, we use the possible electronic excitations of Ti [49], along with the relevant rotational and vibrational energy levels for OH to generate all possible combinations of the products internal states and thus using the balance as the kinetic energy release. The respective states have also been weighed by their degeneracy of $(2J+1)$, yielding a total of more than 900 possible product state combinations. This has been used to generate a functional model and thus define the reaction KER using the same. The model yields a probability dependence for energy which can well be approximated by an exponential function, given as,

$$P_{\mathrm{KER,bg}}(E_{bg}) = Ae^{-BE_{bg}} \tag{5.5}$$

where, E_{bg} is the expected KER value for the $TiOH^+$ recombination (between $0.0-2.1$ eV) yielding Ti and OH fragments and the parameters $A = 0.312$ and $B = 1.2854$ have been obtained by fitting the model based on aforementioned physical considerations, yielding the probability for the specific E_{bg}. The resulting FDD from the MC-simulation using the proposed model has been produced in the figure 5.9 with the $E_{\mathrm{d}} = 0.0$ eV data measured between $500-600$ seconds (as in the figure 5.8). It can be observed that the model shows a good agreement with the background data from ~ 6 mm upto 25 mm in the relevant intensity levels, and it is fairly independent of the change in the experimental detuning energy. Thus, we employ this model to fit the background (with appropriate scaling) along with the simulated distance curves as mentioned in the earlier section, the procedure for which has been elucidated further.

5.3.3 Fitting routine for generated distributions

To assimilate the experimental and analysis techniques developed until this point, the simulated set of 2D FDD plots generated for specific conditions of E_{d} and ΔE, along with the generated model for the background counts has to be compared with the recorded data

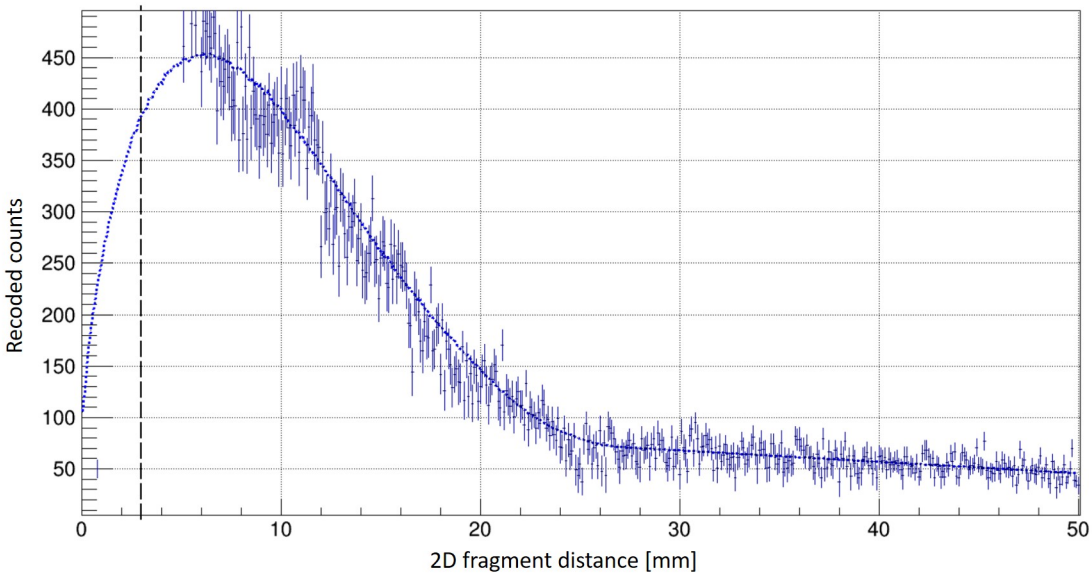

Figure 5.9: FDD from modelled background (dashed blue curve) generated using MC-simulations for an exponential functional model (exponentially decaying energy probability; see equation 5.5) fitted using physical considerations for $TiOH^+$ recombination resulting in break-up as Ti and OH fragments. This has been plotted over the data recorded for $E_d = 0.0$ eV data measured between 500−600 seconds (as in the figure 5.8). The vertical black dashed line represents the 3 mm mark, assumed as limit wherein significant effect for the expected *type-a* background can be observed.

from the experiment. Given that there are atleast twenty independent variables which can be adjusted to vary the shape of the composite curve, we resort to fitting the simulated curves to the acquired data. The fitting routine includes the input as the composite curve– essentially the simulated FDD curves for all energetically feasible channels, grouped together for optimisation as discussed in the previous sections. This ensemble is then used to fit the experimental data for the respective E_d by allowing for the scaling of individual channel curves, defining the fundamental strategy. It is important to note that given the area under each simulated single-channel FDD curve has been appropriately normalised, such direct scaling can be justified logically as essentially mimicking different branching ratios for each recombination channel, which are considered to be independently varying owing to no predetermined estimates or known behaviour of the reaction pathways for the DR under study. Thus, each of the grouped channels (Ch0 to Ch9) is scaled independently by a scaling parameter defined by the fitting routine, to fit the simulated full-composite to the acquired data from the experiment for various E_d. This fit is performed between the fragment distance interval of 1.6 mm to 8 mm, wherein the lower distance limit is defined

by the detector considerations (as elucidated sec. 4.2), and the upper limit has been set such that the significant data (above background) can be fit for the highest probed $E_{\rm d} = 150$ meV, while also keeping the fit limits constant for all data sets. The fitting routine sets the scaling parameters such that χ^2 goodness of fit parameter is optimised. This procedure is iterated systematically over different values of ΔE– our target variable, in the determined range for plausible endothermicity, and the fit-goodness is checked using the χ^2 parameter. Knowing that ΔE should be a constant of the reaction, expectedly independent of the electron-ion collision energy, various data-sets can be ultimately be combined to determine the final value and setting error estimates for the same. The discussion here follows review for the fitting wherein we have elaborately considered the data-set acquired for measurements between $500-600$ seconds, which can be similarly applied to the other datasets.

Understanding that the scaling parameters are physically analogous to branching rations for various channels, we define these to only take positive values. Further on, as for the considered dataset we have a total of nine distinct measurements representing data for $E_{\rm d} = 0$, 10, 20, 30, 40, 60, 90, 120, and 150 meV, as has been listed in table 3.2. Given that all relevant fitting parameters (e.g. fit limits, number of degrees of freedom, etc.) for the routine have been set to the same values for each $E_{\rm d}$, for an attempted fit with a specific ΔE value, the combined goodness of fit parameter is calculated as,

$$\chi^2_{{\rm t},\Delta E} = \frac{\chi^2_0 + \chi^2_{10} + \chi^2_{20} + \chi^2_{30} + \chi^2_{40} + \chi^2_{60} + \chi^2_{90} + \chi^2_{120} + \chi^2_{150}}{9} \tag{5.6}$$

where, $\chi^2_{E_{\rm d}}$ is the Chi-squared value obtained from individual $E_{\rm d}$ fit at the specific ΔE, an average of which gives the value of total goodness of fit parameter, $\chi^2_{{\rm t},\Delta E}$. Here it is noteworthy that given the fit limits, $1.6-8.0$ mm, with a data binning of 0.1 mm/bin, the number of degrees of freedom (NDF) for each plot is 64. At this point, it is instructive to introduce another relevant goodness-of-fit parameter, namely the reduced-χ^2, which is defined as,

$$\textit{red} - \chi^2_{{\rm t},\Delta E} = \frac{\sum \chi^2_{E_{\rm d},\Delta E}}{\sum {\rm NDF}_{E_{\rm d}}} \tag{5.7}$$

where *red*$-\chi^2$ parameter is considered optimized for a value close to 1. Faithful determination of the same requires that the number of degrees of freedom for a given detuning energy fit, ${\rm NDF}_{E_{\rm d}}$ is deduced appropriately. We note that for a particular fit, the NDF is reduced as one includes the number of independent fitting parameters, which in the case considered

by default amounts to 11, given the 10 scaling parameters required for each channel and an additional parameter to scale the background model appropriately. This can be slightly modified to obtain a more authentic goodness parameter by noting that for a given set of E_{d} and ΔE, only a given number of channels are energetically feasible, as has been discussed before. This fundamentally can be checked on purely energy considerations, and thus, for low detuning energies, the number of independent fitting parameters required to obtain a faithful fit can be reduced. Such a list, tabulating the detuning energies which need the specific channel to be included in the fit has been produced in the table 5.2, along with the list depicting the reaction channels as used in the new channel grouping scheme to optimise the fitting routine (see discussion in sec. 5.3.1). As listed in the table are grouped-channels which are kept 'open' for a fit (included as independent fit parameters) and have been resolved such that the fits are faithful for the range of endothermicities probed, i.e. -10 to 60 meV. Incorporating the aforementioned considerations, we can implement the fitting routine which, among other parameters and elaborate quantities, gives out the values for fitted scaling parameters, calculated χ^2 and reduced-χ^2 parameters for each curve and the cumulative data set which are used for further discussions and investigating the physical understanding arising from the same. Some of these observations and results have been discussed in the final section below.

5.3.4 Discussions and interim results

The data acquired and analysed over the course of this work, combined with the experimental program undertaken has brought forth exceedingly insightful and interesting set of measurements for the TiO^+ system undergoing electron recombination. The acquired data and the resulting plots produced are rich with information and detailed subtleties that are still being deciphered with the ongoing analysis at the time of writing of this work. The final part of section 4.2.3 already discusses some of the discernible characteristics of the recorded data. Using the fundamental understanding of the system and the ideas, techniques and procedures as developed in the preceding sections allows for a more detailed interpretation, wherein the advanced plot fitting routines have proven to be instrumental. These investigations have led to a further narrowing of the plausible range for endothermicity within a tentative bracket of -10 meV $< \Delta E <$ 43.0 meV, which is being looked at more intensively through analysis of the acquired multi-dimensional data. In this section we follow a compact discussion about detailed subtleties of mainly the data recorded for measurement between $500-600$ seconds, as understood at the time of writing of this

Channel Name	**Channels grouped** *(initial, final)*	**Used in E_{d}** [meV]
Ch0	(5/2, 0)	0, 10, 20, 30, 40, 60, 90, 120, 150
Ch1	(5/2, 1 + 2)	0, 10, 20, 30, 40, 60, 90, 120, 150
Ch2	(3/2, 0) + (5/2, 3)	0, 10, 20, 30, 40, 60, 90, 120, 150
Ch3	(5/2, 4)	0, 10, 20, 30, 40, 60, 90, 120, 150
Ch4	(3/2, 1 + 2) + (5/2, 5 + 6)	0, 10, 20, 30, 40, 60, 90, 120, 150
Ch5	(3/2, 3)	10, 20, 30, 40, 60, 90, 120, 150
Ch6	(3/2, 4) + (5/2, 7)	20, 30, 40 60, 90, 120, 150
Ch7	(3/2, 5 + 6) + (5/2, 8)	30, 40, 60, 90, 120, 150
Ch8	(3/2, 7)	40, 60, 90, 120, 150
Ch9	(3/2, 8)	60, 90, 120, 150

Table 5.2: The reaction channels are grouped together so as to optimise the fitting routine and make the fits more faithful. The approach yields a total of 10 final grouped-channels, as listed in the table, with channels included in each group depicted in the notation (initial, final), where *initial* represents the electronic state of the molecular ion (Ω = 3/2 or 5/2) partaking in the recombination and *final* denotes the product state index for the specific exit channel referred to (see table 5.1). Third column lists the detuning energies wherein the corresponding channel is expected to contribute (based on energy considerations) and is thus included as an independent parameter in the fitting routine.

work, which is further subject to possible improvements along the course of analysis. The obtained $\chi^2_{\mathrm{t},\Delta E}$ trends for fitting at various endothermicity values have been produced in figure 5.10. Also produced in figure 5.21 are the trends for individual detuning energies, i.e. $\chi^2_{E_{\mathrm{d}}}$ which have been instrumentally used in interpretation and discussions of the data, as follows. Regarding the produced fitting plots, it is important to note that the thick navy blue curve represents the total fitted curve, while thin solid colour curves represent the individual grouped-channel contributions according to the colours as represented 5.7, and the channel descriptions as in 5.2. Whereas, the dashed curves in the plot represent the sum of contributions from Ω = 3/2 (black) and Ω = 5/2 (red) states separately. Additionally the lowest curve in the figure is usually the modelled background curve also used in the fit. Further, the vertical black dashed line (and the shaded area) is indicative of the limit over which the imaging data is credible ($>$ 1.6 mm).

- **0 eV data**: This data category has high statistics available due to data acquisition for each cooling-step in the measurement scheme (see sec. 2.7) for both imaging- and

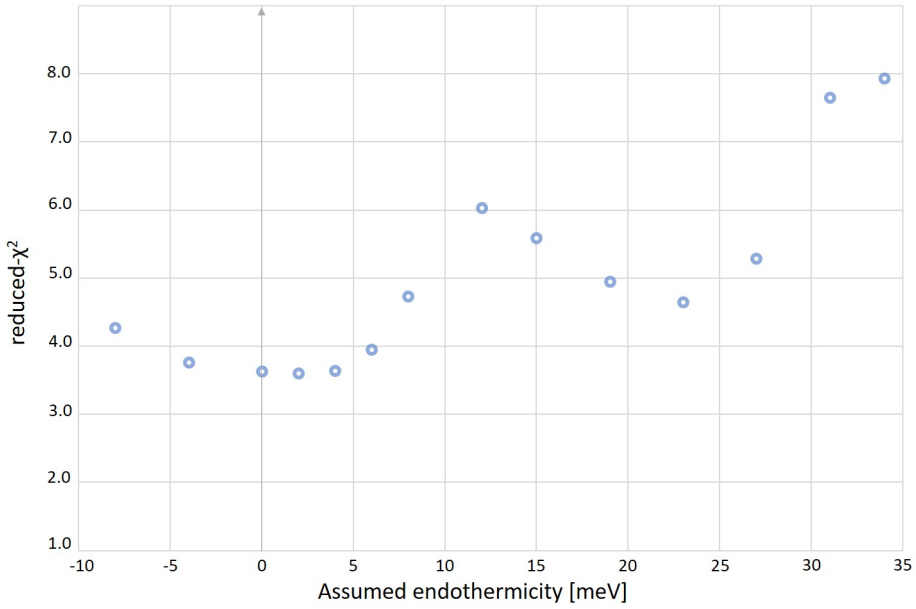

Figure 5.10: The obtained *red*-$\chi^2_{\mathrm{t},\Delta E}$ trends for fitting at various endothermicity values ΔE = -8, -4, 0, 2, 4, 6, 8, 12, 15, 19, 23, 27, 31 and 34 meV, calculated using eqn. 5.6.

rate-intensive measurement runs. Further, as a characteristic of the DR reaction, recombination at zero collision energy is independent of the molecule orientation with respect to the relative electron velocity, i.e. it is an isotropic reaction (anisotropy parameter $a_2 = 0$, see sec. 4.3.2). This provides an excellent opportunity to understand the FDD obtained which is closest to our assumptions at this stage of analysis. Considering the recorded data above the credible imaging threshold of 1.6 mm as in figure 4.14 the data shows a single feature, apparently a falling flank extend upto $\sim$2.6 mm without any shoulders or additional peaks. However, in the $E_{\mathrm{d}} = 0.0$ eV data measured between $1000-1100$ seconds, there is a faintly visible breaking feature for this flank close to 1.6 mm but is not a conclusive pattern (see fig. 4.15). Nevertheless, referring back to the 500 sec dataset, it can be proposed that the overall observed feature may be a remnant of a more significant feature peaking at distances less than 1.6 mm, which should also be the first dominant opening channel given that we see no further discernible characteristics in the data after this. Using the *Ch0* to fit the falling flank yields an optimum at $\Delta E \sim 23$ meV, while using the *Ch1* gives an optimal fit for $\Delta E \sim 4$ meV, as produced in figure 5.11. It can be remarked that for the given simulated shape of composite single-channel FDD (figure 5.5) the flank does not fit well for endothermicity greater than 23 meV, indicating another possible limiting condition for the upper limit of the endothermicity, given that the observed

feature in this dataset should be accounted for by atleast one possibility of a feasible reaction channel.

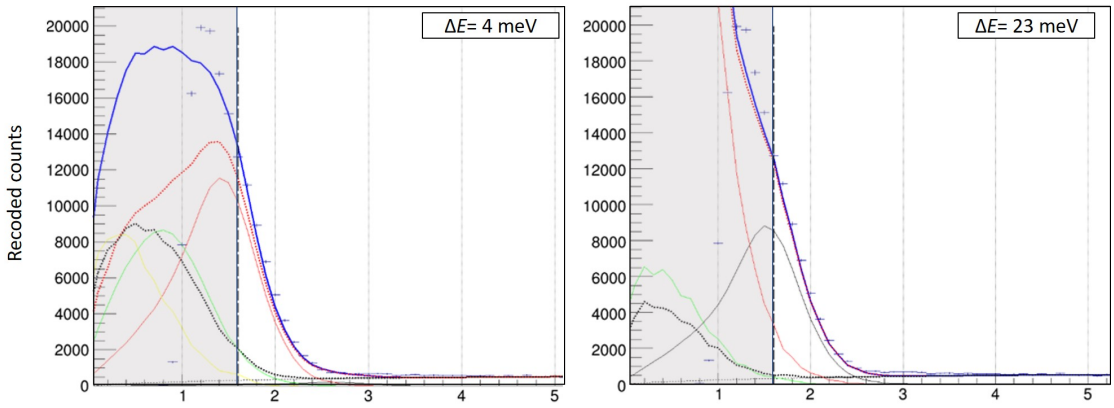

Figure 5.11: Data measured for $E_{\rm d}$ = 0.0 eV (between 500−600 sec) fitted for ΔE = 4 and 23 meV using the routine elucidated in the text. Note that the thick navy blue curve represents the total fitted curve; thin solid colour curves represent the individual grouped-channel contributions according to the colours as represented 5.7; whereas, the dashed curves in the plot represent the sum of contributions from Ω = 3/2 (black) and Ω = 5/2 (red) states separately. Additionally, the lowest curve in the figure is usually the modelled background curve also used in the fit. Further, the vertical black dashed line (and the shaded area) is indicative of the limit over which the imaging data is credible ($>$ 1.6 mm).

- **10 meV data**: The produced plot for this category records a sharp drop centered at ∼2.3 mm, complemented by a possible second feature comparatively feeble in intensity and peaking at ∼3 mm, as can be seen in 5.12. It can be proposed, following from the $E_{\rm d}$ = 0.0 meV data, that with a higher energy pumped into the system, the *Ch0* peak previously shrouded at distance <1.6 mm may have moved further, yielding a sharp dropping pattern, a convincing fit for which case is obtained for ΔE ∼31 meV; or this could be a contribution from both *Ch0* and *Ch1* if the data is inferred to have two separate features present, which produces an optimal fit for ΔE ∼4 meV.

- **20 and 30 meV data**: As compared to the $E_{\rm d}$ =10 meV data, the $E_{\rm d}$ =20 meV dataset (see fig. 5.13) shows a subtle broadening in the sharp decreasing feature around 2.4 mm. The feature now gets broader and a shoulder or prolongation after the feature is visible prominently above the background upto ∼4 mm. In this case the fitting routine yields convincing set of fits for ΔE < 15 meV, which is possible as for decreasing endothermicity more and more channels become energetically

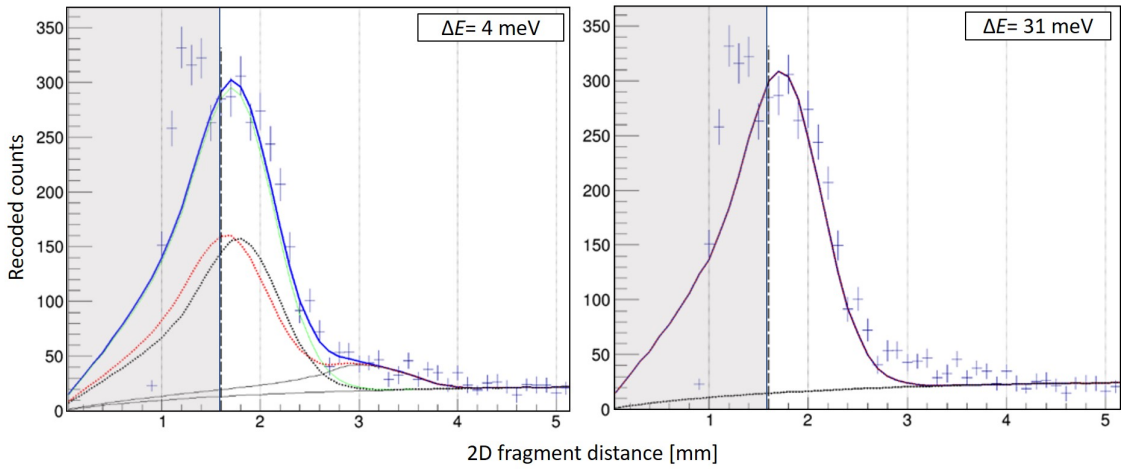

Figure 5.12: Data measured for $E_{\mathrm{d}} = 10$ meV (between 500−600 sec) and fitting for $\Delta E = 4$ and 31 meV.

feasible, providing an extended possibility for fit. This remark is cardinal for further discussions as well in case of other data.

The data for 30 meV detuning energy shows a more gradual slope with a further separated shoulder along with the major broad feature present approximately between 2.0−2.6 mm as can be seen in fig. 5.14. It seems that the first channel stemming from Ω =3/2 initial state may already be within the energetically feasible range here but it is unclear how much it contributed to the given case. The fitting routines fit differently for various endothermicities here, with a closely optimal fit obtained for $\Delta E = 23$ meV, and then again for a larger set of endotherimicities lying ΔE <12 meV.

- **40 meV data**: The obtained data for this category is especially intriguing due to a sharp and evidently distinguished peak structure visible at ∼2 mm, which is above the imaging limit threshold and thus most possibly, a credible feature. Furthermore, the data shows a step-like trend extending upto ∼4.5 mm. Here it seems that there are a minimum of four channels required to fit this appropriately as can be noticed in fig. 5.15. Any less shows an essential departure from the shape. It is noteworthy that for $E_{\mathrm{d}} = 40$ meV, considering higher endothermicities (> 22 meV) is highly improbable given that there are only 3 channels that would essentially be energetically feasible to participate in the fit in that case, yielding inconsistencies. Taking a step back again, fitting the clearly peaking feature at ∼2 mm is one of the sustaining problems at this stage of analysis, wherein it has not been possible to pin down the precise parameters

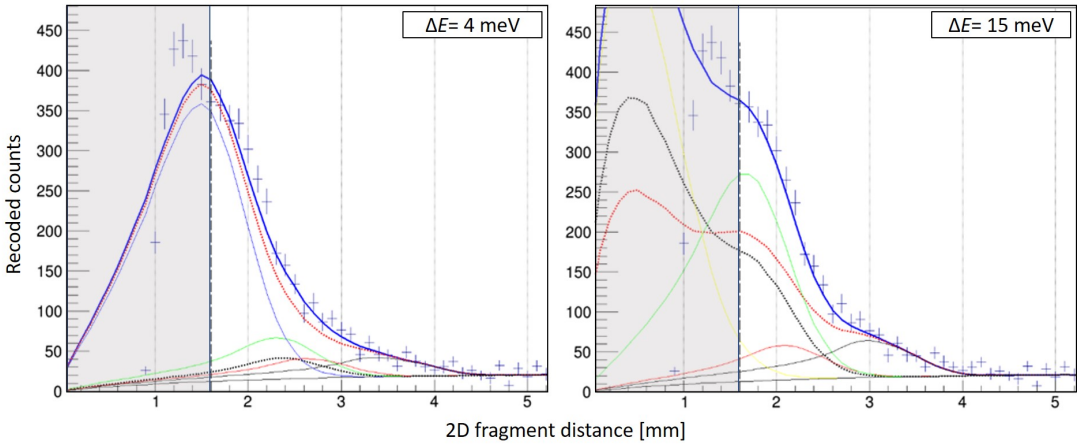

Figure 5.13: Data measured for $E_{\mathrm{d}} = 20$ meV (between 500−600 sec) and fitting for $\Delta E = 4$ and 15 meV.

producing conditions such that the peak width of the MC-simulated curves matches convincingly with the recorded data. This complicates the puzzle, leading to further iterations involving the inclusion of anisotropy in a systematic and deterministic manner in fitting so as to limit the parametric variations possible and yet understand the behaviour better for the changing FDD patterns. This part of analysis is still actively being built upon.

- **60 meV data**: This dataset produced in fig. 5.16 presents first clear trend towards moving away from a dense pattern at low fragment distances and with the appearance of a clear peaking feature above the imaging threshold (1.6 mm), noticeable at ∼2.2 mm. This imparts a considerable validity to our acquired data wherein we can now observe a clearly moving maxima with increasing electron-ion collision energy, and the reaction actually hints at demonstration of dynamical reaction pathways, strongly dependent on E_{d}. The fitting, however, from this point on gets increasingly complicated due to more than five channels participating to fit the features majorly lying between 1.6 mm and ∼5.6 mm. Thus, a satisfactory range of fits are produced by the routine for $\Delta E < 27$ meV, wherein the χ^2 value keeps getting better at lower endothermicities mainly due to the introduction of more channels in the fit, and thus a higher freedom for the procedure.

- **90, 120 and 150 meV data**: A systematic and consistent movement of the dominant peaking feature in the acquired data is visible for these detuning energies, wherein the characteristic curve seems to be moving out from the low distances and thus starts

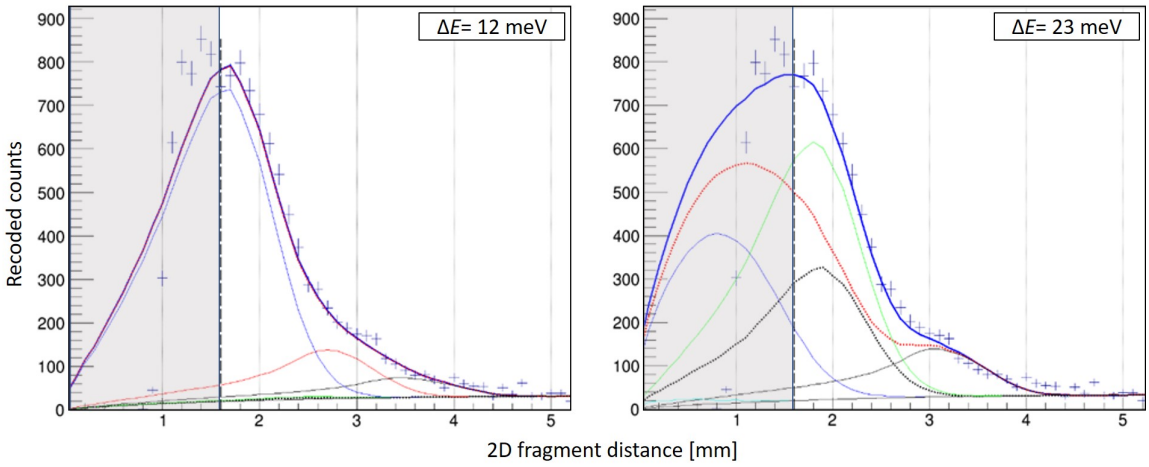

Figure 5.14: Data measured for $E_{\mathrm{d}} = 30$ meV (between 500−600 sec) and fitting for $\Delta E = 12$ and 23 meV.

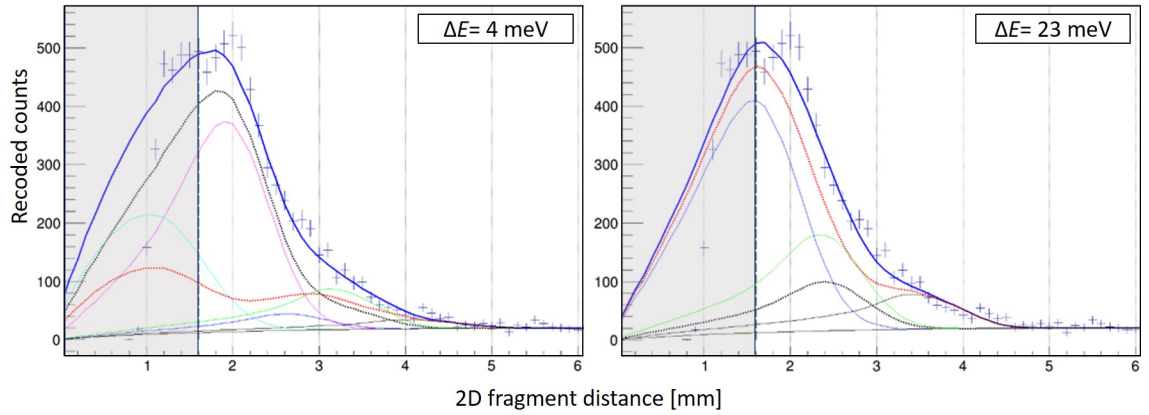

Figure 5.15: Data measured for $E_{\mathrm{d}} = 40$ meV (between 500−600 sec) and fitting for $\Delta E = 4$ and 23 meV.

to become visible. This feature appears to be a plateau or a pattern produced by dense set of closely spaced peaks. While this presents an excellent authentication for the recorded data by displaying an anticipated dependence on E_{d}, it also is an exceedingly instrumental piece of data to mark the dominant reaction channels essentially shaping the recombination process. The fitting routine for $E_{\mathrm{d}} = 90$ meV yields a possible endothermicity broadly for $\Delta E > 24$ meV or $\Delta E < 12$ meV, however the fits yield a close χ^2 value for all ΔE in the plausible range deduced in the previous sections, as produced in fig. 5.17. Further, for the $E_{\mathrm{d}} = 120$ and 150 meV, as shown in fig. 5.18 and 5.19 respectively, the deductions are actually similar as the broad features are noticeable and while the fitting yields indistinguishable results due to

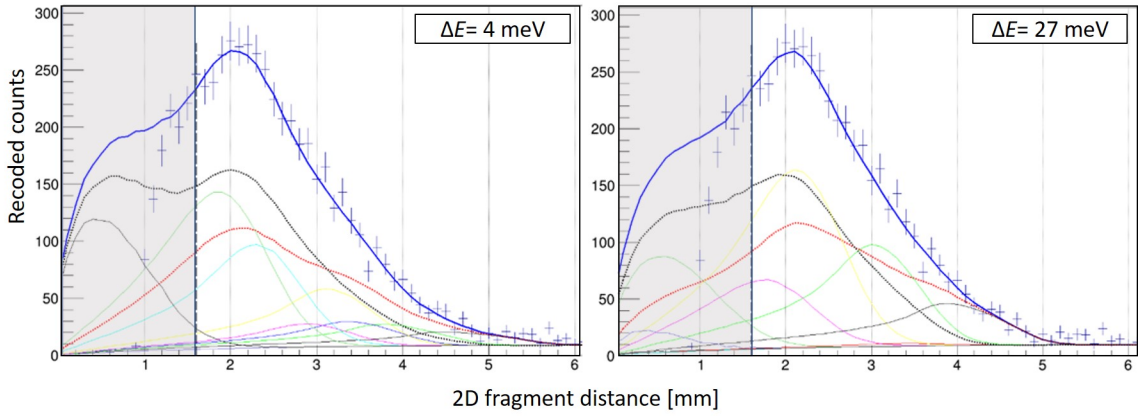

Figure 5.16: Data measured for $E_{\mathrm{d}} = 60$ meV (between 500−600 sec) and fitting for $\Delta E = 4$ and 27 meV.

high number of independently adjustable parameters available. It can be observed, however, that the χ^2 value shows an increasing trend with lowering ΔE– this can be attributed to the fact that all of the ten grouped-channels are considerably exothermic at the given conditions and have peaks (d_{rep}) at distances greater than 2 mm. Thus, as the ΔE is decreased, the composite curves move further at higher distances, thus leaving the low-distance data points out of the possible fit. This is however surmountable by including recombination anisotropy (see sec. 4.3.2) wherein for anisotropy parameter $a_2 > 0.0$ the FDD assumes a broader shape (refer to fig. 4.28).

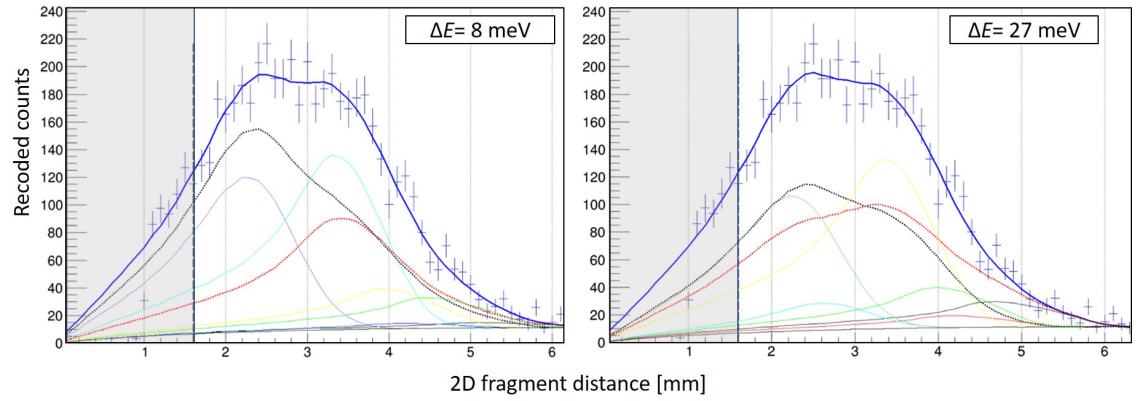

Figure 5.17: Data measured for $E_{\mathrm{d}} = 90$ meV (between 500−600 sec) and fitting for $\Delta E = 8$ and 27 meV.

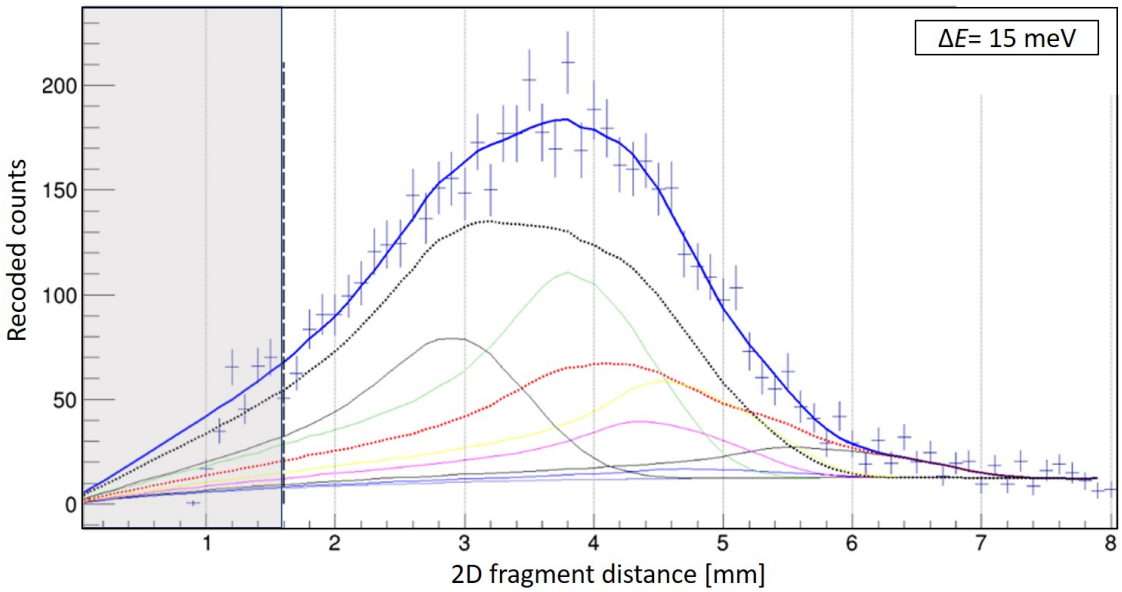

Figure 5.18: Data measured for $E_{\mathrm{d}} = 120$ meV (between 500−600 sec) and fitting for $\Delta E = 15$ meV.

The preceding discussions briefly highlight some of the significant characteristics of the data, and the insights obtained over the course of the analysis. It is also remarked that in the produced χ^2 curves, viz. fig. 5.21 and 5.20 (separately shown for the purposes of clarity) that depict the *red*-χ^2 quantity, these are essentially to be considered as indicative of the relative trends, while the precise values are subject to further details which have not been addressed here for the purposes of brevity. The fitted curves for endothermicity values ΔE have been produced in the appendix A and can be referred to for the purposes of discussions as well as an understanding of the fitting method and the implementation results thereof. Following from the aforementioned discussions and noting the χ^2 trends, at this point, the estimated endothermicity bracket for the DR reaction of TiO^+ is **2 meV** $< \boldsymbol{\Delta E} <$ **12 meV**. The ongoing analysis to resolve the remaining minor discrepancies in the fits is not expected to bring the final endothermicity value out of this range. The details on the planned analysis have been briefly underscored in the final chapter of this thesis.

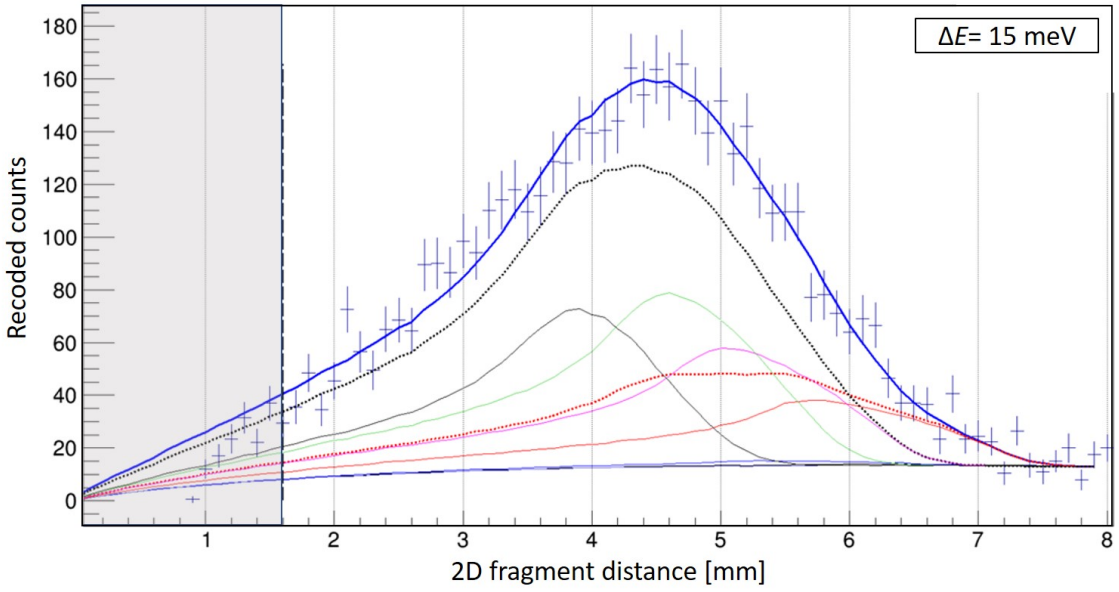

Figure 5.19: Data measured for $E_{\mathrm{d}} = 150$ meV (between 500−600 sec) and fitting for $\Delta E = 15$ meV.

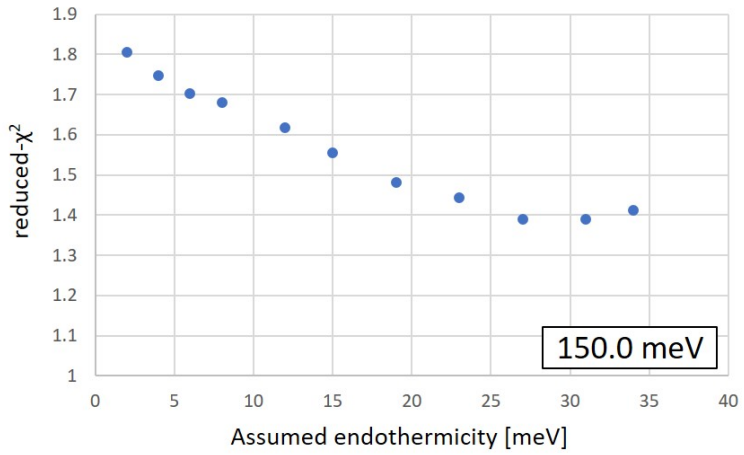

Figure 5.20: The goodness-of-fit, i.e. *red*-$\chi^2_{E_{\mathrm{d}}}$, trends obtained by using the fitting routine for data acquired at $E_{\mathrm{d}} = 150.0$ meV, within the 500−600 sec measurement dataset, calculated according to eqn. 5.7, similar to fig. 5.21.

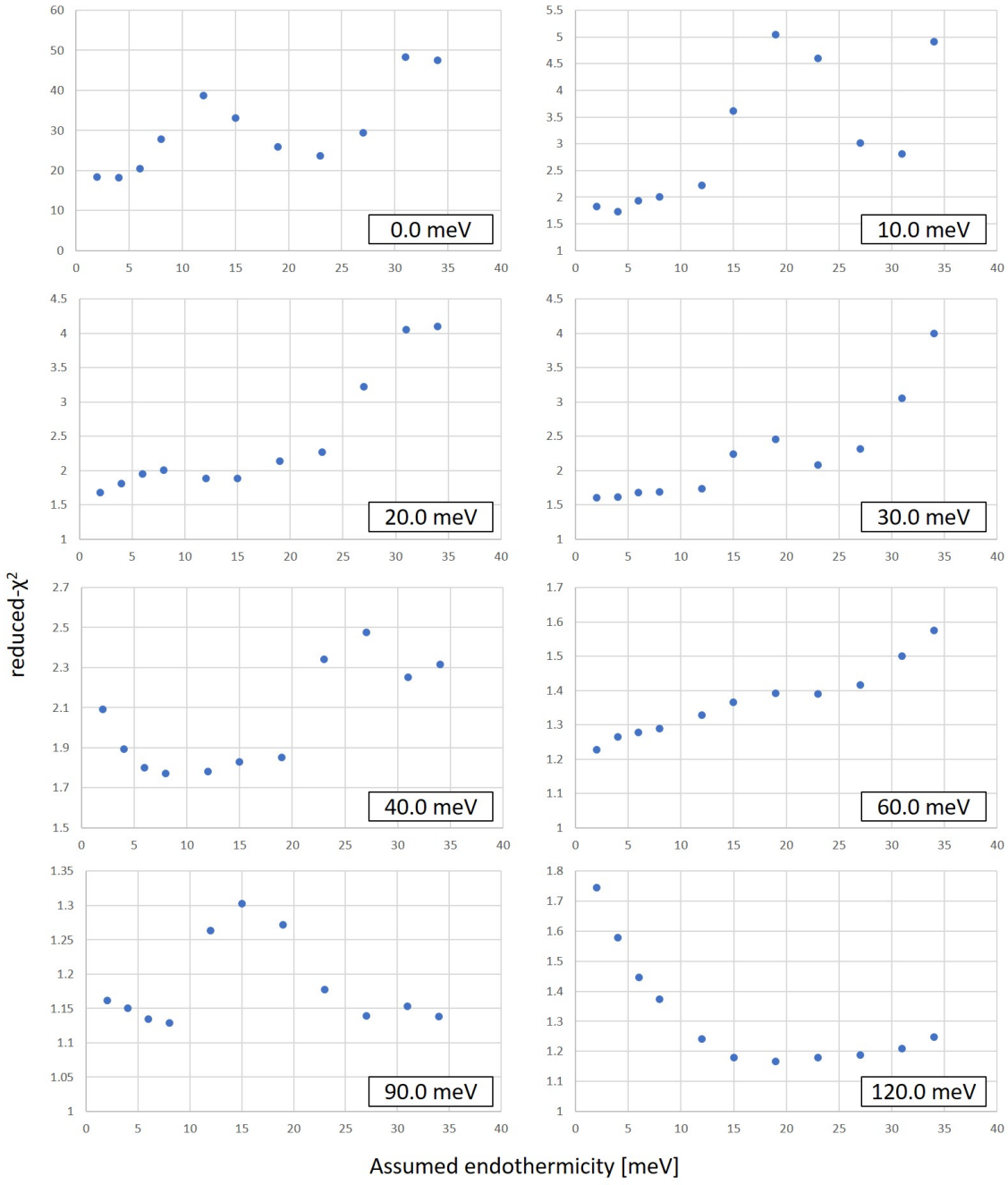

Figure 5.21: The goodness-of-fit, i.e. *red*-$\chi^2_{E_\mathrm{d}}$, trends obtained by using the fitting routine for data acquired at individual detuning energies $E_\mathrm{d} = 0$, 10, 20, 30, 40, 60, 90, 120 meV, within the 500−600 sec measurement dataset, calculated according to eqn. 5.7 for $\Delta E =$ 2, 4, 6, 8, 12, 15, 19, 23, 27, 31 and 34 meV.

Chapter 6

Summary and Outlook

Produced in this work is an exhaustive account of the detailed study comprising of experimental preparation, measurement campaign, data analysis, and interpretation of the interim results obtained for the dissociative electron recombination reaction of TiO^+ molecule performed at the electrostatic Cryogenic Storage Ring (CSR) at the Max-Planck-Institute for Nuclear Physics in Heidelberg.

The titanium monoxide cation has been discussed to be an especially intriguing system due to the hypothesized endothermic DR (with the best known value at the time of production of this work as $E_{\mathrm{reac}} = -0.05 \pm 0.07$ eV). To the best of our knowledge, no direct investigation of the specific DR reactions for such class of reactions had been carried out until the time of production of this work, experimentally or theoretically. Precise laboratory study of the reaction down to an electron-ion collision energy resolution of meV, a primary goal of this study, necessitated an in-depth understanding and customisation of the experimental conditions at the electron cooler (eCool) section of the CSR. A broad perspective of TiO^+ as a molecular system has been presented, with a recapitulation of its major characteristics including a considerably high ion mass of 64 u, electronic structure of the molecule as well as for that of the expected atomic products Ti and O. Consequently, calculations for the rotational and vibrational energy levels and state lifetimes were carried out for the two fine-structure states of the molecule ($\Omega = 3/2$ and $\Omega = 5/2$) relevant for the probed energy levels in the experiment. Further an elaborate routine developed by the group was used to simulate radiative cooling for the molecular ion within the cryogenic environment of the CSR.

To perform electron cooling and access the aimed collision energies for the 280 keV energetic TiO^+ ion beam, merged beams technique was employed at the eCool section, which required an electron beam of $\sim$2 eV energy in the lab-frame tuned with a precision of a few meV. In order to achieve this, the characteristics for the cold electron beam pro-

duced at the cold electron emitter bank (CEEB) were investigated in detail, including the optimisation of beam profile with respect to varying electron-gun electrode conditions and the calibration of the beam steering elements through the $\sim$1.2-meter long electron beam path at the eCool before the experimental beamtime.

The experiment was conducted in December 2019 beamtime at the CSR. A $\sim$20 nA strong TiO^+ was made available by an in-house sputtering Penning ion source and transferred to the storage ring for injection, wherein average lifetimes of > 1100 seconds were recorded for the injected ion beam. The measurement campaign involved data acquisition for various relevant collision energies set as electron beam detuning with respect to the ion beam (E_d), for different predetermined storage times inside the CSR (with electrons off), viz. 0 sec, 500 sec, 1000 sec and 1500 sec, allowing for radiative cooling of the molecular ions. Measurements were performed using rapid energy-wobbling schemes in injection cycles for each run, customised for the rate-intensive and imaging-intensive measurements aimed at understanding the reaction kinetics as well as energetics respectively. The collected data comprised of neutral product fragment timing and position information, recorded event-wise at an average rate within a hundred to few thousand Hertz. The data was efficiently synchronised, acquired, and filtered online for optimal storage using an FPGA-based acquisition system developed by the working group for further analysis.

The latter half of this work was dedicated to the analysis of recorded data from the experiment. Firstly, a calibration procedure was carried out for the conversion of acquired data from the pixel-space (owing to properties of the MCP and Phosphor-screen based neutral fragment detection system) to the physical mm-space. This was a critical procedure that involved an elaborate search for various possible calibration functions to fit the data, and understanding the systematic effects. Following this, the acquired multi-dimensional data was appropriately segregated, filtered to only include the credible events, and thus the resulting fragment distance distribution (FDD) plots were generated for various categories of detuning energies and measurement times in the recorded data separately.

To better understand the intricacies of the FDDs, an elaborate Monte-Carlo simulation model was created to account for various statistical and systematic effects arising from the realistic electron beam energy spread and geometrical considerations of the experimental setup and the electron-ion system at the smallest relevant scales, dealing with the collision, fragmentation and detection processes meticulously. Various assumptions were made at this stage to model the realistic effects, and such approximations were quantified, improved with progressive iterations and dealt with minutely in the further course.

A detailed investigation of reaction energetics (endothermicity) was undertaken by us-

ing the developed MC-simulation routine as a part of this work. At this point, it is important to note the concept of this analysis in a straightforward picture– the initial energy of the reaction ($E_{\rm i} = E_{\rm i,Ti} + E_{\rm i,e}$) is defined by the electronic and rovibrational state energy of the molecule and the energy of the incoming electron (in the system's center-of-mass frame). The reaction then proceeds through recombination to dissociation or fragmentation– a mechanism or pathway for such an endothermic DR is not clearly known, and developing a plausible understanding for the same has been one of the objectives of this work. The DR results in to two neutral atomic fragments as products, namely Ti and O, which manifest the final energy of the reaction ($E_{\rm f} = E_{\rm f,int} + E_{\rm f,KER}$) as either internal excitations or as kinetic energy. This difference between the lowest possible final and initial state energies of the reaction has been termed as the endothermicity (ΔE), in line with the hypothesis that the difference between final energy and initial energy ($E_{\rm f} - E_{\rm i}$) is a constant positive offset, an unusual phenomenon. In order to deduce endothermicity of the reaction, one of the major objectives of this work, we use the fragment distance statistics obtained for the neutral products, which have a direct correlation with the kinetic energy release (KER) of the target reaction. This concept was examined, its validity established, and further executed in this work.

A first estimation of the possible range of endothermicity was deduced by employing the level stick-diagram visualisation of the MC-simulated FDDs with the acquired data, which provides an intuitive and succinct picture of the expected FDD patterns when all possible reaction channels with plausible KER ($E_{\rm KER} > 0$) are accounted for, given the $E_{\rm d}$ and ΔE as distinguishing parameters for each iteration. A bracket of -10 meV $< \Delta E <$ 43 meV was proposed using concrete reasoning through this method, as in the analysis stage at the time of writing of this thesis. This is to be seen in contrast with the available endothermicity estimates in literature before this study (ΔE= 50 $\pm$ 70 meV). Further on, the deduced narrower range for plausible endothermicity was probed in detail using explicit fitting of the FDD obtained utilizing the MC-modelling, to the recorded data for each detuning energy according to the measurement times. This procedure was implemented as a part of this work, wherein the goodness of executed fit was quantified using χ^2 parameter. The fitting results and discussion for the acquired 500$-$600 sec measurement data have been discussed here briefly, and the corresponding χ^2 plots have been produced. This procedure, in the stage as at the time of writing of this thesis, reveals the endothermicity range to lie within 2 meV $< \Delta E <$ 12 meV for the TiO^+ DR.

As discussed, while elaborate procedures have been developed and implemented to understand the measured data for the DR reaction of TiO^+ molecular ion, a more detailed

analysis of the same is still underway. As one aspect not described in this work the analysis of rate constant for the reaction is in progress. On the other hand, some of the major puzzles in the precise determination of reaction energetics– the parameter primarily addressed in this study– still remain to be unraveled completely, including the resolution of exact χ^2 values for the fits, and a better implementation thereof so as to optimise the same. This requires scrutinizing the obtained fitted curves, and gaining a deeper understanding of the possible sources of inconsistent fitting regions followed by an investigation into the plausible processes or realistic effects that may still be unaccounted for in the MC-model for the simulated FDDs. Given that we probe exceedingly low lab-frame energies, it is imperative to account for the most trivial effects that may play a role in the experimental measurements. As another avenue, the current FDD simulation considers an isotropic recombination probability with respect to θ, the molecular orientation in context with the velocity of the recombining electron. This can be extended to include the anisotropy as a fit parameter, which would still lead to a more realistic depiction of the process and consequently a better fitting. It is to be remarked that given the limited knowledge about the system through literature, a number of well-accounted yet simplifying assumptions have been made in the MC-simulation of FDD curves, as well as in the fitting routine (such as considering equal cross sections for individual rotational states within each channel, for instance), each of which may well be required to be inspected in meticulous detail in the further course of this analysis. At the time of the documentation of this work, these constituents are still being investigated thoroughly, and we strongly expect to pin down the details of this DR reaction to an unprecedented precision in the further course of this work, setting a first result of its kind in the field, in due course of time.

Bibliography

[1] T. J. Millar, "Topical review: Astrochemistry," *Plasma Sources Sci. Technol. 24 043001.*, 2015.

[2] A. Florescu-Mitchell and J. Mitchell, "Dissociative recombination," *Physics Reports, 277-374 (430).*, 2006.

[3] E. Herbst, "Molecular ions in interstellar reaction networks," *J. Phys.: Conf. Ser. 4, 003*, 2005.

[4] A. E. Orel and L. Mats, "Dissociative recombination of molecular ions," *Cambridge Molecular Science*, 2008.

[5] R. von Hahn *et al.*, "The cryogenic storage ring CSR," *Review of Scientific Instruments, 87 (063115)*, 2016.

[6] A. O'Connor *et al.*, "Photodissociation of an internally cold beam of CH^+ ions in a cryogenic storage ring," *Physical Review Letters 116, 113002.*, 2008.

[7] T. Dunham, "Interstellar neutral potassium and neutral calcium," *Astronomical Society of the Pacific, Vol. 49, Number 287.*, 1937.

[8] A. E. Douglas and G. Herzberg, "Note on CH^+ in interstellar space and in the laboratory," *Astrophysical Journal, Vol. 94, p.381.*, 1941.

[9] O. Berné, N. L. J. Cox, G. Mulas, and C. Joblin, "Detection of buckminsterfullerene emission in the diffuse interstellar medium," *Astronomy Astrophysics, Vol. 605, L1.*, 2017.

[10] J. Cami, J. Bernard-Salas, E. Peeters, and S. E. Malek, "Detection of C_{60} and C_{70} in a young planetary nebula." *Science, 329 (5996):1180-2.*, 2010.

[11] S. Petrie and B. Diethard, "Associative ionization processes within interstellar clouds," *The Astrophysical Journal, 436.*, 1994.

[12] T. Millar, J. Ellder, A. Hjalmarson, and H. Olofsson, "Searches for interstellar and circumstellar metal oxides and chlorides," *Astron. Astrophys. 182, 143-149.*, 1987.

[13] L. Spitzer and E. B. Jenkins, "Ultraviolet studies of the interstellar gas," *Annual Review of Astronomy and Astrophysics, Vol. 13:133-164*, 1975.

[14] G. Stokes, "Interstellar titanium," *Astrophysical Journal, Suppl. Ser., Vol. 36, p. 115-141*, 1978.

[15] E. Churchwell *et al.*, "Interstellar titanium monoxide: Limits and implications." *The Astronomical Journal, Vol. 85.*, 1980.

[16] U. Jørgensen, "Effects of TiO in stellar atmospheres," *Astronomy and Astrophysics, Vol. 284, p. 179-186.*, 1993.

[17] T. Kaminski *et al.*, "Pure rotational spectra of TiO and TiO_2 in VY-Canis Majoris," *Astronomy and Astrophysics, Vol. 551.*, 2013.

[18] M. J. Reid and J. E. Goldston., "How Mira variables change visual light by a thousandfold," *The Astrophysical Journal, 568:931–938.*, 2002.

[19] Y. Pan, Z. Luo, Y. Chang, K. Lau, and C. Ng, "High-level ab initio predictions for the ionization energies, bond dissociation energies, and heats of formation of titanium oxides and their cations TiO_n/TiO_n^+, n = 1 and 2," *J. Phys. Chem. A, 121, 669679*, 2017.

[20] M. Oppenheimer and A. Dalgarno., "Associative ionization and interstellar TiO^+ and TiO," *The Astrophysical Journal, 212:683-684.*, 1977.

[21] N. S. Shuman, D. E. Hunton, and A. A. Viggiano, "Ambient and modified atmospheric ion chemistry: From top to bottom," *Chem. Rev., 115, 45424570.*, 2015.

[22] R. M. Cox, J. Kim, P. B. Armentrout, J. Bartlett, R. A. VanGundy, M. C. Heaven, S. G. Ard, J. J. Melko, N. S. Shuman, and A. A. Viggiano, "Evaluation of the exothermicity of the chemi-ionization reaction Sm + O $\rightarrow$ SmO^+ + e^-," *J. Chem. Phys. 142, 134307.*, 2015.

[23] S. G. Ard, N. S. Shuman, O. M. Jr., P. B. Armentrout, and A. A. Viggiano, "Chemi-ionization reactions of La, Pr, Tb, and Ho with atomic O and La with N_2O from 200 to 450 K," *J. Chem. Phys. 145, 084302.*, 2016.

[24] M. Ghiassee, J. Kim, and P. B. Armentrout, "Evaluation of the exothermicity of the chemi-ionization reaction Nd + O $\rightarrow$ NdO^+ + e and neodymium oxide, carbide, dioxide, and carbonyl cation bond energies," *J. Chem. Phys. 150, 144309.*, 2019.

[25] W. Petersen *et al.*, "On the sources of energization of molecular ions at ionospheric altitudes," *Journal of Geophysical Research, Vol. 99, Issue A12, p. 23257-23274.*, 1994.

[26] R. Thomas, "When electrons meet molecular ions and what happens next: Dissociative recombination from interstellar molecular clouds to internal combustion engines." *Mass Spectrometry Reviews, 2008, 27, 485 – 530.*, 2008.

[27] I. G. Boger and A. Sternberg, "Bistability in interstellar gas-phase chemistry," *The Astrophysical Journal, Vol. 645, Issue 1, pp. 314-323.*, 2006.

[28] W. D. Geppert and M. Larsson., "Dissociative recombination in the interstellar medium and planetary ionospheres," *Molecular Physics, Taylor Francis, 106 (16-18), pp. 2199-2226.*, 2008.

[29] O. Novotný *et al.*, "Quantum-state–selective electron recombination studies suggest enhanced abundance of primordial HeH^+," *Science Vol. 365, 6454, pp. 676-679*, 2019.

[30] O. Novotný, A. Becker, H. Buhr, C. Domesle, W. Geppert, M. Grieser, C. Krantz, H. Kreckel, R. Repnow, D. Schwalm, K. Spruck, J. Stützel, B. Yang, A. Wolf, and D. Savin, "Dissociative recombination measurements of HCl^+ using an ion storage ring," *Astrophysics Journal, 54,*, 2013.

[31] O. Novotný *et al.*, "The dissociative recombination of fluorocarbon ions: II. CF^+," *Journal of Physics B: Atomic, Molecular, and Optical Physics, Vol. 38, Issue 10, pp. 1471-1482.*, 2005.

[32] ——, "Fragmentation channels in dissociative electron recombination with Hydronium and other astrophysically important species," *Phys. Chem. A, 114, 14, 4870–4874.*, 2010.

[33] S. Novotny, "Fragmentation of molecular ions in slow electron collisions," *Ph.D. Thesis.*, 2008.

[34] E. Martínez-Ferrero, Y. Sakatani, C. Boissière, D. Grosso, A. Fuertes, J. Fraxedas, and C. Sanchez, "Nanostructured titanium oxynitride porous thin films as efficient visible-active photocatalysts," *Adv. Funct. Mater., 17, 3348–3354*, 2007.

[35] H.-G. Xu *et al.*, "Interaction of TiO^+ with water: infrared photodissociation spectroscopy and density functional calculations," *Phys. Chem. Chem. Phys., 15, 17126*, 2013.

[36] Z. Shang *et al.*, "Synthesis of single-crystal TiO_2 nanowire using titanium monoxide powder by thermal evaporation," *J. Mater. Sci. Technol., 28(5), 385–390*, 2012.

[37] H. Lo and W. Fite, "Associative ionization of Ti, Zr, Mg and Th in collisions with O and O_2," *Chem. Phys. Letters, Vol. 29, No. 1.*, 1974.

[38] J. M. Dyke, B. W. J. Gravenor, G. D. Josland, R. A. Lewis, and A. Morris., "A gas phase investigation of titanium monoxide and atomic titanium using high temperature photoelectron spectroscopy," *Molecular Physics, Vol. 53, No. 2, 465-477.*, 1984.

[39] A. O. Sappey, G. Eiden, J. E. Harrington, and J. C. Weisshaar, "Vibronic structure of TiO^+ from multiphoton ionization photoelectron spectroscopy," *J. Chem. Phys. 90, 1415.*, 1989.

[40] D. E. Clemmer, J. L. Elkind, N. Aristov, and P. B. Armentrout, "Reaction of Sc^+, Ti^+, and V^+ with CO. MC^+ and MO^+ bond energies," *J. Chem. Phys. 95, 3387.*, 1991.

[41] H.-P. Loock, B. Simard, S. Wallin, and C. Linton, "Ionization potentials and bond energies of TiO, ZrO, NbO and MoO," *J. Chem. Phys. 109, 8980.*, 1998.

[42] K. M. Perera and R. B. Metz, "Photodissociation spectroscopy and dissociation dynamics of TiO_2 (CO_2)," *J. Phys. Chem. A, 113, 6253–6259.*, 2009.

[43] E. Miliordos and A. Mavridis, "Electronic structure and bonding of the early $3d$ transition metal diatomic oxides and their ions: $ScO^{\pm}$, $TiO^{\pm}$, $CrO^{\pm}$ and $MnO^{\pm}$," *J. Phys. Chem. A, 114, 8536–8572.*, 2010.

[44] C. M. Andreazza, A. A. de Almeida, R. M. Vichietti, and D. T. Ceccatto, "Radiative association of Ti and O atoms," *Mon. Not. R. Astron. Soc. 427, 833–838.*, 2012.

[45] D. Clemmer *et al.*, *J. Chem. Phys., 95.*, 1992.

[46] C. Naulin *et al.*, *Chemical Physics Letters, 266.*, 1997.

[47] L. Matsuoka *et al.*, *J. Opt. Soc. Am. B, 24.*, 2007.

[48] H. Huang, Z. Luo, Y. C. Chang, K.-C. Lau, and C. Y. Ng, "Rovibronically selected and resolved two-color laser photoionization and photoelectron study of titanium monoxide cation," *J. Chem. Phys. 138, 174309.*, 2013.

[49] E. Saloman, "Energy levels and observed spectral lines of neutral and singly ionized titanium, Ti I and Ti II," *J. Phys. Chem. Ref. Data 41, 013101.*, 2012.

[50] C. Moore, "Tables of spectra of hydrogen, carbon, nitrogen, and oxygen atoms and ions," *CRC Series in Evaluated Data in Atomic Physics, 339 pp.*, 1993.

[51] D. Zajfman *et al.*, "Physics with electrostatic rings and traps," *J. Phys. B: At. Mol. Opt. Phys. 37*, 2004.

[52] F. Hinterberger, "Physics of particle accelerators and ion optics," *Springer publications*, 2008.

[53] P. Wilhelm, "First studies of low-energy electron cooling of keV energy ion beams at the electrostatic cryogenic storage ring CSR," *PhD. Thesis.*, 2019.

[54] N. Tongnopparat, L. D. Yu, T. Vilaithong, and H. Wiedemann, "Ion beam emittance measurement based on transformation matrix theory," *J. Korean Physical Society, Vol. 53, No. 6, pp. 37443748*, 2008.

[55] G. Hill, "On the part of the motion of the lunar oerigee which is a function of the mean motions of the Sun and Moon," *Acta Mathematica, 8(1):7*, 1886.

[56] S. Vogel, "Developments at an electrostatic cryogenic storage ring for electron-cooled kev energy ion beams," *PhD. Thesis.*, 2016.

[57] D. Orlov, U. Weigel, D. Schwalm, A. Terekhov, and A. Wolf., "A new type of photoemitter," *Nuclear Instruments and Methods in Physics Research A, 532, 418–421.*, 2004.

[58] J. J. Scheer and J. van Laar, "A new type of photoemitter," *Solid State Commun., 3(189).*, 1965.

[59] A. Shornikov, "An electron cooler for ultra-low energy cryogenic operation," *PhD. Thesis.*, 2012.

[60] S. Pastuszka, U. Schramm, M.Grieser, C. Broude, R. Grimm, D.Habs, J.Kenntner, H. J. Miesner, D. Schwalm, and A. Wolf, "Electron cooling and recombination experiments with an adiabatically expanded electron beam," *Nuclear Instruments and Methods in Physics Research A, 369, 11-22*, 1996.

[61] G. H. Jansen, "Coulomb interactions in particle beams," *Boston Academic Press*, 1990.

[62] S. M. Trujillo, R. H. Neynaber, and E. W. Rothe, "Merging beams, a different approach to collisional cross section measurements," *Rev. Sci. Instrum., 37, 1655-1661*, 1966.

[63] R. A. Phaneu, C. C. Havener, G. H. Dunn, and A. Müller, "Merged-beams experiments in atomic and molecular physics," *Rep. Prog. Phys. 62 1143*, 1999.

[64] L. S. Jr., "Physics of fully ionized gases," *Wiley Sons, New York London, 2nd edition*, 1962.

[65] A. Becker, "Imaging of neutral fragmentation products from fast molecular ion beams: Paving the way for reaction studies in cryogenic environment," *PhD. Thesis.*, 2016.

[66] P. Roth and G. Fraser, "Microchannel plate resistance at cryogenic temperatures," *Nuclear Instruments and Methods in Physics Research Section A: Accelerators, Spectrometers, Detectors and Associated Equipment, Vol. 439, pp. 134-137*, 2000.

[67] S. Rosén, H. T. Schmidt, P. Reinhed, D. Fischer, R. D. Thomas, H. Cederquist, L. Liljeby, L. Bagge, S. Leontein, and M. Blom, "Operating a triple stack microchannel plate-phosphor assembly for single particle counting in the 12-300 K temperature range," *Review of Scientific Instruments, Vol. 78, p. 113301*, 2007.

[68] Z. Amitay, D. Zajfman, P. Forck, U. Hechtfischer, B. Seidel, M. Grieser, D. Habs, R. Repnow, D. Schwalm, and A. Wolf, "Dissociative recombination of CH^+: Cross section and final states," *Physical Review A, Vol. 54, No. 5*, 1996.

[69] Z. Nouri, R. Li, R. Holt, and S. Rosner, "A penning sputter ion source with very low energy spread," *Nuclear Instruments and Methods in Physics Research A, 614, 174–178*, 2010.

[70] W. Schuurman, "Investigation of a low pressure penning discharge," *Physica, 36, pp. 136-160*, 1967.

[71] E. Miliordos, J. F. Harrison, and K. L. C. Hunt, "Ab initio investigation of titanium hydroxide isomers and their cations, $TiOH^{0,+}$ and $HTiO^{0,+}$," *The Journal of chemical physics, 135, 144111*, 2011.

[72] M. Rimmler, "Operating a low-energy electron cooler at the cryogenic storage ring CSR," *Master thesis.*, 2017.

[73] M. Beutelspacher, M. Grieser, K. Noda, D. Schwalm, and A. Wolf, "Dispersive electron cooling experiments at the heavy ion storage ring TSR," *Nuclear Instruments and Methods in Physics Research A, 512, 459–469.*, 2003.

[74] L. S. Rothman *et al.*, "The HITRAN 2012 molecular spectroscopic database," *J. Quant. Spectrosc. Radiat. Transfer 130, 4-50.*, 2013.

[75] R. Bennett, "Hönl–London factors for doublet transitions in diatomic molecules," *Monthly Notices of the Royal Astronomical Society, Vol. 147, Issue 1.*, 1970.

[76] P. F. Bernath, "Spectra of atoms and molecules." *Oxford University Press.*, 1995.

[77] S. Saurabh, "Collision studies with internally cold ion beams and merged electron beams in a cryogenic storage ring," *PhD. Thesis.*, 2019.

[78] M. Larsson, H. Danared, J. R. Mowat, P. Sigray, G. Sundström, L. Broström, A. Filevich, A. Källberg, S. Mannervik, K. G. Rensfelt, and S. Datz, "Direct high-energy neutral-channel dissociative recombination of cold H_3^+ in an ion storage ring," *Phys. Rev. Lett. 70, 430*, 1993.

[79] T. F. Magnera, D. E. David, and J. Michl, "Gas-phase water and hydroxyl binding energies for monopositive first-row transition metal ions," *J. Am. Chem. Soc., 111, 11, 4100–4101*, 1989.

[80] B. Ruscic *et al.*, "On the enthalpy of formation of hydroxyl radical and gas-phase bond dissociation energies of water and hydroxyl," *J. Phys. Chem. A, 106, 2727-2747*, 2002.

Appendix A

Curve fitting for endothermicity determination

The following figures depict the fitted curves obtained by the using the procedure as outlined in the Chapter 5, wherein the measured data for various detuning energies and storage times has been used to deduce the reaction endothermicity ΔE. Here we have produced the curve fittings for the $500-600$ seconds measurement dataset for assumed endothermicity ΔE= 4 meV and 23 meV, where the noticeable local minimum in the χ^2 curves (refer to fig. 5.10) was visible according to the investigations until the time of writing this thesis. The aforementioned dataset consists of fragment distance distribution data acquired for $E_{\mathrm{d}} =$ 0, 10, 20, 30, 40, 60, 90, 120, and 150 meV to which the simulated fragment distance distribution curves by a Monte-Carlo routine, including various realistic effects as elucidated in section 4.3 were used to generate a fit using a χ^2 optimisation routine. Refer to section 5.3 for a detailed discussion of the same.

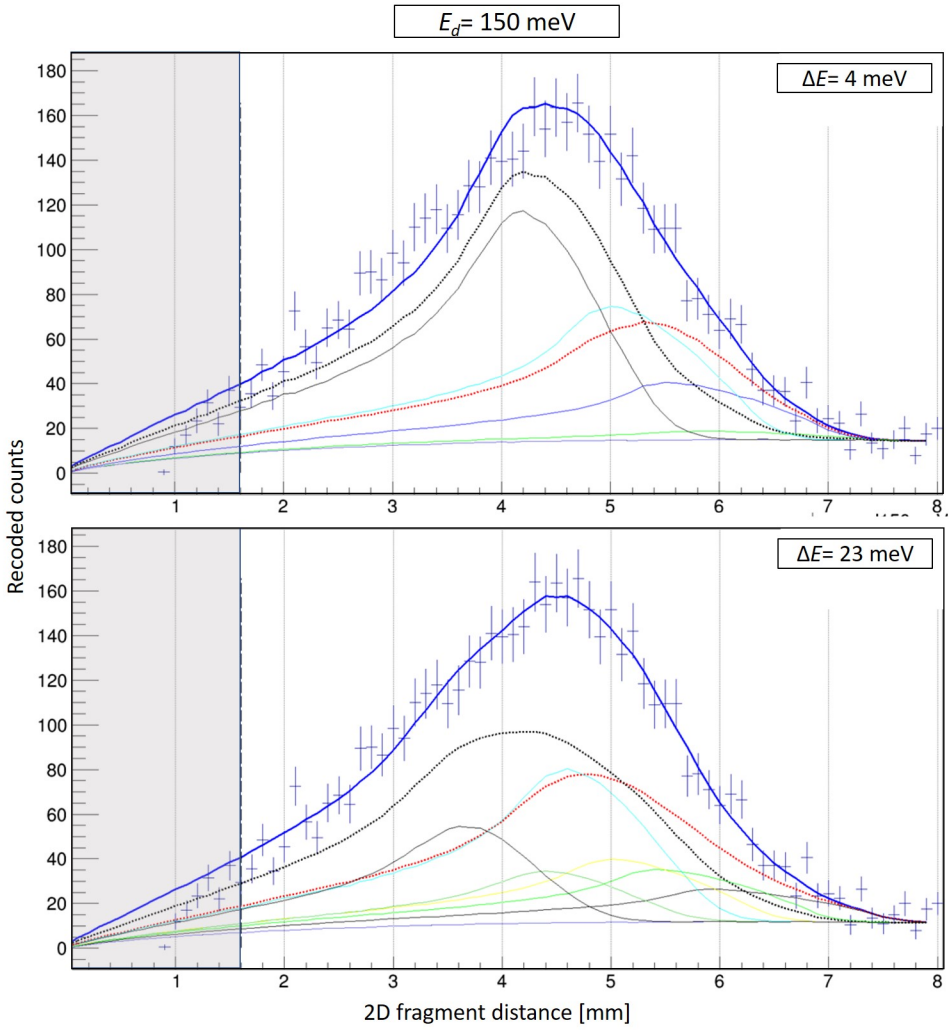

Figure A.1: The obtained fitted curves for $E_{\mathrm{d}} = 150$ meV (for the $500-600$ sec measurement), assuming endothermicity $\Delta E = 4$ and 23 meV; refer to Chapter 5 for discussion.

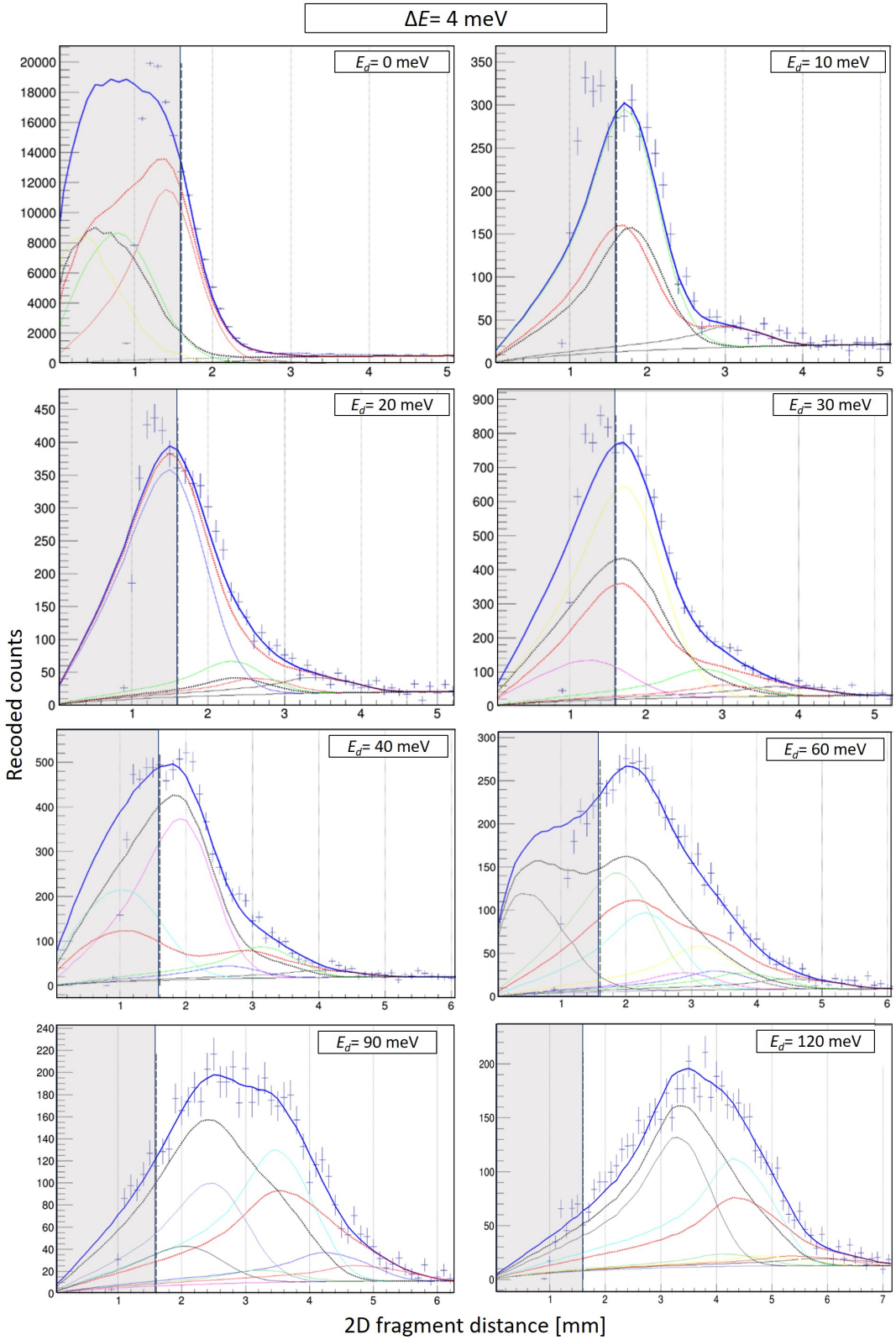

Figure A.2: The obtained fitted curves for $\Delta E = 4$ meV for the 500−600 sec measurement dataset for E_{d} as indicated; refer to Chapter 5 for discussion.

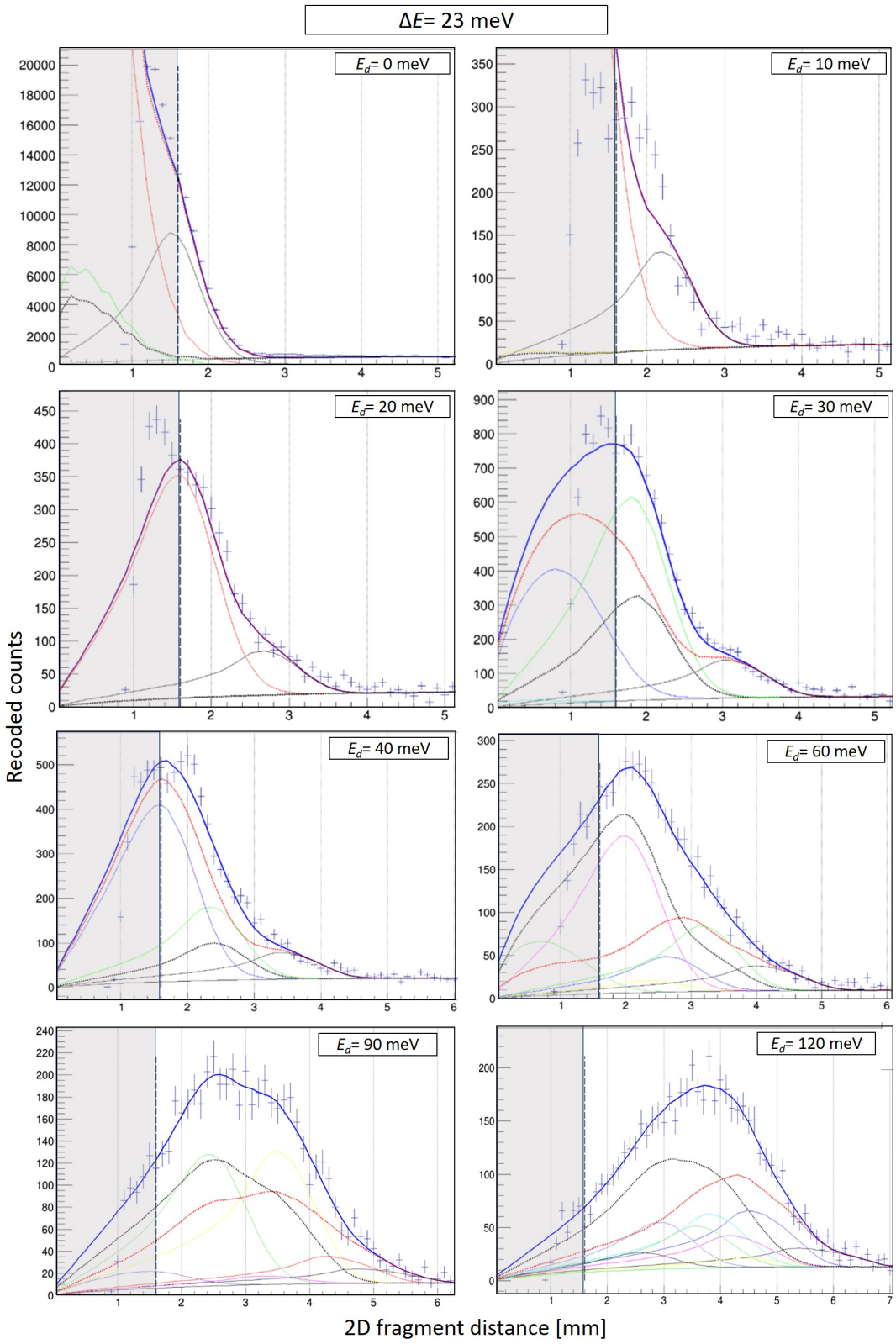

Figure A.3: The obtained fitted curves for $\Delta E = 4$ meV for the 500−600 sec measurement dataset for E_{d} as indicated; refer to Chapter 5 for discussion.

Acknowledgements

I honestly believe that it would not be an overexaggeration to call the opportunity to pursue this work as a very real piece of my childhood physics fascinations coming to life, and for this I have numerous people to be grateful to, without whom this experience would have not been so enriching for me.

Foremost, I would like to extend my deepest gratitude to *Prof. Dr. Andreas Wolf* for accepting me in his working group at the Max-Planck-Institute for Nuclear Physics and granting me this opportunity to contribute to such an inspiring project. His infectious passion, extensive understanding of physics, the ability to consistently think critically and further from obvious, and to communicate such ideas so aptly, have been a great source of inspiration throughout the course of our interactions and till date. The generosity and thoughtfulness that he proffered especially in the trying times of 2020 pandemic crisis on behalf of the group and the institute have helped me immensely and I will always be grateful for this.

I wish to sincerely extend my gratefulness to *Dr. Oldřich Novotný* who has been my supervisor and mentor throughout the period at MPIK. I can not imagine coming this far if it were not for his constant support, advises, understanding, and of course, unending patience through the proof-reading of this thesis. He has been a constant source of motivation through his actions, ingenious understanding of technological systems, and exceedingly perceptive take on solving physics puzzles, which makes the most complicated of procedures look simple.

A special thanks to *Dr. Umesh Kadhane* whose role in my journey through the last four years cannot be aptly expressed in finite words. His ways of seeing the world and understanding it have made me believe in myself, and in the courage to dream further.

I would like to wholeheartedly thank my colleagues at MPIK who made the ten months seem like a happy blip along my time axis. I have learnt a great deal from the academic and personal discussions alike with *Dr. Ábel Kálosi* and *Daniel Paul*, who are not only brilliant physicists but also really kind human beings and I thank them for helping me each time I asked for their time, and even when I could not make myself to ask but was in desperate need. I wish to thank *Dr. Patrick Wilhelm* and *Dr. Sunny Saurabh* who completed their Ph.D. periods while my stay and played a huge role in making me comfortable in the

working group, and familiarising me with the beautiful town of Heidelberg. A special thank you to *Julia Jäger* for the great conversations and for making sure my thesis writing was not restricting me from venturing out in to the real world.

I owe much thanks to the rest of the Stored and Cooled ions group, including *Dr. Holger Kreckel, Dr. Florian Grussie, Aigars Znotiņš, Damian Müll, Felix Nüsslein, Viviane Schmidt*, and *Lisa Gamer*, for making the work on this experiment such a great experience and for many fruitful discussions, conversations, outings and musings, which I will cherish for a lifetime.

I wish to express my sincerest gratitude to the Max-Planck-Institute for Nuclear Physics in Heidelberg, and especially the division of *Prof. Dr. Klaus Blaum* for hosting me so kindly, along with all the of administrative and technical staff at the institute for their indispensable and generous support. I could not have envisaged a more flawless and enriching experience in a place so far from what I knew as home, without their help.

I would like to thank the Department of Physics at the Indian Institute of Space Science and Technology, Thiruvananthapuram, for their continuous consideration and evaluation of my work, and the institute administration for allowing me to avail this opportunity of pursuing my project work at MPIK. I gratefully acknowledge all the consideration and support extended through the pandemic crisis and in facilitating my travel back to India.

I am extremely thankful to all my friends who helped me through this time, especially *Ayushi Kalyan, Rashi Jain* and *Shefali Sharma* who were my go-to humans through my stay in Germany. A special thanks to *Shreya Mishra* for always being there to support me, through all my deepest worries and highest points alike.

Finally, no words can express how thankful I am to my family, to whom I owe my everything, my parents *Deepak Jain* and *Deepika Jain*, and my brother, *Aryan* – this has been possible because of your efforts. Kudos!

Naman Jain